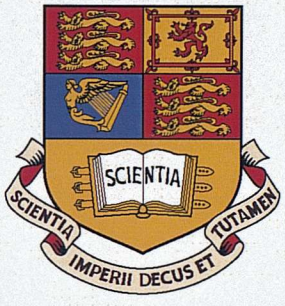
Large Eddy Simulation of Two-phase Reacting Flows



Claudio Lettieri

Department of Mechanical Engineering

Imperial College London

A thesis submitted for the degree of

Doctor of Philosophy

I declare that the present thesis is my own work and has not been submitted in any form for another degree or diploma at any university. Information derived from the published and unpublished work of others has been acknowledged in the text and a list of references is given in the bibliography.

to my parents

"A person who never made a mistake never tried anything new"
A.Einstein

Acknowledgements

I would firstly like to thank my supervisor Professor W.P. Jones for his advice and encouragement throughout my studies at Imperial College. I also wish to thank my co-supervisor Dr. A.J. Marquis for his insightful comments, advices and his help with the multi-block code. Among the numerous people I feel grateful to, I think I owe a special thank to Dr. S.N. Martinez, for his priceless support during most part of my PhD. I am also grateful to Mr. Paolo Ariaudo, Mr. Massimo Palomba and Mr. Luigi Castiglione for endevouring my application to this position. Finally, I wish to thank my friends Regina Zoby and Tiziana Rossetti.

I dedicate this thesis to my parents, whose constant love and support has without a doubt sustained me during these years.

Abstract

The aim of the present work is to investigate, by mean of numerical techniques, the dynamics of turbulent two-phase flows in practical aeronautical applications. A Large Eddy Simulation Eulerian-Lagrangian particle methodology is applied to the study of a two-phase flow in an experimental burner. A Lagrangian description of the dispersed phase is adopted and combined with an Eulerian description of the continuous phase with two-way coupling between the gas and the liquid phase. A probabilistic description of the liquid phase is incorporated and stochastic models for the filtered Lagrangian rates of change of droplet position, mass and temperature are presented. A stochastic formulation for the droplet diameters is devised and incorporated into the equation describing the evolution of the spray pdf in order to simulate the atomisation of sprays in the framework of uncorrelated breakup events. Several non-reacting and reacting test cases are simulated. In the non-reacting cases the performances of the numerical methodology are investigated through comparison of the predicted values of the gas-phase, as well as data for the liquid phase with experimental findings. In the reacting cases the same numerical methodology is applied to the study of the ignition in an aeronautical-type swirl-stabilized spray burner.

Nomenclature

Subscripts

$_{\alpha,\beta}$	scalar field indices
$_{i,j,k}$	coordinate indices
$_{\ell}$	liquid or dispersed phase
$_{\xi}$	droplet surface
$_{g}$	gas or continuous phase
$_{sgs}$	sub-grid scale
$_{g}$	continuous phase property
$_{p}$	dispersed phase property

Greek Symbols

α_p	volume fraction
β	sub-grid scale breakup frequency constant
ΔU	velocity difference
Δ	LES filter width
δ_{08}	velocity level thickness
Δ_{hf}	standard heat of formation

δ_{ij}	Kronecker symbol
$\dot{\omega}_\alpha$	Chemical source term of specie α
$\dot{\Theta}$	rate of change of the droplet temperature
ϵ	rate of dissipation of turbulent kinetic energy
η	Kolmogorov length scale
Γ	diffusion coefficient
μ	dynamic viscosity
μ_{sgs}	turbulent eddy viscosity
ν	kinematic viscosity
ν	stoichiometric coefficient
Ω	LES filter volume
ω	breakup frequency
ϕ_α	general reactive scalar
ψ_i	sample space of the random variable ϕ_i
ρ	density
ρ_p	density of particle p
σ	surface tension
σ_{ij}	stress tensor
σ_{sgs}	sub-grid standard deviation
τ	timescale
τ_p	particle response time
τ_t	sub-grid timescale

τ_{sgs} sub-grid mixing time scale

θ_{lq} integral liquid volume flux

ξ_{α}^{n} continuous stochastic field n for specie α

a_p particle acceleration

t_η Kolmogorov time scale

$theta_u$ momentum thickness

u_η Kolmogorov velocity

Roman Symbols

$\bar{\dot{S}}_{mass}$ filtered mass source term per unit volume

$\bar{\dot{S}}_{v}^{\alpha}$ filtered source term of general reactive scalar per unit volume

$\dot{S}_\alpha$ net formation rate of specie α per unit volume

$\dot{N}$ rate of change of the droplet number

$\dot{R}$ rate of change of the droplet radius

$\mathbf{J}^{sgs}$ turbulent diffusional flux vector

$\mathbf{u}_p$ velocity vector of particle p

$\mathbf{x}_p$ spatial location vector of particle p

$\mathcal{F}$ fine grained joint pdf

$\tilde{P}_sgs$ density weighted sub-grid pdf

A drift coefficient

A_j pre-exponential factor j-th reaction

B Spalding number for mass transfer

B diffusion coefficient

C	CFL number
C_ϕ	micromixing constant
C_a	concentration of species α
C_D	drag coefficient
C_o	dispersion constant
c_p	specific heat at constant pressure
C_s	Smagorinsky constant
C_V	evaporation constant
Cp_p	specific heat at constant pressure of particle p
D	droplet final diameter
$d\mathbf{W}_t$	increment of the Wiener process
D_α	Diffusivity of species α
d_m	mean particle size
D_o	droplet initial diameter
d_p	diameter of particle p
dm_p	particle mass
dT_p	particle temperature
F	liquid volume flux
F_D	drag force
F_g	graviational force
G	LES filter function
g_i	gravitational acceleration in i-direction

h	enthalpy
H_{fg}	latent heat of evaporation
k	thermal conductivity
k	wave number
k_j	rate coefficient of j-th reaction
k_{sgs}	sub-grid kinetic energy
L	characteristic lengthscale
L_0	integral length scale
Le	Lewis number
m_p	mass of particle p
n	spread of particle sizes
N_s	number of scalars
Nu	Nusselt number
P	sub-grid pdf
p	Thermodynamic pressure
Pr	Prandtl number
q	liquid volume flux
R	Rosin-Rammler probability distribution function
R	universal gas constant $R = 8.315(KJ/KgmolK)$
r_c	particle critical radius
r_p	particle radius
$R_{1/2F}$	radial distance where the liquid volume flux is half of the centreline value

$R_{1/2U}$ radial distance where the velocity is half of the centreline value

R_{cdf} Rosin-Rammler cumulative distribution function

Re Reynolds number

Re_p Reynolds number of particle p

S_{ij} Filtered strain tensor

Sc Schmidt number

Sh Sherwood number

St Stokes number

T temperature

t time

t_c characteristic timescale

t_I integral time scale

T_p temperature of particle p

U characteristic velocity

U mean axial velocity

U_c convective velocity

u_i velocity in i-direction

U_C mean co-flow axial velocity

U_{eo} excess axial velocity at the jet centreline

U_e excess axial velocity

U_{min} minimum velocity

U_o axial velocity at the jet centreline

u_{rel} relative velovity

W_α molar mass of specie α (Kg/Kg mol)

We Weber number

x_i coordinate in i-direction

Y_α Mass fraction of species α

$y_{0.5}$ 'centreline' penetration

$\bar{\dot{S}}_m$ filtered momentum source term per unit volume

Superscripts

$'$ forward reaction

$''$ backward reaction

$\bar{}$ mean contribution of Reynolds decomposition

$\bar{}$ spatial filtering

$\tilde{}$ Favre filtering

$'$ fluctuating component of Reynolds decomposition

Acronyms

AMD Arithmetic Mean Diameter

DNS Direct Numerical Simulation

LES Large Eddy Simulation

pdf probability density function

RANS Reynolds Averaged Navier Stokes

SMD Sauter Mean Diameter

Contents

Nomenclature 12

1 Introduction and Thesis Outline **24**

1.1 Introduction 24

1.2 Thesis Outline 26

2 Gas Phase Equations **28**

2.1 Introduction 28

2.2 Governing Equations 29

2.3 Turbulence 32

2.3.1 Scales of Turbulent Motion 32

2.3.2 Modelling 33

2.4 Large Eddy Simulation 36

2.5 Numerical Aspects 40

3 Spray Equations **42**

3.1 Introduction 42

3.2 Overview 43

3.2.1 Stochastic Approach 43

3.3 PDF modelling of sprays 46

3.4 Two-way coupling terms 51

4 Atomisation **53**

4.1 Introduction 53

4.2 Overview 54
4.3 Atomisation Physics 55
4.3.1 Primary Breakup 56
4.3.2 Secondary Breakup 58
4.4 Literature Review 63
4.5 Present breakup model 68
4.5.1 Overview 68
4.5.2 The Model 68
4.5.3 Breakup Frequency 69
4.5.4 Discrete Poisson release process 75
4.5.5 Pdf of diameters for the daughter particles 77
4.6 Results 80
4.6.1 Diesel spray in still flow 80
4.7 Atomisation of mono-dispersed diesel droplets in a cross-flow air stream 84
4.7.1 Air Jet 86
4.7.2 Bag breakup regime (We=68) 87
4.7.3 Stretching and thinning breakup regime (We=153) 94
4.7.4 Catastrophic breakup regime (We=383) 96
4.7.5 Evolution of the system of one single droplet 100
4.8 Conclusions 104

5 Large Eddy Simulation of the two-phase flow in an experimental swirl-stabilized burner 106
5.1 Introduction 106
5.2 Configuration 107
5.3 Meshing 111
5.4 Gas Phase 117
5.5 Simulation Remarks 129
5.6 Two Phase Flow 142
5.6.1 Injector characterisation 142
5.6.2 Validation 145
5.7 Discussion 151

5.8 Conclusions 156

6 Large Eddy Simulation of turbulent reacting flow in an experimental burner - Ignition **158**

6.1 Introduction 158
6.2 Overall features of the ignition experiment 159
6.3 Simulations 160
6.3.1 Failed Ignition 164
6.3.2 Successful Ignition 168
6.4 Conclusions 179

7 Conclusions and Further Works **182**

A Stochastic Review **185**

B Random Variate Generation **189**

C Basics of spray characterization **191**

D Large Eddy Simulation of complex geometries **194**

References **207**

List of Figures

2.1 Conceptual representation of the Energy Spectra for RANS and LES applied in an homogeneous isotropic turbulent field [39] . . . 36

3.1 Mean Diameter according to axial distance (We=383). Distance in mm (x axis) AMD in μm (y axis) 49

4.1 Primary and Secondary breakup 55
4.2 Sketch of the near-injection region of a spray in the atomisation breakup regime 56
4.3 Atomisation Mechanism 58
4.4 Droplets deformation and breakup with Weber and Ohnesorge . . 60
4.5 Pulse shadowgraphs of secondary breakup in the bag breakup regime (water, We = 15, Oh = 0.0045) 61
4.6 Pulse shadowgraphs of secondary breakup in the shear breakup regime (ethyl alcohol, We = 81, Oh = 0.0126). [21] 62
4.7 Deterministic component of the breakup frequency versus droplet diamter, $\rho_g = 1.2$ kg/m^3, $\rho_l = 817$ kg/m^3, $r_o = 100$ μm, $\sigma =$ N/m 73
4.8 Stochastic component of the breakup frequency, $\rho_g = 1.2$ kg/m^3, $\rho_l = 817$ kg/m^3, $r_o = 100$ μm, $\sigma =$ N/m 73
4.9 Critical diameter versus rate of dissipation of turbulent kinetic energy 74
4.10 Deterministic component at different relative velocities (a) - Stochastic component at different relative ϵ (b) 75
4.11 Poisson distribution 76

4.12 Dimensionless pdf of daughter parcels indicating evolution of the pdf with dissipation rate of turbulent kinetic energy, $\rho = 1000\frac{kg}{m^3}$ $r_o = 1.5mm$ $\sigma = 0.072\frac{N}{m}$ 78
4.13 Dimensionless pdf of daughter parcels indicating evolution with the radius - $\rho = 13.57kg/m^3$, $\epsilon = 200000\frac{m^2}{s^3}$, $\sigma = 0.0295N/m$ . . . 79
4.14 Dimensionless pdf of daughter parcels indicating evolution with the diameter collected approximatively 1 million breakups 79
4.15 Injection methodologies 81
4.16 Sauter Mean Diameter distribution along the axis of injection - Distance in cm from the injector (x axis) SMD in μm (y axis) . . 82
4.17 Spray penetration, time in μm, distance in cm 83
4.18 Snapshot of the diesel injection - Left gas phase axial velocity contour [m/s] - Right droplets colored by diameter [μm] 84
4.19 Schematic diagram of the experimental droplet generator and gas nozzle 85
4.20 Measurement points of th PDA experiment according to th breakup regimes 86
4.21 Variation with axial distance of the mean velocity along the centerline in the jet with different Cs 87
4.22 Sauter Mean Diameter of droplets: left experimental, right simulated 88
4.23 Breakup in cross flow 89
4.24 Sauter Mean Diameter of droplets: left experimental, right simulated 89
4.25 Size distribution according to radial distance at a distance of 8 mm from the jet nozzle. Distance in mm (x axis) SMD in μm (y axis) 90
4.26 Size distribution according to radial distance at a distance of 12 mm from the jet nozzle. Distance in mm (x axis) SMD in μm (y axis) 90
4.27 Size distribution according to radial distance at a distance of 16 mm from the jet nozzle. Distance in mm (x axis) SMD in μm (y axis) 91
4.28 Droplet Mean Axial Velocity according to radial distance at a distance of 8 mm from the jet nozzle. Distance in mm (x axis) Velocity in m/s (y axis) 91

4.29 Droplet Mean Axial Velocity according to radial distance at a distance of 12 mm from the jet nozzle. Distance in mm (x axis) Velocity in m/s (y axis) 92
4.30 Droplet Mean Axial Velocity according to radial distance at a distance of 16 mm from the jet nozzle. Distance in mm (x axis) Velocity in m/s (y axis) 92
4.31 Probability density function of droplet diameter at injection . . . 93
4.32 Probability density function of droplet diameter at z = 12 mm , r = 8 mm 93
4.33 Probability density function of droplet diameter at z = 4 mm , r = 2 mm 94
4.34 Mean Diameter according to axial distance (We=153). Distance in mm (x axis) AMD in μm (y axis) 95
4.35 Mean Diameter according to axial distance (We=153). Distance in mm (x axis) SMD in μm (y axis) 95
4.36 Droplet Mean Velocity according to axial distance (We=153). Distance in mm (x axis) Velocity in m/s (y axis) 95
4.37 Mean Diameter according to axial distance (We=383). Distance in mm (x axis) AMD in μm (y axis) 96
4.38 Mean Diameter according to axial distance (We=383). Distance in mm (x axis) AMD in μm (y axis) 97
4.39 Droplet Mean Velocity according to axial distance (We=383). Distance in mm (x axis) Velocity in m/s (y axis) 97
4.40 Size distribution according to radial distance at a distance of 8 mm from the jet nozzle. Distance in mm (x axis) SMD in μm (y axis) 98
4.41 Size distribution according to radial distance at a distance of 12 mm from the jet nozzle. Distance in mm (x axis) SMD in μm (y axis) 98
4.42 Size distribution according to radial distance at a distance of 16 mm from the jet nozzle. Distance in mm (x axis) SMD in μm (y axis) 99

4.43 Droplet Mean Axial Velocity according to radial distance at a distance of 8 mm from the jet nozzle. Distance in mm (x axis) Velocity in m/s (y axis) 99
4.44 Droplet Mean Axial Velocity according to radial distance at a distance of 12 mm from the jet nozzle. Distance in mm (x axis) Velocity in m/s (y axis) 100
4.45 Droplet Mean Axial Velocity according to radial distance at a distance of 16 mm from the jet nozzle. Distance in mm (x axis) Velocity in m/s (y axis) 100
4.46 Droplets characteristics from fragmentation of a single particle in the Park at al. experiment 101
4.47 Droplets characteristics from fragmentation of a single particle in the Park et al experiment 102
4.48 Droplet Diameters versus time (a) - Droplets age versus time (b) . 103
4.49 Droplets characteristics from fragmentation of a single particle in the Park at al. experiment 103
4.50 Droplets characteristics from fragmentation of a single particle in the Park Lee experiment 104

5.1 Lateral view of the MERCATO experimental rig 107
5.2 MERCATO Test bench - front view (a) - Combustor (b) 108
5.3 Sketch of the MERCATO test bench 108
5.4 Definition of the axis and measured velocity components. 110
5.5 Measurement planes 111
5.6 Velocity Vectors. Complete Grid 112
5.7 Mean axial velocity profiles for the partial and complete grid . . . 113
5.8 Mean tangential velocity profiles for the partial and complete grid 113
5.9 Mean radial velocity profiles for the partial and complete grid . . 114
5.10 Partial geometry grid 115
5.11 Injector area close-up 115
5.12 Planar sections 116
5.13 Mean Axial velocity. Top: Lateral view. 8mm Front section (a) - 26mm Front section (b) 118

5.14 Mean Axial velocity 119
5.15 Instantaneous snapshot of the axial velocity. Top: Lateral view. 8mm Front section (a) - 26mm Front section (b) 120
5.16 Mean Tangential velocity. Top: Lateral view. 8mm Front section (a) - 26mm Front section (b) 121
5.17 Mean Tangential Velocity 122
5.18 Instantaneous Tangential Velocity. Top: Lateral view. 8mm Front section (a) - Air Mixture Fraction 26mm Front section (b) 123
5.19 Mean Radial velocity. Top: Lateral view. 8mm Front section (a) - 26mm Front section (b) 124
5.20 Mean Radial Velocity 125
5.21 Instantaneous Radial Velocity. Top: Lateral view. 8mm Front section (a) - 26mm Front section (b) 126
5.22 *Rms* of Axial Velocity 127
5.23 *Rms* of Tangential Velocity 127
5.24 *Rms* of Radial Velocity 128
5.25 Air mass fraction 128
5.26 Mean Axial velocity - WR=0.284 $Kg/sec\sqrt{K/bar}$ 129
5.27 Mean Tangential Velocity - WR=0.284 $Kg/sec\sqrt{K/bar}$ 130
5.28 Mean Radial Velocity - WR=0.284 $Kg/sec\sqrt{K/bar}$ 130
5.29 *Rms* of Radial Velocity - WR=0.284 $Kg/sec\sqrt{K/bar}$ 131
5.30 *Rms* of Tangential Velocity - WR=0.284 $Kg/sec\sqrt{K/bar}$ 131
5.31 *Rms* of Axial Velocity - WR=0.284 $Kg/sec\sqrt{K/bar}$ 132
5.32 Mean Axial velocity - WR=0.424 $Kg/sec\sqrt{K/bar}$ 132
5.33 Mean Tangential Velocity - WR=0.424 $Kg/sec\sqrt{K/bar}$ 133
5.34 Mean Radial Velocity - WR=0.424 $Kg/sec\sqrt{K/bar}$ 133
5.35 *Rms* of Radial Velocity - WR=0.424 $Kg/sec\sqrt{K/bar}$ 134
5.36 *Rms* of Tangential Velocity - WR=0.424 $Kg/sec\sqrt{K/bar}$ 134
5.37 *Rms* of Axial Velocity - WR=0.424 $Kg/sec\sqrt{K/bar}$ 135
5.38 Contour plots of recirculation areas 136
5.39 Isosurface of Q-criterion at different times (a) - (d) 137
5.40 FFT of velocity components of test case WR=0.142 for Probe 1 - Axial (a) Transverse (b) 139

5.41 FFT of pressure of the test case WR=0.142 and velocity component of test case WR=0.426 for Probe 1 - Pressure (a) Axial (b) . 139
5.42 FFT of velocity components and pressure of test case WR=0.426 for Probe 1 - Transverse (a) Pressure (b) 140
5.43 FFT of Transverse velocity components case WR=0.142 - Probe2 (a) Probe5 (b) 140
5.44 FFT of Axial velocity component and pressure for case WR=0.426 - Probe5 (a) Probe6(b) 140
5.45 FFT of Transverse velocity components for probe 10 - case WR=0.142 (a) case WR=0.426 (b) 141
5.46 Probe signal of test case WR=0.142 - Axial velocity component(a) Transverse velocity component (b) 141
5.47 Injector schematic and perspective view 143
5.48 Injector, frontal view 143
5.49 Hollow cone pattern 144
5.50 Schematic of injection configuration and angles 145
5.51 Kerosene Droplets by diameter 145
5.52 Sauter Mean Diameter contour with measurement locations . . . 146
5.53 Sauter Mean Diameter. Filled dots represents experimental data, dots represents the results of the simulations, lines are polynomial fit of the computed values 147
5.54 Liquid Mean Axial Velocity contour with measurement locations 148
5.55 Liquid Mean Axial Velocity. Symbols are the same as figure (5.53) 148
5.56 Liquid Mean Transverse Velocity contour with measurement locations 149
5.57 Liquid Mean Transverse Velocity. Symbols are the same as Figure 5.53 150
5.58 *Rms* of Liquid Axial Velocity. Symbols are the same as Figure 5.53 150
5.59 *Rms* of Liquid Transverse Velocity. Symbols are the same as Figure 5.53 151
5.60 Liquid Volume Flux. Symbols are the same as Figure 5.53 152
5.61 Isosurface of Temperature showing evaporation in the PVC . . . 153
5.62 Liquid Injection 153

5.63 Sauter Mean Diameter z=6mm 154
5.64 Sauter Mean Diameter z=26mm 154
5.65 Mean droplet diameter 155
5.66 SMD 156

6.1 Spark occurrence (Volt) versus pressure drop 160
6.2 Spark occurrence (Volt) versus pressure drop - Ignition close-up . 161
6.3 Gaussian distribution of spark Temperature 162
6.4 Spark plug abscissa versus FAR 163
6.5 Kerosene mass fraction isosurface and contour 165
6.6 Kerosene mass fraction isosurface and Temperature contour . . . 166
6.7 Scatter plot of kerosene mixture fraction versus temperature . . . 167
6.8 Kerosene mass fraction isosurface and Temperature contour . . . 167
6.9 Extinguishing flame after spark removal - 26 mm (a) wall (b) . . . 168
6.10 Instantaneous droplets snapshot after t=10 ms from spark deposition. The circle shows the spark location 169
6.11 Temperature contour at t=10 ms after the spark application . . . 170
6.12 Temperature contour at t=20 ms after the spark application . . . 171
6.13 Temperature contour at t=60 ms after the spark application . . . 172
6.14 Temperature contour at t=80 ms after the spark application . . . 173
6.15 Global scatter plot of kerosene vapour mixture fraction versus temperature 174
6.16 Scatter plot of kerosene vapour mixture fraction versus temperature- 8mm section (a) 26mm section (b) 174
6.17 Scatter plot of kerosene mixture fraction versus temperature- 56 mm (a) 86mm section (b) 175
6.18 Scatter plot of kerosene mixture fraction versus temperature- 116 mm (a) 130mm section (b) 175
6.19 Mean temperature (a) and H2 mass fraction (b) along the axis of the combustor 176
6.20 Mean CO2 mass fraction (a) and H2O mass fraction (b) along the axis of the combustor 176
6.21 Mean axial velocity profiles 177

6.22 Axial velocity rms profiles 177
6.23 Mean temperature profiles 178
6.24 Mean CO2 mass fraction profiles 178
6.25 Mean kerosene mass fraction profiles 179

D.1 Basic scheme of halo cells for the left-side sub-domain 195
D.2 Basic scheme of halo cells in a multi-domain configuration 196

Chapter 1

Introduction and Thesis Outline

1.1 Introduction

Turbulent multi-phase flows are encountered in several engineering applications, such as internal combustion engines, liquid and solid propellant rocket motors, aircraft gas-turbines and industrial burners. The vast majority of aeronautical propulsion systems are based on combustion and uses liquid hydrocarbons, mostly kerosene, as a fuel. In a gas turbine the fuel normally enters the combustor by way of a fuel injector in the form of a thin column or film and which, on interaction with turbulent structure of the gas phase, undergoes fragmentation, dispersion and evaporation. The physics of such flows is extremely complex and is difficult to predict. The ability to simulate numerically two-phase flows in complex geometries would ideally lead to improvements in the design of burners and would be a significant contribution to the study of complex phenomena such as ignition and extinction. Moreover, an accurate modelling of the combustion process in practical geometries would be of considerable aid in achieving a reduction in fuel consumption and pollutant emissions.

Three main topics are the centre of the attention of the current industrial research: specific fuel consumption, engine noise and emission reduction [39]. The demand for more efficient engines with lowered environmental impact gave rise to a series of new studies of the combustion process. The specific fuel consumption

is significantly effected by the choice of the overall layout of the system, to which numerical simulation can be applied as an optimisation tool. For what concerns the field of emission reduction, the major pollutants produced during combustion of a typical aircraft propulsion systems are unburned and partially burned hydrocarbons, nitrogen oxides (NO and NO_2), carbon monoxide and particulate matter in various forms [90]. The emission of CO_2 is closely linked to overall fuel consumption and therefore related to the necessity of increasing the engine efficiency. Other emissions like NO_x , CO, unburned hydrocarbons or particle emissions like soot are primarily influenced by combustor design.

Numerical simulation of turbulent reacting flows is capable of giving vast information concerning the physics of the problem and can be seen as an ideal tool for the study of the combustion process. Unfortunately, a direct approach (Direct Numerical Simulation) is often unfeasible for practical applications so that a statistical description is usually the only available option. Statistical methods based on Reynolds Averaged Navier Stokes equations are probably the most widely implemented in industrial applications. However, this approach has proved in the past to be not sufficiently accurate for the the investigation of phenomena, such as combustion, which are greatly influenced by the small scales motions. Moreover, previous studies available [79, 100], demonstrated that in a two-phase flow the dispersion of the liquid phase is mostly governed by the large scale turbulent motions, which in a Reynolds Averaged Navier Stokes approach are strongly effected by the model applied.

In this respect, Large Eddy Simulation (LES) has demonstrated its ability to reproduce turbulent gaseous flows in complex geometries [4, 96] and is becoming a standard tool for computational research. The potential of both simulating turbulent flows with good accuracy, and being numerically affordable makes LES an ideal tool for the simulation of practical cases.

In the present work LES is applied to the simulation of the two-phase flow in an experimental burner. The set up is essentially an aeronautical-type swirl-stabilized spray burner, fuelled by Jet-A liquid Kerosene. An Eulerian description of the continuous phase is adopted and fully coupled with a Lagrangian definition of the dispersed phase. The characteristic dimensions of the particulate phase are comparable to the smallest turbulent length scales enabling the particles to be

viewed, in respect of their influence on the gas phase, as point sources. Dispersion and evaporation of the droplets are considered, and stochastic models for the sub-grid scale (sgs) contributions are adopted. The model for breakup, being one of the main topic of the present work, is presented and is validated by comparison with experimental data. The performances of the proposed Lagrangian particle methodology is investigated by comparison of the simulated results with experimental findings.

1.2 Thesis Outline

In Chapter 2, the governing equations of turbulent flows are introduced. The problem of Turbulence modelling is reviewed along with some consideration about the turbulent scales: the Reynolds Averaged Navier-Stokes approach, the Direct Numeric Simulation approach and the Large Eddy Simulation approach are briefly discussed. The LES methodology is described in more details and the filtered equations for the gas phase are presented.
In Chapter 3, the equations for the dispersed phase are described. The Lagrangian particle methodology is summarised and the reasons for the choice of a stochastic approach are discussed. The equations for droplets dispersion and evaporation are introduced, along with the models for the sub-grid scale contributions to particle dispersion and vaporisation.
In Chapter 4, liquid atomisation is described. The chapter presents the definition of breakup with a short review of the physics of the most common atomisation regimes. The problem of modelling fragmentation in the framework of LES is introduced and an overview of the models available in the literature is given. A new model for droplet breakup is proposed using a stochastic methodology. The model is validated via comparison of the predicted results with existing measurement in two different configurations; at first a spray in a typical diesel injection configuration is investigated. Secondly, the case in which a Kerosene spray is injected in a cross flow is considered.
In Chapter 5 the LES Lagrangian particle methodology is applied for the study of

a practical aeronautical combustor. The models proposed in the previous chapters for droplets break-up, evaporation and dispersion are used in the simulation of the two-phase flow in a swirl-stabilised combustor. The problems arising in the simulation of complex geometries is briefly discussed. Finally, the simulated values of gaseous and liquid properties are compared with experimental data and the results are discussed.

Chapter 6 presents an investigation of the ignition in the same configuration studied in Chapter 5. Two different test cases are considered, varying the inlet conditions for both the gas and liquid phase. In the first test case no combustion is observed and the spark procedure fails to achieve ignition of the kerosene-air mixture. A second test case is considered in which the flame is studied through the analysis of the scatter plots of temperature versus kerosene mixture fraction and the mean profiles of the gas phase variables.

Finally, in Chapter 7 the findings of the present study are summarised and some suggestions for further investigations are given.

Chapter 2

Gas Phase Equations

2.1 Introduction

The aim of the present study is to validate and investigate the performance of the LES based methodology in the spray case for practical applications. Therefore, a theoretical background must be provided for the continuous phase flow to be modelled. In this chapter the governing equations of turbulent reacting flows in their instantaneous form are briefly described. The equations shown are limited to those actually used in the thesis so that the present review does not represent an exhaustive description of the mathematical formulation of the physics of fluids. More comprehensive accounts can be found in [68], [27] and in the references therein.

The equations have been presented in the form proposed by [2] and [53], to which source terms have been added in order to incorporate the two-phase coupling between the gas and liquid phases. The equations include balances for mass, momentum and energy. Attention is focused on the Navier-Stokes equation in the case of high Reynolds number flows: the important features of turbulence are briefly reviewed in order to introduce the problem of turbulence modeling. The importance of the application of some sort of average or filtering is discussed in one of the sections where the most common computational approaches are introduced. The LES methodology is discussed in detail and the filtered equations

are reported.
All the equations are presented in the Cartesian tensor form with the Einstein summation convention adopted throughout

2.2 Governing Equations

Fluid flow can be described by governing equations derived from the principles of mass, momentum and energy conservation together with the continuum hypothesis. The mass conservation or *continuity* equation can be written as

$$\frac{\partial \rho}{\partial t} + \frac{\partial \rho u_i}{\partial x_i} = \dot{S}_{mass} \tag{2.1}$$

where ρ is the fluid density, t is time, u_i is the velocity in i^{th} direction, x_i is the Cartesian coordinate in i^{th} direction and $\dot{S}_{mass}$ represents a global mass sink/source term. The mass source term takes into account the destruction or creation of mass which can occur in any part of the control volume. For instance, this can be due to evaporation or condensation of the liquid phase dispersed in the gas continuum. In the present work we suppose that the size of the liquid fragment is small enough to enable the droplets to be viewed as point sources, allowing the mass coupling to be achieved by means of a source term added to the continuity equation.
The conservation of momentum is described by equations which relate the local change of momentum u_i in time t to convective transport and to the forces due to deformation, pressure and gravity.

$$\frac{\partial \rho u_k}{\partial t} + \frac{\partial \rho u_i u_k}{\partial x_i} = \rho g_k - \frac{\partial p}{\partial x_k} + \frac{\partial \sigma_{ik}}{\partial x_i} + \dot{S}_{mom,i} \tag{2.2}$$

where σ_{ik} is the viscous stress tensor, u_i represents the three velocity components, p is the pressure, g_k is the gravity acceleration. $\dot{S}_{mom,i}$ represents source/sink terms for the momentum. In this respect, a source of momentum is added to the Navier-Stokes equations in order to consider two-way coupling between the continuous and dispersed phases due to the particle acceleration. For a Newtonian

ffuid, the components of the symmetric stress tensor σ_{ij} can be expressed as a function of the molecular viscosity and the local strain rate:

$$\sigma_{ij} = 2\mu S_{ij} - \frac{2}{3}\mu S_{kk}\delta_{ij} \tag{2.3}$$

$$S_{ij} = \frac{1}{2}\left(\frac{\partial u_i}{\partial x_j} + \frac{\partial u_j}{\partial x_i}\right) \tag{2.4}$$

where δ_{ij} is the Kronecker delta and μ is the coefficient of the viscosity which is a function of the temperature and the composition.
Thus for a Newtonian fluid, the equation (2.2) is written as:

$$\frac{\partial \rho u_k}{\partial t} + \frac{\partial \rho u_i u_k}{\partial x_i} = \rho g_k - \frac{\partial p}{\partial x_k} + \frac{\partial}{\partial x_i}(\mu(\frac{\partial u_k}{\partial x_i} + \frac{\partial u_i}{\partial x_k} - \frac{2}{3}\delta_{ik}\frac{\partial u_j}{\partial x_j})) + \dot{S}_{mom,i} \tag{2.5}$$

This equation is the Navier-Stokes equation.
The species conservation equation is given by

$$\frac{\partial \rho Y_\alpha}{\partial t} + \frac{\partial \rho Y_\alpha u_i}{\partial x_i} = \frac{\partial J_{\alpha,i}}{\partial x_i} + \dot{S}_{Y_n} + \dot{\omega}_\alpha \tag{2.6}$$

where Y_α is the mass fraction of the specie α, $\dot{S}_{Y_n}$ express the rate of creation/destruction of species α and ω_α is the mass source term defined as:

$$\dot{\omega}_\alpha = \Sigma_k(\nu''_{kk} - \nu'_{kk})K_k\Pi_m C_m^{\nu_\alpha k} \tag{2.7}$$

where ν denotes the matrix of stoichiometric coefficients, $C_m = Y_m\rho/W_m$ and $k = Aexp(-E/RT)$. $J_{\alpha,i}$ is the diffusional flux with contribution of concentration gradients, mass diffusion due to temperature, external forces and pressure gradients. If diffusion can be described by Fick's law, valid for binary diffusion, then

$$J_{\alpha,i} = -\rho D_\alpha \frac{\partial Y_\alpha}{\partial x_i} \tag{2.8}$$

where D_α is the diffusion coefficient of species α. Substituting equation (2.8) into equation (2.6) the following equation can be derived for the species conservation:

$$\frac{\partial \rho Y_\alpha}{\partial t} + \frac{\partial \rho Y_\alpha u_i}{\partial x_i} = \frac{\partial}{\partial x_i}\left(\frac{\mu}{Sc_\alpha}\frac{\partial Y_\alpha}{\partial x_i}\right) + \dot{S}_{Y_n} + \dot{\omega}_\alpha \tag{2.9}$$

where $Sc_\alpha = \mu/\rho D_\alpha$ is the Schmidt number for the α specie. It is often postulated that the diffusivity coefficient of the various species is identical. With this assumption a unique Sc number can be defined for all the species.
The equation of the energy can take many forms, including static pressure, stagnation enthalpy, internal energy or temperature as main variables. In the present work the energy equation is proposed in the form of enthalpy conservation equation. The enthalpy, h, is a function of species mass fractions and temperature.

$$h = h(Y_1, Y_2, ..., Y_n, T) = \sum Y_\alpha (h_{0\alpha} + \int c_{p\alpha} dT) \tag{2.10}$$

where $h_{0\alpha}$ is the enthalpy of formation and $c_{p\alpha}$ is the heat capacity of species α. The energy transport equation can be written in its complete form as:

$$\begin{aligned} \frac{\partial \rho h}{\partial t} + \rho u_i \frac{\partial h}{\partial x_i} &= \frac{\partial p}{\partial t} + u_i \frac{\partial p}{\partial x_i} + \tau_{ij} \frac{\partial u_i}{\partial x_i} + \dot{S}_h \\ &- \frac{\partial}{\partial x_i} \left[-\frac{\mu}{Pr} \frac{\partial h}{\partial x_i} + \mu \left(\frac{1}{Pr} + \frac{1}{Sc} \right) \sum_n h_n \frac{\partial Y_n}{x_i} \right] \end{aligned} \tag{2.11}$$

where $Pr = cp\mu/k$ is the Prandtl number, k is the local instantaneous thermal conductivity and $\dot{S}_h$ represent the enthalpy source term. The first term on the right hand side of equation (2.11) is usually neglected in combusting flows, while the last term is removed in the case that the Prandtl and Schmidt number are unique for all the species: the Lewis Number ($Le = Pr/Sc$) is of the order of one and there are low compressibility effects. The gas temperature can be computed from the enthalpy and the species mass fractions, and it is not directly solved.
The relation between the local pressure, temperature, density and composition of the gaseous mixture is defined through the state equation:

$$p = \rho RT \sum_\alpha \frac{Y_\alpha}{W_\alpha} \tag{2.12}$$

where the density is a function of the local composition, pressure and enthalpy fields:

$$\rho = \rho(p, h, Y) \tag{2.13}$$

2.3 Turbulence

When inertial effects are prominent over the damping action of viscosity, fluids undergo transition to a turbulent state. Probably one of the most important characteristics of turbulent flows is its irregularity, or randomness. This makes a deterministic approach to turbulence problems very difficult. An increasing number of irregular random fluctuations arises from any perturbation applied to the flow, and rapidly propagate in time and space. Perturbations in the initial or boundary conditions of the flow are unavoidable. The striking feature of turbulence is that the flow field displays an acute sensitivity to such perturbations. Predicting the behavior of these systems is very difficult, because of the complexity and non-linearity of the problem. Instabilities are related to the interaction of viscous terms and non linear inertia terms in the equation of motion, which can become exceedingly complex and the mathematics of nonlinear partial differential equations has not been developed to a point where a solution can be found for practical cases. Turbulence exhibits an highly diffusive behavior, which causes rapid mixing and increases the transfer rates of momentum, heat and mass. Therefore, applications such as combustion or sprays are strongly influenced by turbulent motions; a reliable numerical method is needed to overcome the problems arising in the mathematical solution of the equations of motion.

2.3.1 Scales of Turbulent Motion

Richardson's theory of the energy cascade describes turbulence as an hierarchy of eddies of different sizes. Energy enters the flow in the form of big eddies, which are unstable and break down into smaller ones. The energy is transfered from the large scales to smaller ones in a process which is called the energy cascade. This process goes on until a scale is reached at which viscosity is capable of dissipating the kinetic energy into heat. A major contribution to the theory of turbulence is due to Kolmogorov and Obukhov to which we will refer in the present review. An important length scale is the characteristic length of the largest turbulent motions, l_0 which is comparable to the flow length scale L. It is clear that this scale is strongly influenced by the geometry of the flowfield. However, while

the turbulence progresses into smaller and smaller scales this 'dependence' or 'information' is lost. The range of scales for which turbulent motion is isotropic can be referred to as the universal equilibrium range. Kolmogorov quantified the upper limit of this region by defining a characteristic length $l_{EI} = l_0/6$. As the scales are reduced the effect of viscosity becomes progressively more important and the kinetic energy of the flow is eventually dissipated into heat. It is assumed that the rate at which the smallest scales dissipate kinetic energy is equal to the rate at which the kinetic energy is transfered to the small scales, then the turbulence is in equilibrium condition and the smallest scale can be completely characterised by the rate of dissipation of kinetic energy ϵ and the kinematic viscosity ν. The characteristic length and velocity of these dissipative motions are:

$$\eta = \left(\frac{\nu}{\epsilon}\right)^{1/4} \tag{2.14}$$

$$u_\eta = (\nu\epsilon)^{1/4} \tag{2.15}$$

where η is the Kolmogorov length scale and u_η is the Kolmogorov velocity scale. The range of scales for which the effects of viscosity are not relevant, so that kinetic energy is just redistributed to increasingly smaller eddies is called the inertial subrange. Its lower limit is defined by $l_{DI} \approx 60\eta$ [68]. Such an energy redistribution is controlled by a single parameter: the rate of dissipation of energy. As pointed out earlier, at scales smaller than l_{DI} the viscosity effects become important. The range of scales with dimensions $\eta < l < l_{DI}$ is called the dissipation range. It remains to be defined how the turbulent kinetic energy is distributed among all these turbulent ranges. It has been demonstrated that the bulk of the energy is contained in the larger eddies in the size $l_{EI} < l < 6l_0$ which has been defined "the energy-containing range".

2.3.2 Modelling

From the previous sections it starts to become clear that the problem of solving directly the Navier Stokes equations is a very difficult challenge. The high capability of these equations in describing precisely flow motions represents, from a

practical point of view, their greatest limitation. The mathematical difficulties intrinsically embodied in the structure of the equations leave few if no space at all for an analytical solution. Indeed, analytic solutions are feasible only in few cases when the geometry, the initial and boundary conditions are very simple. The necessity of applying numerical methodologies is thus set evident.
The velocity field in a turbulent flow is three-dimensional, time-dependent and effectively random. The largest turbulent motions are as large as the geometry while it can be shown that the smallest scales decrease dramatically as the Reynolds number increases. In fact the lengthscale ratio η/L decreases as $Re^{-3/4}$, while the timescale ratio as $Re^{-1/2}$ [68]. The ratio between the largest scale and the Kolmogorov scale gives an estimation of the number of turbulent structures which are contained in a single turbulent motion:

$$\left(\frac{l_0}{\eta}\right)^3 = Re^{9/4} \tag{2.16}$$

A Direct Numeric Simulation (DNS) involves the direct solution of the Navier Stokes equations. Because all length scales and time scales have to be resolved, DNS is computationally very expensive. It can be shown, [43, 44, 93], that the computational cost for such approach is proportional to Re^3. When combustion is considered, even more stringent requirements are found. Therefore, the application of DNS for high Reynolds number flows is totally unfeasible in practical engineering applications.
Statistical approaches must therefore be considered: Reynolds was among the first to develop a statistical formulation, decomposing the flow variables into a mean and a fluctuating part. This approach is called Reynolds-averaged Navier-Stokes (RANS). The solution is achieved by solving the Reynolds equations for the mean velocity after models are introduced in order to determine the unknown terms. Indeed, the Reynolds stresses which arise from the averaging of the Navier-Stokes equations require a model of some kind in order to close the equations. About the simplest approach that can be adopted are turbulent viscosity models where the eddy viscosity is obtained either from an algebraic relation or from turbulence quantities such as the kinetic energy k and the rate of dissipation ϵ. In so called second moment closures, model transport equations are solved for the individual

Reynolds stresses, without the need of a turbulent viscosity. RANS models have been extensively used in the past and represents today one of the most widely used computational approach in industrial applications. However, in RANS the quality of the prediction depends strongly on the quality of the adopted model. Previous studies [79, 100] have demonstrated that in two-phase flows the dispersion of the liquid phase is mostly governed by the large scale of motions. Because of the averaged nature, RANS calculations of two-phase flows have demonstrated in the past to be not completely reliable.

In this regard Large Eddy Simulation (LES) represents a good compromise between accuracy and computational load, as it is intermediate between the direct solution of the flowfield in DNS, and the modelled approach of RANS methodologies. LES is very different from the other two methods, however the idea behind this methodology follows a similar technique as that adopted in RANS approaches. RANS and LES differ by the operator employed in the derivation: in RANS the operator consists of a time average or an ensemble average over a set of realizations of the flowfield, while in LES, the operator is a spatially localized time independent filter of given size. The latter is applied to a single realization of the studied flow, allowing information to be collected about the instantaneous field and not only averaged values. At the end of the previous section it was noticed that the energy spectrum is not uniformly distributed among all the scales. The large turbulent structures, which are predominantly responsible for the transport of mass, momentum, species concentration and the dispersed phase, are also the scales where most of the energy is located. The smallest scales in the flow have a more general behavior, independent of the geometry and their main purpose is to dissipate the kinetic energy transferred from the largest scales. Even though the contribution of these smallest scales is important, it must be said that they are more amenable to modelling than the larger scales, because of their isotropic nature. Figure (2.1) from [39] illustrates the conceptual representation of the Energy spectrum for RANS and LES when applied to a homogeneous isotropic turbulent field. It is evident that the information lost in the averaging process is smaller in LES so that the effects of the model on the predictions is less relevant and the results are likely to be closer to the real physics of the problem. For the

reasons presented above, LES has a clear potential in predicting turbulent flows for industrial applications.

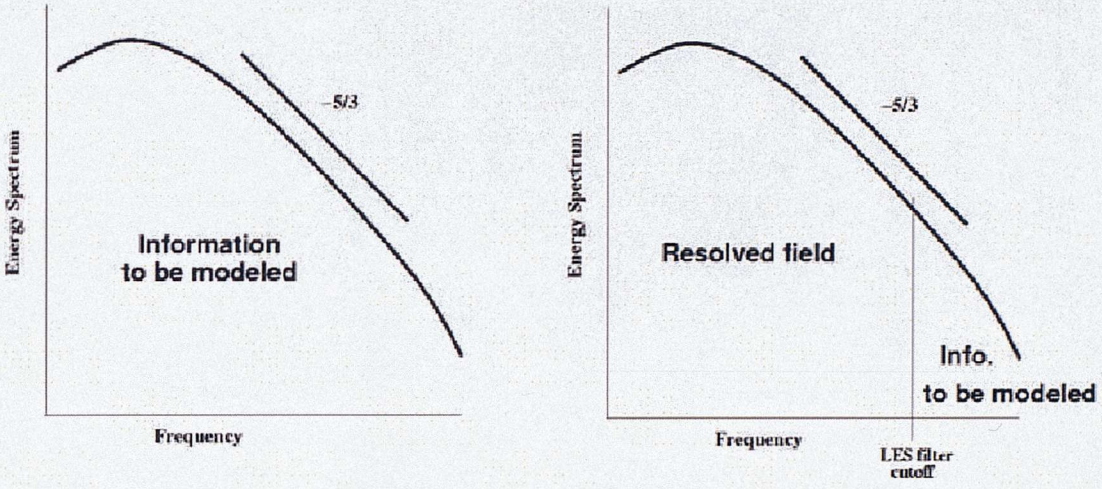


Figure 2.1: Conceptual representation of the Energy Spectra for RANS and LES applied in an homogeneous isotropic turbulent field [39] .

2.4 Large Eddy Simulation

In Large Eddy Simulation (LES) the dynamics of the large, energy-containing structures are computed directly and the effects of the small dissipative structures are modelled. The Navier-Stokes equations that govern the conservation of mass, momentum, and energy in a fluid, are filtered to obtain the LES equations for fluid motion. The filtering operation results in terms that must be modelled. Closure of the filtering governing equations can be achieved using sub-grid models. This approach is consistent with Kolmogorov's theory of self similarity, stating that the large eddies of the flow are dependent on the geometry, whilst the smaller scales have a more universal character (locally isotropic). It was pointed out in a section (2.3.1) that such an assumption implies that orientations arising from external geometry have been erased at smaller scales, and the only parameters governing their motion are the mean rate of dissipation of energy per unit of mass of fluid ϵ and the viscosity ν. A second hypothesis of Kolmogorov's theory consists of admitting the existence of an inertial range of scales in which the

effects of viscosity are not relevant and so energy is only redistributed over that range of scales. It can be shown that ϵ is controlled by the large scales which are, therefore, the most significant.

The process of removing unresolveable scales from the equation of motion can be achieved by applying a spatial filter to any function representing a turbulent flow property. A general filter operator G of kernel Δ is defined by:

$$\bar{\psi}(\mathbf{x},t) = \int\int\int_{-\infty}^{+\infty} G(\mathbf{x}-\mathbf{x}',\Delta)\psi(\mathbf{x},t)d\mathbf{x}' \tag{2.17}$$

where consistency with the limiting case $\psi(\overrightarrow{x},t) = constant$ requires the filter function to integrate to unity. In the presence of density variation, it is common to introduce a density weighted filter, also named Favre filtering, defined as follows:

$$\tilde{\psi} = \frac{\overline{\rho\psi}}{\bar{\rho}} \tag{2.18}$$

By using this formalism the filtered Navier-Stokes equations can be written as

Filtered Continuity:

$$\frac{\partial\bar{\rho}}{\partial t} + \frac{\partial\bar{\rho}\tilde{u}_i}{\partial x_i} = \bar{\dot{S}}_{mass} \tag{2.19}$$

Filtered Momentum:

$$\frac{\partial\bar{\rho}\tilde{u}_k}{\partial t} + \frac{\partial\bar{\rho}\widetilde{u_i u_k}}{\partial x_i} = \bar{\rho}g_k - \frac{\partial\bar{p}}{\partial x_k} + \frac{\partial\bar{\sigma}_{ik}}{\partial x_i} + \bar{\dot{S}}_{mom,i} \tag{2.20}$$

where $\bar{\tau}_{ij} = -2\mu\tilde{S}_{ij} + \frac{2}{3}\mu\tilde{S}_{kk}\delta_{ij}$, the filtered strain tensor is usually accounted for using the filtered velocity field as $\tilde{S}_{ij} = \frac{\partial\tilde{u}_i}{\partial x_j} + \frac{\partial\tilde{u}_j}{\partial x_i}$. Filtered source terms for particle laden flows are added in order to include the effect of particles on the gas phase.

It can be noticed that the filtering operation results in a closure problem for the filtered transport equations: $\widetilde{u_i u_j} \neq \tilde{u}_i\tilde{u}_j$. In order to overcome this problem an unknown filtered stress tensor is introduced, so that the convective term of the equation can be written as:

$$\bar{\rho}\tilde{u}_i\tilde{u}_j = \bar{\rho}\widetilde{u_i u_j} + r_{ij} \tag{2.21}$$

In this way the filtered stress r_{ij} incorporates all the errors of the splitting of the Favre filter of the product into the product of the Favre filtered quantities. Equation (2.20) can thus be written as:

$$\frac{\partial \bar{\rho}\tilde{u}_i}{\partial t} + \frac{\partial \bar{\rho}\widetilde{u_i u_j}}{\partial x_j} = \bar{\rho} g_k - \frac{\partial \bar{p}}{\partial x_i} + \frac{\partial \bar{\tau_{ij}}}{\partial x_j} - \frac{\partial r_{ij}}{\partial x_j} + \bar{\dot{S}}_{mom,i} \tag{2.22}$$

The main task to be accomplished by a model for the residual stress is to provide a correct rate of drain of energy from the large scales. Indeed, an equation for the kinetic energy expression, with $\tilde{k} = 1/2\tilde{u}_i\tilde{u}_i$, can be derived then:

$$\frac{\partial \bar{\rho}\tilde{k}}{\partial t} + \frac{\partial \bar{\rho}\widetilde{u_i k}}{\partial x_j} = -\tilde{u}_i \frac{\partial \bar{p}}{\partial x_i} + \frac{\partial \bar{\tau_{ij}}\tilde{u}_i}{\partial x_j} - \bar{\tau_{ij}}\bar{S_{ij}} - \frac{\partial \tilde{u}_i r_{ij}}{\partial x_j} \tag{2.23}$$

where the positive term $\tau_{ij}\bar{S}_{ij}$ provides a drain of energy representing the effect of the unresolved scales.

The oldest and probably the most widely used model for the residual stresses is that proposed by Smagorinsky [85]. The basic idea of this model is to connect the residual stress to the resolved strain rate with an eddy viscosity type hypothesis. The model can be summarised through the equations:

$$r_{ij} = r^d_{ij} + \frac{1}{3} r_{kk}\delta_{ij} \tag{2.24}$$

which is expressed as

$$r^d_{ij} = -2\mu_{sgs}\widetilde{S}_{ij}. \tag{2.25}$$

where

$$\mu_{sgs} = \bar{\rho}(C_s\Delta)^2||\widetilde{S}_{ij}|| \tag{2.26}$$

and

$$||\widetilde{S}|| = \sqrt{2\widetilde{S}_{ij}\widetilde{S}_{ij}} \tag{2.27}$$

In which Δ is the filter width,$||\tilde{S}_{ij}||$ is the Frobenius norm, r^d_{ij} is the deviatoric sgs stress and C_s is a model constant. Estimation of the order of C_s can be obtained in the case of isotropic turbulence and infinite inertial range, through an estimation of the mean subgrid scale kinetic energy and imposing that the production of kinetic energy is equal to the dissipation.

Dynamic versions of the Smagorinsky model allow the value of the parameter Cs to be determined as a function of time and position without the need for a value to be specified by the user. The fundamental assumption of dynamic calibration of Smagorinsky parameter is that of scale invariance. Consider two different filter widths Δ_1 and Δ_2 in the inertial subrange, it is possible to write the following equivalence:

$$C_s(\overrightarrow{x},t)|_{\Delta_1} = C_s(\overrightarrow{x},t)|_{\Delta_2} \tag{2.28}$$

A test filter is introduced with filter length Δ larger than the filter already applied by LES. C_s can be derived from the filtered momentum equation by imposing equation (2.28). Germano [60] derived the following expression for the model parameter by assuming that the latter is a slowly varying function of space:

$$(C_s\Delta_1)^2 = \frac{1}{2}\frac{L_{ij}^{(a)}\tilde{S}_{ij}}{M_{ij}\tilde{S}_{ij}} \tag{2.29}$$

$$M_{ij} = \alpha^2\hat{\bar{\rho}}||\hat{\tilde{S}}||\hat{\tilde{S}}_{ij} - \widehat{(\bar{\rho}||\tilde{S}||\tilde{S}_{ij})} \tag{2.30}$$

where L_{ij}^a represents the anisotropic component of the the stress tensor. Lilly [54] proposed an alternative version which can be written as:

$$(C_s\Delta_1)^2 = -\frac{1}{2}\frac{L_{ij}^{(a)}M_{ij}}{M_{ij}^2} \tag{2.31}$$

Other models are also available [26], but are not used in the present work. The scope of the present investigation is an application of the proposed LES particle methodology to the solution of practical test cases. Therefore, for the sake of convenience the choice between a standard or dynamic model in the simulation was made dependant on the quality of the predictions. The standard Smagorinsky model was preferred over the dynamic version as it is computationally cheaper. However, in cases where the simulations failed to produce good results, a sgs model refinement was adopted through use of a dynamic calibration (both Lilly calibration and Piomelli-Liu are available in the in-house source code Boffin-LES).

Finally the filtered scalar transport equation for a scalar field $\xi(x,t)$ (for example a mass fraction field) can be written as:

$$\frac{\partial \bar{\rho}\tilde{\xi}}{\partial t} + \frac{\partial \bar{\rho}\widetilde{u_i\xi}}{\partial x_i} = -\frac{\partial}{\partial x_i}\left[\frac{\mu}{Pr}\frac{\partial \tilde{\xi}}{\partial x_i}\right] + \bar{\dot{S}}_\xi \tag{2.32}$$

Like the momentum equation, the non linearity of the convective terms makes the filtered equation unclosed. Using Germanos framework, the following vector quantity can be introduced:

$$\eta_j^{(\xi)} = \bar{\rho}\widetilde{\xi u_i} - \bar{\rho}\tilde{\xi}\tilde{u}_j \tag{2.33}$$

For its nature equation (2.32) is usually referred to as the sub filter flux of scalar ξ; in a similar fashion as for the residual stresses also the sub filter flux requires modelling.

The filtered enthalpy equation is proposed in its simple form valid for unitary Lewis number and low compressibility effects.

$$\frac{\partial \bar{\rho}\tilde{h}}{\partial t} + \frac{\partial \bar{\rho}\widetilde{u_i h}}{\partial x_i} = -\frac{\partial}{\partial x_i}\left[\frac{\mu}{Pr}\frac{\partial \tilde{h}}{\partial x_i}\right] + \bar{\dot{S}}_h \tag{2.34}$$

Where, as before, the non linearity of the convective term can be dealt with the introduction of a sub filter enthalpy flux, $\eta^h = \bar{\rho}\widetilde{hu_i} - \bar{\rho}\tilde{h}\tilde{u}_j$, which requires modelling.

2.5 Numerical Aspects

The code utilised throughout the present work is the in-house code BOFFIN (BOundary Fitted Flow Integrator) extensively described in [40] and [7]. The code is based on a finite-volume approach using an implicit low-Mach number formulation with a SIMPLE type pressure correction and a pressure smoothing algorithm. A Central Difference Scheme (CDS) is used for the spatial discretisation, while the temporal discretisation scheme implements a Crank-Nicholson (C-N) approach. The code adopts a Bi-conjucate gradient iterative method for the solution of the equations. The implementation of the discretisation schemes

for sde (which will be introduced in the next chapter) for the liquid stochastic equations and their coupling to the flow field is relatively straight forward and follows conventional discretisation schemes presented in appendix A.

Chapter 3

Spray Equations

3.1 Introduction

This chapter presents the governing equations for a dispersed phase immersed in a continuous turbulent flow. A phase is said to be dispersed in a hosting fluid medium when its elements can not be viewed as forming a continuum. The liquid phase is simulated with a Lagrangian approach, which treats droplets as a set of discrete particles on which point mechanics is applied.
In the first part of this chapter a short overview on the available models for Lagrangian particle tracking is considered. The need for a stochastic methodology is discussed and the dynamics of the joint probability density function of the particle variables is derived. In the second part of the chapter the current models for droplet dispersion and evaporation are presented. Finally, the terms for two way coupling between gas and liquid phase are introduced following the general assumption that the characteristic dimensions of the particulate phase are small enabling the particles to be viewed, in respect of their influence on the gas phase, as a point sources.

3.2 Overview

The utilisation of a Lagrangian particle methodology is not new. A number of works [9, 10, 42, 62, 70, 71, 79] can be found in literature which have used this approach in several applications including RANS, LES and DNS. In a DNS the gas phase is solved to the smallest scale so that at each instant the properties of the flow $\phi(t) = (\rho(t), U(t), p(t), h(t))$ at the particle position are known. The particle can be characterised by a state vector $\overrightarrow{\psi}(t) = (\psi_1 ... \psi_n)$, whose elements represent particles properties such as position, velocity, mass, temperature and diameter. The evolution of the particle state vector can be linked to the gas phase dynamics [84] by applying ad-hoc governing equations.
This is not the case for LES: only filtered information for the continuous phase is available. If the properties of the flow field at the particle position is decomposed into filtered and residuals, $\phi(x,t) = \tilde{\phi}(x,t) + \phi_{sgs}(x,t)$, then in LES only $\tilde{\phi}(x,t)$ is known. Because of the size of the droplets being comparable with the unresolved scales the effects of the filtered motions, $\phi_{sgs}(x,t)$, on the particle dynamics is significant. In chapter (2) it was observed that the behavior of these small scales is unpredictable and random. From the point of view of an LES observer, the droplets immersed in a turbulent flow will experience the effects of the filtered known velocity, plus a "random" perturbation due to the filtered unknown component. The gas phase is solved over time intervals which are defined by accuracy considerations. In these time intervals the gas could experience fluctuations whose frequency may be higher than that allowed by the filtering operation. Hence, the unresolved information contains both a time and a spacial contribution which are important for defining the particles dynamics. The absence in $\tilde{\varphi}$ of the small scale fluctuation is a reason for considering, from a LES point of view, the particle dynamics as Markovian [7].

3.2.1 Stochastic Approach

The application of a stochastic model to simulate the effects of the unresolved scales on the particles dynamics represents a possible solution.

In the literature two main descriptions for a statistical representation of a dispersed phase are available, both derived from the kinetic theory of gases and fluids: the Klimontovich formulation and the Liouville formulation [25]. A review of the relative theory is beyond the scope of the present work; interested readers are directed to appendix A and references therein. From these formulations two different approaches can be derived: a convection-diffusion partial differential equation (pde) or a Monte Carlo stochastic differential equation (sde). The pde and sde approaches are equivalent when the phase space trajectories of the process are deterministic, and it is possible to demonstrate that the simulation of trajectories (Monte Carlo sde in phase space) has an information content about the process which is greater than or equal to that contained in the solution of the corresponding pde. In its general form sdes including a Markovian dynamic via a Wiener process term, can be written:

$$X_t = X_0 + \int_0^t a(s, X_s)ds + \int_0^t b(s, X_s)dW_s \tag{3.1}$$

with $dW_s = W_{s+dt} - W_t$. In [7, 25] it is shown that a substantial equivalence exists between this kind of "trajectory approach" which uses sdes and the probability density function (pdf) formulation of the problem:

$$\text{PDF Problem} \begin{cases} \frac{\partial}{\partial t}p = -\sum_i \frac{\partial}{\partial x_i}(A_i(\overrightarrow{x}, t)p) + \\ +\sum_{ij} \frac{1}{2}\frac{\partial^2}{\partial x_i \partial x_j}[\underline{B}(\overrightarrow{x}, t) \times \underline{B}^T(\overrightarrow{x}, t))_{i,j}p] \\ p = p(\overrightarrow{x}, t|\overrightarrow{x}_0, t_0) \\ p_0(\overrightarrow{x}_0, t_0)\,\overrightarrow{x}_0 \in D \\ \text{boundary conditions for } p(\overrightarrow{x}, t|\overrightarrow{x}_0, t_0) \in \partial D \end{cases} \tag{3.2}$$

$$\text{Trajectory Problem} \begin{cases} d\overrightarrow{X}_t = A(\overrightarrow{X}, t)dt + \underline{B}(\overrightarrow{X}, t)d\overrightarrow{W}_t \\ \overrightarrow{X}(t=0)\text{distributed with density } p_0(\overrightarrow{x}_0, t_0) \\ \text{set of conditions if } \overrightarrow{X}\text{is on the boundary}\partial D \end{cases} \tag{3.3}$$

The pdf transport equation (3.2) and its analogue set of phase space trajectory sdes (3.3) are just two formulations of the same problem. It is possible either to use a Monte Carlo integration of the sdes for many particles, or a numerical approximation of the transport equation of the pdf. On the one hand in the sde

approach the Lagrangian modelling is more intuitive, the boundary conditions are more naturally implemented, and the Monte Carlo integration is computationally more efficient. On the other hand, the knowledge of $\tilde{P}$ with all its moments is a more complete representation than the the individual moments that result from a Monte Carlo calculation. However, even if the solution of the transport equation might reveal more features, the sde approach is adopted in this work for reasons of computational efficiency. A different choice is possible, and has been adopted by other authors, [28].

The rate of change of the particle state vector $d\psi_i(t)$ can be written in a form which contains a deterministic, a stochastic continuous and a stochastic discontinuous term. The deterministic continuous time term comes from the effects of the filtered flow field. The Markovian continuous time variation attempts to take into account the effects of the unresolved scales. Following [25] a stochastic discontinuous term can be added to the formulation equation (3.1) in order to take into account random discontinuous changes of the particle state vector. This term is introduced to incorporate a Poisson breakup release process, as to be discussed in section 4.5.4 of chapter 4. The appropriate sde can be written as:

$$d\psi_i(t) = f_i(\vec{\psi}, \tilde{\vec{\varphi}}, t)dt + B_{ij}(\vec{\psi}, \tilde{\vec{\varphi}}, t)dW_t^{(j)} + A_{ij}(\vec{\psi}, \tilde{\vec{\varphi}}, t)\delta N_{dt}^{(j,\Lambda)} \tag{3.4}$$

where f_i and B_{ij} represent respectively the drift and diffusion terms. $N_t^{(j,\Lambda)}$ is the j^{th} component of a stochastic counting process evolving at a rate Λ. $\delta N_{dt}^{(j,\Lambda)}$ is the variation of $N_t^{(j,\Lambda)}$ observed over a time dt, and A_{ij} is the physical model that serves to re-adapt the integer number $\delta N_{dt}^{(j,\Lambda)}$ to the intensity of physical switch variation of $d\psi_i(t)$. As showed in equation (3.2) the equivalent Pdf transport equation can be written as:

$$\begin{aligned}\frac{\partial}{\partial t}\tilde{P}(\vec{\psi}, t|\vec{\psi_0}) = &-\sum_i \frac{\partial}{\partial \psi_i}[f_i(\vec{\psi}, \vec{\varphi}, t)\tilde{P}(\vec{\psi}, t|\vec{\psi_0})]+ \\ &+\sum_{ij}\frac{1}{2}\frac{\partial^2}{\partial\psi_i\partial\psi_j}[B_{ij}(\vec{\psi}, \vec{\varphi}, t)\tilde{P}(\vec{\psi}, t|\vec{\psi_0})]+ \\ &+\int_\Omega [J(\vec{\psi}, \vec{\chi}, t)\tilde{P}(\vec{\psi}, t|\vec{\psi_0}) - J(\vec{\chi}, \vec{\psi}, t)\tilde{P}(\vec{\psi}, t|\vec{\psi_0})d\vec{\chi}\end{aligned} \tag{3.5}$$

3.3 PDF modelling of sprays

Following Bini and Jones [9] the probabilistic description of the spray is adapted with the state of the spray being characterised uniquely in terms of the droplet radius, r the droplet velocity, $\mathbf{v}$ the droplet temperature, θ and number, n. The required joint *pdf* is $\overline{\mathrm{P}}_{spr}(\mathbf{V}, \mathrm{R}, \Theta, \mathrm{N}; \mathbf{x}, t)$, where $\{\mathbf{V}, \mathrm{R}, \Theta, \mathrm{N}\}$ is the 'phase' space for $\{\mathbf{v}, \mathrm{r}, \theta, \mathrm{n}\}$, which can be obtained, after suitable modelling, from:

$$\frac{\partial \overline{\mathrm{P}}_{spr}}{\partial t} + \nabla_{\mathbf{v}} \cdot \left(\mathbf{a}\overline{\mathrm{P}}_{spr}\right) + \frac{\partial\left(\dot{\mathcal{R}}\overline{\mathrm{P}}_{spr}\right)}{\partial R} + \frac{\partial\left(\dot{\mathcal{T}}\overline{\mathrm{P}}_{spr}\right)}{\partial \Theta} + \frac{\partial\left(\dot{\mathcal{N}}\overline{\mathrm{P}}_{spr}\right)}{\partial N} = 0 \tag{3.6}$$

where $\mathbf{a}, \dot{\mathcal{R}}, \dot{\mathcal{T}}$ and $\dot{\mathcal{N}}$ represent:

$$\mathrm{E}\left(\frac{\mathrm{D}\psi_k}{\mathrm{D}t}\middle|\, \mathbf{\Psi} = \mathbf{\Phi}\right) \text{ where } \mathbf{\Phi} = \mathbf{v}, \mathrm{r}, \theta \text{ and } \mathrm{n}$$

and where $\mathrm{E}\left(\frac{\mathrm{D}\psi_k}{\mathrm{D}t}\middle|\, \mathbf{\Psi} = \mathbf{\Phi}\right)$ is the expect value of $\frac{\mathrm{D}\psi_k}{\mathrm{D}t}$ conditioned upon $\mathbf{\Psi} = \mathbf{\Phi}$ anywhere in the filter volume. These quantities are unknown and models are required.

In order to first model and then solve equation (3.6) it is replaced with an equivalent system [25] (see section 3.2.1) of stochastic ordinary differential equations describing the trajectories of stochastic particles in the phase space $\{\mathbf{V}, \mathrm{R}, \Theta, \mathrm{N}\}$. The models for dispersion and evaporation of droplets have been extensively described in previous publications [10, 41] and are here only briefly outlined.

The Ito equivalent of the closed form of equation (3.6) that describes the evolution of the spray *pdf* in space and time is given by the following system of equations:

$$\begin{aligned} d\mathbf{x}_p &= \mathbf{v}_p dt \\ d\mathbf{v}_p &= \mathbf{a}_p dt \end{aligned} \tag{3.7}$$

where the subscript p represents the p^{th} particle. Consistent with this the motion of a stochastic particle in a turbulent flow field can be viewed as a random process with position determined by a deterministic part, evaluated in terms of filtered values and a stochastic component arising from the *sgs* turbulent motions of the

gas phase. In this study only viscous drag and gravitational forces are considered and a stochastic Markov model [8, 9] is used to represent the influence of the unresolved carrier gas velocity fluctuations experienced by a stochastic particle p over a time dt which is added to the deterministic contribution:

$$d\mathbf{v}_p = \tau_p^{-1}\left(\widetilde{\mathbf{U}}_p\left(t\right) - \mathbf{v}_p\right)dt + \frac{\rho_\ell - \bar{\rho}_p}{\rho_\ell}\mathbf{g}dt + \left(C_o\frac{k_{sgs}}{\tau_t}\right)^{1/2} d\mathbf{W}_t \qquad (3.8)$$

where ρ_ℓ is the particle density, $\mathbf{v}_p$ is the velocity of the p^{th} particle, $\bar{\rho}_p$ and $\widetilde{\mathbf{U}}_p$ are the filtered gas density and velocity at the particle position, k_{sgs} is the unresolved kinetic energy of the gas phase, C_o is a model constant, $d\mathbf{W}_t$ represents the increment of the Wiener process and $\mathbf{g}$ is the gravitational acceleration. τ_t is a sub-grid timescale, which determines the rate of interaction between the particle and turbulence dynamics, defined as:

$$\tau_t = \tau_p\left(\frac{\tau_p}{\frac{\Delta}{\sqrt{k_{sgs}}}}\right)^{0.6} \qquad (3.9)$$

The particle relaxation time, τ_p is given by: $\tau_p^{-1} = \frac{3}{8}\frac{\rho_f C_D}{\rho_p R}|\widetilde{\mathbf{U}}_p - \mathbf{v}_p|$, where the drag coefficient C_D is obtained from Yuen and Chen [101]:

$$C_D = \begin{cases} \frac{24}{Re}\left(1 + \frac{Re^{2/3}}{6}\right) & : \quad 0 < Re < 1000 \\ 0.424 & : \quad Re \geqslant 1000 \end{cases} \qquad (3.10)$$

where Re is the Reynolds number based on the droplet diameter and the relative velocity of the droplet with respect to the gas phase.

The drag coefficient, equation (3.10) was developed for spherical shape particles and is appropriate as long as the droplet remains close to this shape. However in some of the cases to be considered the deformation effects are so large that the use of equation (3.10) is no longer justified. In particular the droplets can deform into a balloon or parachute-like shapes and the drag coefficient should be adjusted accordingly. In Volgin and Yugai [91] and Stekol'shchikov et al [87] and references therein, the drag coefficients of single significantly deformed droplets were measured as a function of Weber number, We. The major result was that C_D increases with We up to a value of about 2 for $We \geq 50$. The drag force also depends on the orientation of the droplet and the flow and strictly it cannot be

expressed in terms of a scalar drag coefficient. The extension of equation (3.8) to account for variable droplet shapes is a complex and difficult task and is not entirely consistent with the assumption of particles acting as point forces and sources. For this reason a scalar drag coefficient is retained. Some justification for this is provided by the statistical approach adopted: in a population of many droplets experiencing the same conditions the modified C_D will apply on average in all directions. The corrected drag coefficient [7] is thus as follows:

$$\bar{C}_D = \begin{cases} C_D & : \quad We \leq We_c \\ C_D + \left(\frac{We - We_c}{50 - We_c}\right)(2 - C_D) & : \quad We \leq 50 \\ 2.0 & : \quad We > 50 \end{cases} \tag{3.11}$$

where the Weber number is defined as $We = \dfrac{2\rho_g r_p |\tilde{\mathbf{U}}_p - \mathbf{v}_p|^2}{\sigma}$ and where σ is the surface tension of the dispersed phase. We_c is the critical value of Weber number below which breakup does not occur. The *sgs* kinetic energy is obtained from $k_{sgs} = \left(2\Delta\nu_{sgs}\tilde{S}_{ij}\tilde{S}_{ij}\right)^{\frac{2}{3}}$, an expression derived using equilibrium arguments (see chapter 2).

The problem of evaporation is is graphically illustrated in figure (3.1) taken from [39]. For the formulation of the evaporation model it is assumed that droplets are spherical and isolated, neglecting the effects of interaction between droplets. The thermal conductivity in the liquid phase is supposed to be infinite, resulting in a homogeneous temperature over the droplet volume as displayed in the figure. The droplets are assumed to be at equilibrium with the surrounding gas phase, guaranteeing continuity of the temperature. The effects of radiating heat are neglected. Finally, the temperature and the properties of the gas are assumed to be homogeneous around the droplet surface, so that the temperature is a function only of the distance from the centre of the particle. The derivations of the evaporation model and the notation are similar to those used by [84]. The gaseous properties at a radial distance r_p corresponding to the droplet radius are indicated with the subscript ζ, while properties in the far field have the subscript ∞. Upon interaction with the gas phase, liquid vaporizes generating mixture fraction of fuel vapour Y_f which has a maximum value near the droplet surface and decreases with the radial distance. It is common that in combustion application the temperature of the liquid fuel is lower than the surrounding gas.

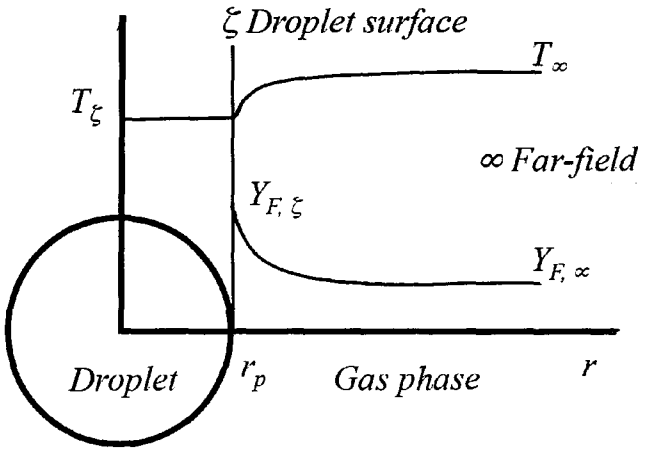


Figure 3.1: Mean Diameter according to axial distance (We=383). Distance in mm (x axis) AMD in μm (y axis)

Miller et al.[61] presented a review of several models for liquid evaporation. In his review Miller showed that various vaporization models perform nearly identically for low evaporation rates at gas temperatures lower than the liquid droplet boiling temperature. This assumption is unfortunately not valid in many practical combustion applications, where the droplets interact with the hot gas of the flame and the temperature of the liquid rises rapidly until it reaches boiling temperature. Therefore, additional modifications to the model are required when the droplets reach saturation. The rate of change of temperature T is considered first. The variation of the temperature of the droplets depends from the heat flux from the gas phase and from the latent heat of evaporation. It can be written as:

$$dT_p = \frac{Nu}{3Pr_g}\frac{Cp_g}{Cp_l}\left(\frac{T_g - T_p}{\tau_m}\right)dt + \frac{h_{fg}}{Cp_l}\frac{dm_p}{m_p} \tag{3.12}$$

where h_{fg} is the latent heat of evaporation, Cp is the specific heat, Pr_g and Sc_g are the gas-phase Prandtl and Schmidt numbers, Nu is the modified Nusselt number and τ_m is a diffusion relaxation time: $\tau_m = \rho_l 4r^2/(18\mu_g)$. The Nusselt number represents the thermal interaction between the droplet and the surroundings and defines the normalised heat flux across the interface. Several correlations using

$Nu = f(Re, Pr, B_T)$ have been proposed in the past [23, 24, 102]. The present model from [84] implements the following corrected Nusselt number:

$$Nu^* = 2 + 0.552 Re_k^{1/2} Pr^{1/3} F(B_T) \tag{3.13}$$

where the Reynolds number is the one of the particle:

$$Re_k = \frac{\rho_g U_{rel} d}{\mu_g}. \tag{3.14}$$

The correction function $F(B)$ is introduced to account for the evaporated fuel mass moving away from the surface at certain velocity, also known as the Stephan flux [1],

$$\frac{1}{F(B)} = (1+B)^{0.7} \frac{\ln(1+B)}{B} \tag{3.15}$$

where the number B represents the heat transfer number, B_T, based on the gas temperature, T_∞, is given by

$$B_T = \frac{C_{pg}(T_\infty - T_p)}{h_{fg}} \tag{3.16}$$

When the temperature of the droplet is lower than the saturation temperature, $T_{drop} \leq T_{sat}$, hence when the rate of evaporation is controlled by mass transfer, the gradient of vapour concentration is important. The mass evolution is expressed as a function of the normalised diffusion across the interface defined as the Sherwood number, Sh. The the mass evaporation rate $\dot{m}_p$ can be written as a function of the modified Sherwood number Sh

$$dm_p = -\frac{m_p}{3Sc_g \tau_m}(Sh^d + Sh^{st}) H_M dt \tag{3.17}$$

In equation (3.17) the Sh^d is the modified Shewood number:

$$Sh^d = 2 + 0.552 Re_k^{1/2} Sc^{1/3} F(B_M) \tag{3.18}$$

while H_M is a function of the mass transfer number B_M as specified in [1].

$$H_M = ln(1 + B_M) \tag{3.19}$$

and

$$B_M = \frac{Y_S - Y_\infty}{1 - Y_S} \tag{3.20}$$

In order to model the effects of the sub-grid velocity fluctuations on the droplets evaporation, a stochastic Sherwood number is defined as

$$Sh^{st}dt = C_V Sc_g^{1/3} \left(\frac{\rho_g k_{sgs}^{1/2} D}{\mu_g} \right) |dW_t|^{1/2} \tau_p^{3/4} \tag{3.21}$$

where C_V is a model constant taken as one [41]. The associated change of diameter dD is derived directly from dm.
When the droplet is at saturation temperature, the mass evaporation rate $\dot{m}_p$ is given by

$$dm_p = -2\pi r_p \frac{Nu}{Pr} \mu_g H_T dt \tag{3.22}$$

In the case of unit Lewis number and equilibrium models, B_T can be replaced with a good degree of approximation with the value of B_M as reported in one of the principal simplifications that Spalding [86] adopted. The viscosity and the specific heat depend on properties of the gas surrounding the droplet which change over the radial distance from the droplet. An interpolation between ζ and ∞ weighted with a factor A = 1/3 [38, 61, 102] is implemented on the temperature and the mass fractions from which μ and C_P are calculated.

$$T_r = T_S + A(T_G - T_S) \tag{3.23}$$

$$Y_r = Y_S + A(Y_G - Y_S) \tag{3.24}$$

The model for breakup, being one of the main topics of this work, is treated separately in chapter(4)

3.4 Two-way coupling terms

The equations reported in the previous section account for the effects of the gas phase on the dispersed particles, defining how the droplets react to the environmental input. This interaction is usually referred to as one-way coupling. In

several applications the opposite interaction, i.e. the effect of the dispersed phase on the continuous phase, is not negligible. This interaction is called two-way coupling in most of the literature [84].
In an LES framework the droplet effects on the turbulent gas phase can be ideally divided in those which influence the large resolved scales and those which effect the unresolved scales. The effects on the sub-grid scales has been addressed by [103]. It has been shown [7] that although a modification of the LES sgs model due to the particles may be an interesting issue, its contribution can often be neglected. In the present work attention is focused on the large scale coupling, which is incorporated in the filtered transport equations of mass, momentum, energy and species mass fraction through source terms. The source terms are provided with a filter symbolism which shows the absence of sub-grid contributions. The source terms take in to account every droplet instantaneously contained in the specific filter volume. The global contribution of the particles at a location ξ within a filtering volume Δ to the source is just the volume average of the individual contributions:

$$\bar{\dot{S}}(\mathbf{x}) = \frac{1}{\Delta}\sum_i \int_D \dot{S}^{(i)}\delta(\xi^{(i)} - \mathbf{y})G(\mathbf{x}-\mathbf{y})d\mathbf{y} \tag{3.25}$$

The relevant terms for mass, momentum, enthalpy and vapour mass fractions are reported below

$$\begin{aligned}
\dot{S}^{(i)}_{mass} &= -\frac{dm_p^{(i)}}{dt} \\
\dot{S}^{(i)}_{mom} &= -\left(m_p^{(i)}\frac{dV^{(i)}}{dt} + \frac{dm_p^{(i)}}{dt}V^{(i)}\right) \\
\dot{S}^{(i)}_{h} &= -\left(\dot{q} + \frac{dm_p^{(i)}}{dt}h_{vap}\right) \\
\dot{S}^{(i)}_{Y_v} &= \frac{1}{\rho\Delta^3}\frac{dm_p^{(i)}}{dt}
\end{aligned} \tag{3.26}$$

where $\dot{q} = m_P Nu/(3Pr\tau_m)Cp_g(T_g - T_p)$ is the heat exchanged with the droplet and $h_{vap} = Cp_g(T_g - T_p)$ is the vapour enthalpy

Chapter 4

Atomisation

4.1 Introduction

The present chapter can be divided into four parts. The first part provides an overview of sprays, explaining the importance of atomisation in combustion along with a short review on the physics of the atomisation process, analyzing the most relevant features of droplet deformation, primary breakup and secondary atomisation. The second part comprises a literature review of the methods used in the past for the simulation of spray and modelling of droplet size distributions. The characterization of breakup via statistical analysis and different ways to model it are presented in the third part of the chapter. A brief discussion concerning their advantages and disadvantages is included. Finally, the stochastic model devised and implemented in the LES in-house code Boffin is presented, and is validated by application to two test cases. The results of the simulations are compared with experimental data for a typical diesel injection configuration and a spray in cross flows. The Sauter Mean Diameter (SMD) distribution along the axis of injection in a representative diesel engine configuration is compared with the experimental data of Hiroyasu and Kadota [34] and with the DNS, RANS and LES results described by Apte et al [3] in which different breakup models are used. The results of the simulations, including SMD profiles, are also compared with the measurement of Park et al [65] in the spray resulting from a sequence

of droplets injected transversely into a high Reynolds number jet.

4.2 Overview

The utilization of sprays is not new, and in modern society it is extensive enough that almost every engineering application related to combustion uses some form of atomisation. Combustion in gas turbines, rockets, diesel engines and furnaces are only a few examples of spray applications. In all these processes it is often desired to enhance mass-transfer rates by increasing the inter-species surface area. This is one of the goals of atomisation.

The atomisation process is defined in [6] as the one in which bulk liquid is disintegrated into small drops by the acting forces. Lefevre [51] considers atomisation as a disruption of the consolidating influence of surface tension by internal and external forces, which results into the transformation of a liquid column or sheet into relatively small fragments or droplets. These fragments can be stable or undergo to further fragmentation, generating even smaller droplets. The importance of drop size on the combustion process is evident from Equation (3.17) in Chapter 3. Since the evaporation rate of fuel is inversely proportional to the droplets diameter, it is evident that small droplets will evaporate faster, enhancing the production of fuel vapour. Therefore, the atomisation of liquid fuel plays an important role and strongly influences combustion efficiency. An efficient atomisation reduces the size of fuel droplets, leading to higher volumetric heat release rates, smaller evaporation times, easier lightup and wider burning ranges [51]. Furthermore, the size of the droplets in the spray determines the fuel vapour distribution inside the flame and hence the exhaust concentration of pollutant emissions.

An increasing scientific interest in the subject of atomisation is evident in the past two decades. This is lead by the growing attention of industries into combustion efficiency and spray applications. The increasing concern for environmental problems such as the global warming and engine exhaust pollution has emphasised the importance of addressing fundamental issues such as engine efficiency and the reduction of fuel consumption. Moreover, attention is directed to the subject by

the intrinsic difficulties related to the simulation of a multi-phase flow. Liquid fragmentation constitutes an interesting engineering challenge, due to the complexity of the physics involved in the process, which makes spray atomisation a live and practically important problem.

4.3 Atomisation Physics

An extensive treatment of the physics of fragmentation of liquid jets, blobs and droplets in turbulent flow fields is beyond the scope of this work. A short overview of the physics related to liquid fragmentation is reported in order to provide the basic information required for the understanding of the model devised and implemented in the present study.

The usual distinction of liquid break up divides fragmentation into primary and secondary break-up. Primary break up refers to the fragmentation of a liquid jet, or column, due to the oscillations and the growth of perturbations arising from the interaction between the cohesive and disruptive forces acting on the bulk liquid. This process accounts for the initial disruption of the liquid column into liquid fragments, ligaments and large droplets. Secondary break up refers to the further disruption of the unstable drops produced during the initial disintegration. Primary and secondary breakup are equally important, as both influence the final range of drop sizes generated; the processes are illustrated in figure (4.1).

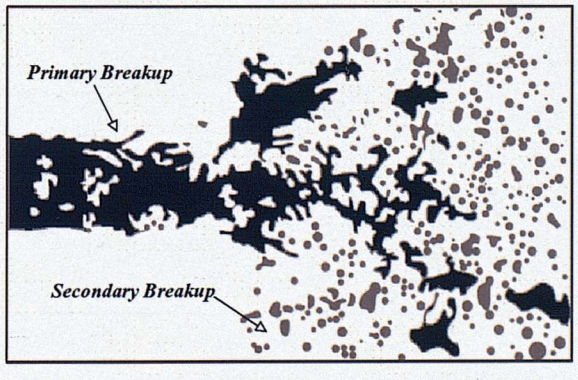


Figure 4.1: Primary and Secondary breakup

4.3.1 Primary Breakup

When a liquid jet enters a gas media from a nozzle, the complex interaction of the liquid phase with the surrounding gas usually generates instabilities. Sometimes oscillations are formed on the surface of the jet and under favorable conditions these oscillations can be amplified and lead to fragmentation. The spray which results from such atomisation can be divided in two main region as shown in figure (4.2) [22]: the dense and dilute spray.

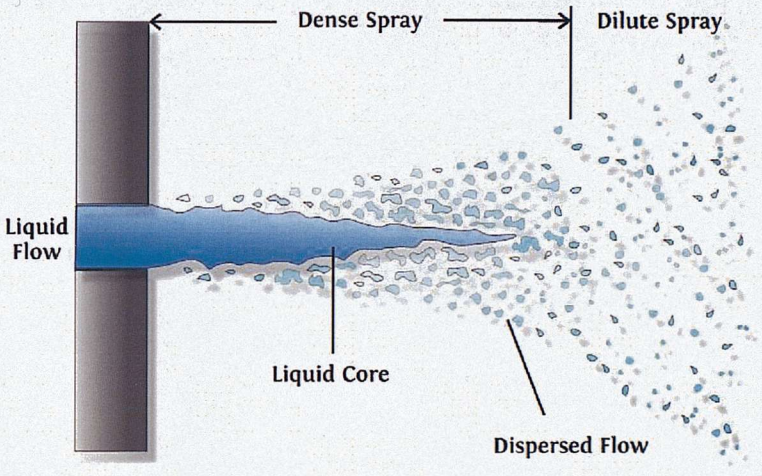


Figure 4.2: Sketch of the near-injection region of a spray in the atomisation breakup regime

There are two regions within dense sprays: the liquid core and the dispersed flow region beyond the surface of the liquid core. The properties of most interest for the analysis of the primary breakup are the length of the liquid core, and the typical drop size. A number of factors can influence those parameters. Rayleigh demonstrated that the initial conditions of the liquid stream, such as the velocity of injection and the velocity profile, play a central role. The presence of gas phase perturbations at the nozzle exit, as well as a relative velocity between the two phase can have a dramatic impact on the length of the liquid core and on the size of the smallest fragments generated. The diameter of the nozzle also exerts an important influence. Experimental studies [14] have shown that the liquid core

length can be expressed as:

$$L_c = C_c(\frac{\rho_L}{\rho_G})^{1/2}d \tag{4.1}$$

where C_c is an experimental constant and d is the diameter of the injector. Primary atomisation involves two different mechanisms depending on the velocity of injection as shown in figure (4.3), [94]. When the discharge velocity is slow (typically of the order of magnitude of 1 m/s), breakup is mostly due to random internal perturbations. The perturbations generate narrow bands on the jet surface which develop into wider bands, leading to the development of droplets (figure (4.3a)). Rayleigh showed that this kind of atomisation can be obtained just with internal perturbations and that the waves that cause it are a function of the liquid surface tension. When the discharge velocity increases (figure (4.3b)), asymmetric wave type distortions form on the surface of the jet due to the aerodynamic forces. Since the air moving along the jet accelerates in the vicinity of convexities and decelerates in the proximity of concavities, a negative pressure develops in the convexities and a positive pressure develops in the concavities. This causes the asymmetric waves to increase their amplitude as they travel away from the nozzle. When the wave amplitude is large enough, tension forces promote the formation of droplets. When a liquid jet is subjected to even higher aerodynamic forces it disintegrates into relatively small droplets. This force depends mainly on the relative velocity between the jet and the gas at the injection, but also on the density of the gas. If the velocity of injection is maintained high enough so that aerodynamic forces are the cause of atomisation, higher values in the gas density will promote smaller droplet diameters. This atomisation mechanism is the one that occurs in most of the applications of atomisers.

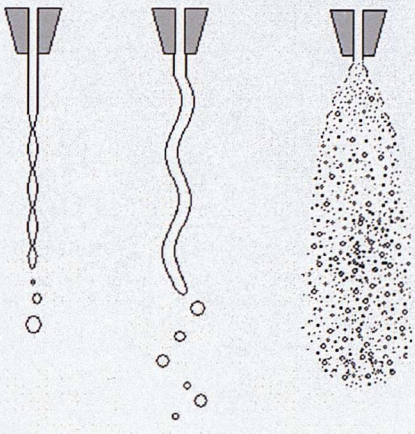


Figure 4.3: Atomisation Mechanism

It must be noticed that because of the Lagrangian methodology adopted in the present work, the interface between gas and liquid cannot be tracked. As a result, primary breakup is neglected and only secondary breakup is taken into account.

4.3.2 Secondary Breakup

Secondary atomisation occurs as a result of interaction of the droplet with some sort of external disrupting forces. When liquid is injected into a gaseous flow and under equilibrium conditions the internal pressure at any point on the drop surface is just sufficient to balance the external aerodynamic pressure [51].

$$p_l = p_A + p_\sigma \tag{4.2}$$

where for a spherical droplet [51]:

$$p_\sigma = \frac{4\sigma}{D} \tag{4.3}$$

The droplet remains stable as long as changes in the air pressure p_A on the droplet surface can be compensated by a change of the corresponding internal pressure p_σ. When the value of p_A increases, the droplets undergoes deformation and the aerodynamic pressure distribution around the droplet changes. In order

to keep p_l constant p_σ must decrease. If the value of the external aerodynamic pressure is too high and can not be compensated by a change of the internal surface tension force, the droplets breaks into fragments. It is evident from equation (4.3) that the value of the internal pressure of the smaller, newly formed droplets, is higher. Depending on p_σ being large enough to compensate for the variation of p_A, the newly born droplets will be stable or undergo further fragmentation. In general, for droplets in a flowing stream the aerodynamic forces can be represented as $0.5\rho_g U_R^2$. The ratio between aerodynamics and surface tension forces expressed in equation(4.3) is an important parameter in atomisation, called the Weber number:

$$We = \frac{\rho_l U^2 D}{\sigma} \tag{4.4}$$

To account for the influence of liquid viscosity, it is common in the literature to use a viscosity group, the Ohnsorge number, defined as the ration $Oh = \frac{\sqrt{We}}{Re}$ or:

$$Oh = \frac{\mu_l}{(\rho_l D \sigma)^{0.5}} \tag{4.5}$$

Numerous studies have considered the dependency of the breakup and deformation regimes on the Weber and Ohnsorge numbers. Figure (4.4) taken from [22] shows this dependency.

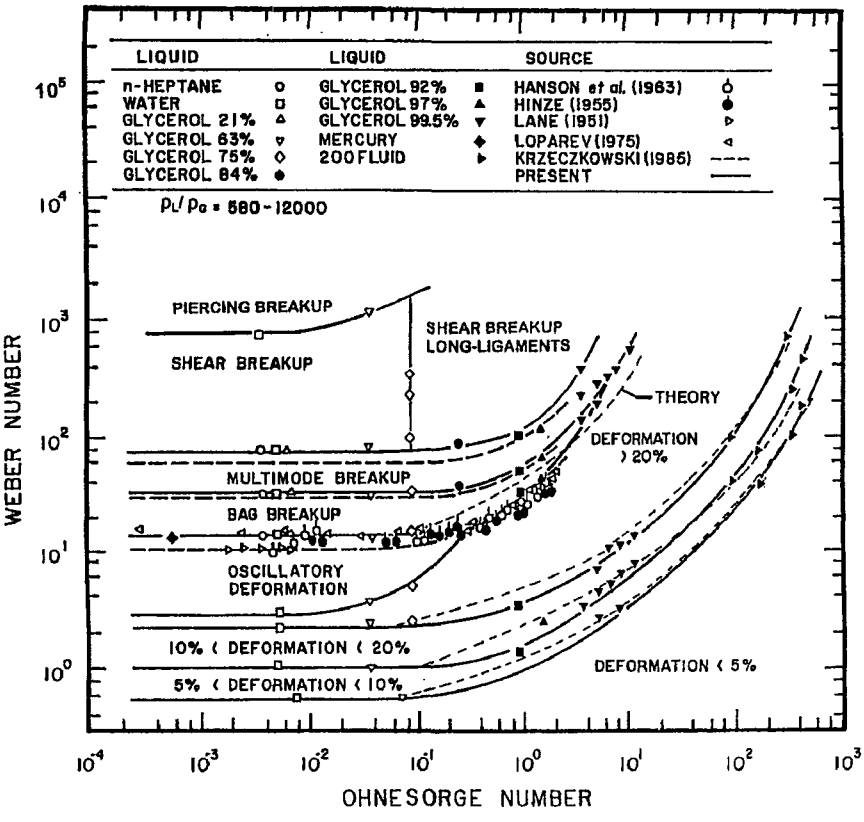


Figure 4.4: Droplets deformation and breakup with Weber and Ohnesorge

An important observation to be made from figure (4.4) is that the values of We required for particular regime transitions are relatively constant for $Oh < 0.1$. Only for $Oh > 0.1$ does the Weber number progressively increases with Oh [75]. The transitions to the deformation regimes are important because they define conditions where drop drag departs significantly from that of a solid sphere. These regimes are defined by the ratio of the maximum (cross stream) dimension to the original drop diameter. The oscillatory deformation regime is defined by conditions where the drop oscillates with a weakly damped amplitude.
The breakup regime observed at small Weber numbers, and when effects of liquid viscosity are small, is usually called bag breakup [22, 37]. This regime involves deflection of the drop into a thin disk normal to the flow direction, followed by deformation of the center of the disk into a thin, balloon-like structure, both of which subsequently divide into drops (figure (4.5)).

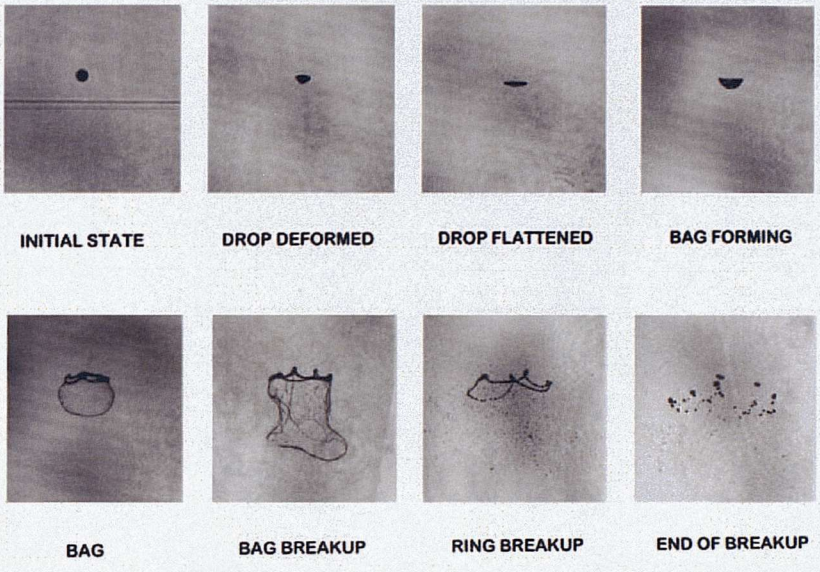


Figure 4.5: Pulse shadowgraphs of secondary breakup in the bag breakup regime (water, We = 15, Oh = 0.0045)

The shear breakup regime is observed at higher relative velocities [36] and is also called the stretching and thinning breakup regime by other authors [51, 65]. This regime involves deflection of the periphery of the disk in the downstream direction, rather than deflection of the center of the disk, and the stripping of drops from the periphery of the disk. Droplets disintegrate at their edges because of a suction stress on the surface of the droplet. This shear stress is due to the high-speed gas flow on the droplet which caused the deformation and the separation of the droplet surface.

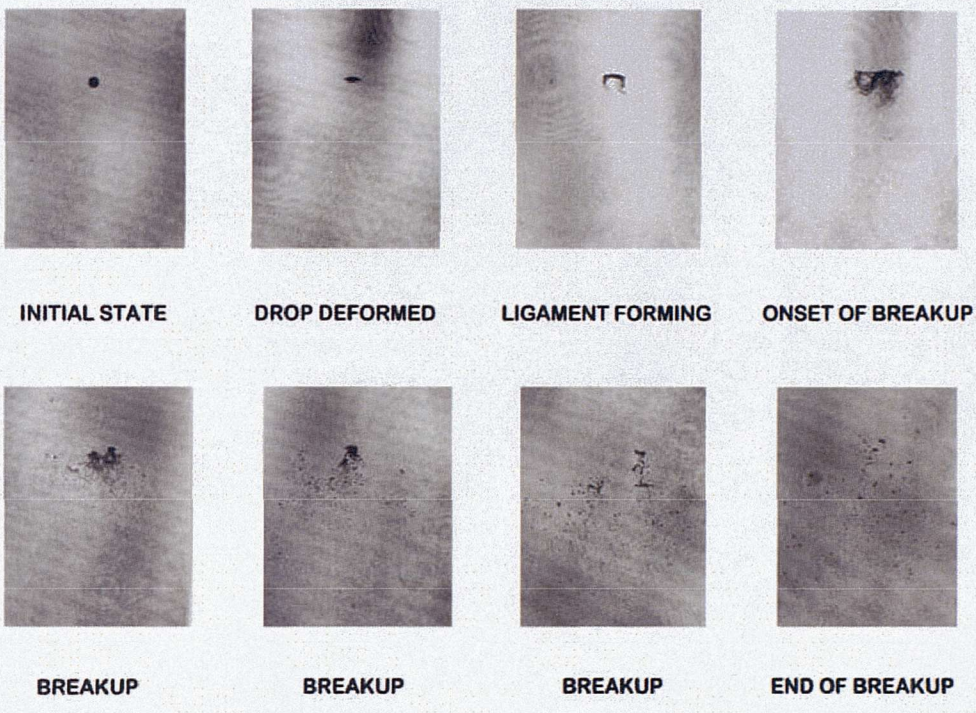


Figure 4.6: Pulse shadowgraphs of secondary breakup in the shear breakup regime (ethyl alcohol, We = 81, Oh = 0.0126). [21]

The transition between the bag and shear breakup regimes is a complex mixture of the two regimes which is usually called the multimode breakup regime. Another complex breakup mechanism has been observed at very large relative velocities between the particle and the gas phase, and this is usually called catastrophic breakup. In this breakup regime, the breakup of the droplet occurs suddenly due to the wave instability on the droplet surface, which is usually classified [50] into Kelvin-Helmholtz or Rayleigh-Taylor waves, depending on the manner in which it is generated (shear stress or droplet acceleration). In [66] five distinct mechanisms of drop breakup are isolated as determined by the initial Weber number. Table (4.1) shows the respective limits of each breakup regime.

In the present work the breakup regimes are divided as reported in [65].

Breakup Regime	Minimum Weber	Maximum Weber
Vibrational breakup	-	12
Bag breakup	12	50
Bag-and-stamen breakup	50	100
Sheet stripping	100	350
Catastrophic breakup	350	-

Table 4.1: Breakup regimes

4.4 Literature Review

A variety of models has been proposed in the literature on liquid sprays. Computational approaches of liquid sprays in turbulent flows are often based on the Lagrangian-Eulerian procedure proposed by [19]. The Eulerian equations for gaseous phase are solved along with a Lagrangian model for particle transport with two-way coupling of mass, momentum and energy exchange. Sometimes the spray is represented by discrete particles which are a sample of the total population, where each computational particle represents a group of droplets possessing the same characteristics (size, velocity, composition) [35]. An Euler-Euler representation, where the description of the history of each particle is replaced by the description of their mean properties, regarding the spray as a continuous fluid is also possible. A relevant work implementing this approach is that of [39]. Droplets are considered to be a continuous fluid interpenetrating and interacting with the gas phase. However, the simplicity of implementation and the non-diffusive character of the Lagrangian approach are the main advantages of using a Lagragian rather than an Eulerian description of the spray.

Atomisation is a complex phenomena and may involve several mechanisms, determined by the initial Weber number, such as vibrational breakup, bag breakup, bag and stamen breakup, sheet stripping and catastrophic breakup. There have been several studies of liquid droplet deformation and breakup [36, 50, 56, 66, 92] in which attention has been focused on the global behavior of the droplets and empirical laws for the breakup process have been defined. Concerning breakup modelling, the most widely accepted mechanism is the one formulated by Reitz

[74, 75] , where it is assumed that surfaces waves form on the liquid phase. Reitz used the wave equation of Taylor to estimate the wavelength and growth rate of the most unstable wave on the surface of the parent droplet thereby defining the conditions where the amplification of the waves would lead to the breakup of the droplets. New droplets are formed based on the growth rate of the wave instability. Amongst the wave breakup models, the Taylor analogy breakup (TAB) [64] is another important and widely accepted approach. The TAB model represents the oscillations of the parents droplets as a spring-mass system with breakup presumed to occur when the oscillations in the parent droplet exceed a critical value. Gosman and Clerides [29] proposed a variation on Reitz's approach in which the initially unstable waves on the jet surface are assumed to be produced by turbulence in the injection nozzle. It is important to point out that the wave instability and TAB models are both deterministic models, with "single scale" production of droplets. In several practical combustion applications the high relative velocity between droplets and gas phase may result in the formation of droplets with a very wide spectrum of diameters. The TAB and wave instability models may not be able to capture this behavior. Tanner, [88] developed an enhanced TAB model (ETAB), which achieves better performances by deriving the parameters of the product droplet size via a breakup cascade modeled by an exponential law.
In the framework of definition of a suitable breakup model, the prediction of the representative droplet diameter (the Sauter Mean Diameter for example), and the prediction of the droplet size distribution are issues of fundamental importance. Since the 1930s several methods of modelling droplet size distributions have been proposed. A classical approach is the empirical method, based on a curve which is used to fit data collected for a wide range of atomizers and operating conditions. The curve extrapolated from the empirical data is used to characterize the distribution of droplet sizes. A complete review of the available methods for modelling drop size distribution is provided by [5]. As first shown by Kolmogoroff [16, 28] the log-normal distribution arises when considering the theoretical distribution that is produced by continuous random partitioning of a set of solid particles.

The distribution can be written as:

$$f_0(D) = \frac{1}{D(ln\sigma_{LN})\sqrt{2\pi}} exp\{\frac{1}{2}\left[\frac{ln(D/\bar{D}}{ln\sigma_{LN}}\right]^2\} \tag{4.6}$$

where f represents the droplet distribution and the subscript 0 refers to a number distribution. $\bar{D}$ is the logarithmic mean size of the distribution and σ_{LN} represents the width of the distribution. One of the most widely used distribution is the Rosin-Rammler distribution, defined as:

$$f_0 = q\bar{D}^{-q}D^{q-1}exp[-(D/\bar{D})^q] \tag{4.7}$$

where f_0 is the number distribution, $\bar{D}$ represents the mean of the distribution and q provides a measure of the width. Small values of q are associated with sprays with a broad size distribution, and large values with narrow sprays. The Nukiyama-Tanasawa is also a quite common distribution and its number distribution can be written as:

$$f_0(D) = aD^p exp(-bD^q) \tag{4.8}$$

where b, p and q are adjustable parameters which control the width of the distribution and the location of the mean, and a is a normalizing constant.

As alternatives to empirical methods, several analytical approaches have been proposed. Maximum Entropy methods were developed in the late 1980s and early 1990s and have recently received attention from several investigators [82]. The Maximum Entropy method treats spray formation as a completely non-deterministic process that can be modelled using the principle of entropy maximization subject to suitable constraints. The atomisation process is seen as a 'black box' which turns a bulk liquid into droplets with a specific distribution. Even though there are an infinite number of possible droplets distributions, only one will satisfy the principles of mass and energy conservation and minimize the entropy. Different from the Maximum Entropy method, which is completely non-deterministic, is the discrete probability function (DPF) approach, an analytical method, which divides the spray formation process into deterministic and non-deterministic components. The deterministic portion describes the breakup of the gross fluid structure, whilst the non-deterministic part describes the effect

of fluctuating initial conditions on the resulting drop size distribution. However, most of these models are not suited to LES of sprays in practical applications to which the present work is directed.

Recently, stochastic models inspired by the work of Martinez-Bazan et al. [58, 59] have gained increasing popularity, due to their ability to predict the essential global features of complex spray phenomena without being computationally too expensive. A comprehensive review of some of the most relevant stochastic models for particle breakup is provided by Lasheras [47] , where a population balance treatment for droplet breakup is formulated. Probably the first statistical formulation able to describe the complex disorder encountered in sprays was proposed by Williams [95]. Williams' approach assumes that only one parameter, the radius r, is sufficient to characterize the size and shape of the particles. Under this assumption Williams formulation states that the rate of change of the probable number of droplets is related to the particle growth rate, the particle acceleration, the formation of new particles and the effect of collisions. The probable number of droplets with radius between r and $r + dr$ located in the position range $d\mathbf{x}$ about $\mathbf{x}$, with a velocity in the range $d\mathbf{v}$ about $\mathbf{v}$ at time t is :

$$f(r, \mathbf{x}, \mathbf{v}, t) dr d\mathbf{x} d\mathbf{v} \tag{4.9}$$

then the rate of change of the probable number of droplets is:

$$\frac{\partial f}{\partial t} = -\frac{\partial}{\partial r}(Rf) - \boldsymbol{\Delta}_{\mathbf{x}} \cdot (\mathbf{v}f) - \boldsymbol{\Delta}_{\mathbf{v}} \cdot (\mathbf{F}f) + Q + \Gamma \tag{4.10}$$

where $R \equiv dr/dt$ is the particle growth rate, $\mathbf{F} \equiv d\mathbf{v}/dt$ is the particle acceleration, the source term Q may account for the formation of new particles, and Γ represents the rate of increase of the function f due to droplet collisions. Droplets breakup is taken into account through the terms which refer to particle formation and destruction.

Following the work of Williams, the Boltzmann-type equation (4.10) , often known as the population balance equation, is used by Martinez and Lasheras in order to formulate an innovative stochastic model for breakup. In [47] the authors consider a test case in which air bubbles are injected into a water vessel. The proposed stochastic model is able to describe the temporal and spatial rate of

change of the probable number of droplets with a well defined position, velocity and size through the definition of a breakup frequency and a pdf distribution of breaking droplets.

Another interesting approach has been developed by [3] based on a stochastic model for the breakup combined with Large Eddy Simulations of the continuous phase. The characteristic radius of droplets at a given position is assumed to be a time-dependent stochastic variable. An initial distribution function is assigned and the breakup of droplets is viewed as the temporal evolution of the distribution function. The size of the newly formed droplets is sampled from the distribution sampled at a characteristic breakup time scale of the parent drop. The model is based on the Kolmogorovs stochastic theory of the breakup of solid particles in the framework of uncorrelated breakup events [28]. The atomisation is represented as a random discrete process where the probability of breaking each parent particle into a given number of parts is independent of the size of the parent particle. Another kind of approach is that of [55], where the implementation of the finite stochastic breakup model (FSBM) of prefilming air-blast atomizers for the secondary atomisation is proposed. In the FSBM a breakup can occur only if the size of the mother particle is larger than a critical diameter and the fragmentation generates two droplets of diameters chosen randomly with a uniform probability distribution.
It must be noted here that most of the models presented in the present literature review are not feasible from a computational point of view when LES is to be applied. Indeed, most of the deterministic models proposed require information about the liquid interface which are simply not available in LES approaches. Level set methods or similar interphase tracking methodologies are often used when DNS is applied to the simulation of the gas field. However, such applications are beyond the aim of the present work. The Lagrangian particle tracking methodology adopted assumes that droplets are point sources. Moreover, because the size of the applied LES filter is much larger than the biggest droplet, the liquid-gaseous interface interaction can not be reproduced. Methods for the prediction of droplets size distribution, such as empirical methods or entropy

based models, have proved in the past to be unreliable and not sufficently accurate. In this regard, the application of stochastic methods to sprays in conjuction with LES makes sense.

4.5 Present breakup model

4.5.1 Overview

The model for breakup consists of a stochastic formulation which reproduces the effects of the sub-grid scale motions on the droplet secondary breakup. Each breakup event is defined in a statistical manner through a Poisson release process and the evolution of the radius of the droplets is defined by a probabilistic approach. The breakup of stochastic particles is related dynamically to the flow field through the breakup frequency and the local Weber number, while each breakup event is defined by a life expectation procedure, governed by a Poisson distribution of characteristic frequency equal to the breakup frequency. The probability density function (*pdf*) of the radius of droplets arising from the atomisation is defined in a stochastic way and is related to the rate of dissipation of kinetic energy and to the radius of the breaking particles. A surface energy model based on a balance of the stresses existing at the particle surface is adopted.

4.5.2 The Model

The conditional Lagrangian rate of change of particle number, $\dot{\mathcal{N}}$ is used to represent droplet breakup processes. Stochastic particles are implemented in order to represents ensemble of liquid droplets. Each stochastic particle contains a given number of droplets, n that represent the probable number of particles with radius in the range $r < r' < r + dr$, located within the spatial position $\mathbf{x} < \mathbf{x}' < \mathbf{x} + d\mathbf{x}$ and with a velocity $\mathbf{v} < \mathbf{v}' < \mathbf{v} + d\mathbf{v}$ at time t. More precisely, the variation in the number n arises only through droplet nucleation, coalescence and breakup. There have been numerous studies of the dynamics of particles in dispersed flow systems and much of this work can grouped under the heading the population balance equation (PBE) model [15, 73]; a recent and comprehensive review is provided by

Rigopoulos [76]. Examples of applications of the PBE to droplet breakup include the works of Williams [95], Lasheras et al [47] and Martinez-Bazan et al [58, 59].

The rate of change of the number of droplets in a stochastic particle, $\dot{\mathcal{N}}$ is equal to the rate of change of the number of particles due to breakup. The latter can be expressed [47] as the sum of the birth rate of particles of size r resulting from the breakup of larger ones, and the death rate of particles of size r due to their breakup into smaller ones :

$$\begin{aligned} \dot{\mathcal{N}} &= \int_r^\infty q(r_0) f(r, r_0) \omega(r_0, We) n(r_0) dr_0 \\ &- \omega(r, We) n(r) \end{aligned} \tag{4.11}$$

where $\omega(r, We)$ is the break up frequency of particles of size r; $q(r)$ is the mean number of particles resulting from the break up of a mother particle of size r_0; $f(r, r_0)$ is the size distribution of daughter particles formed from the breakage of a mother particle of size r_0. In order to close equation (4.11), a suitable model for the breakup frequency $\omega(r)$, the expected number of daughter particles $q(r)$ and the *pdf* of daughter particles $f(r, r_0)$ must be defined. The average number of particles formed from the breakup at time t is frequently known and following Ramkrishna [73] it is assigned the value 2.

4.5.3 Breakup Frequency

The break-up frequency of a particle of diameter D is defined by [15] as:

$$\omega(r_p, We) = \frac{1}{t_b} \frac{\Delta N(r_p)}{N(r_p)} \tag{4.12}$$

where $N(r_p)$ is the total number of particles of size D, t_b is the break-up time and $\Delta N(r_p)/N(r_p)$ represents the fraction of drops breaking.
The present model for breakup splits the breakup frequency in two terms:

$$\omega(r_p, We) = \omega_d(r_p, We) + \omega_s(r_p, \epsilon) \tag{4.13}$$

where $\omega_d(r_p, We)$ is the '*deterministic component*' of the breakup frequency, defined according to O'Rourke and Amsden [64] and Faeth et al [22] and is dynamically related to the local flow properties through the velocity and density of the

gas phase:

$$\omega_d(r_p, We) = 0.5C_b(We)\sqrt{\frac{\rho_g}{\rho_\ell}}\frac{|\tilde{\mathbf{u}} - \mathbf{v}_p|}{r_p} \tag{4.14}$$

with $C_b = \sqrt{1/3}$.

The second term represents the *sgs* contribution and is based on a work of Martinez-Bazan et al [58, 59] who studied the break up of air bubbles in a stirred vessel. In this case the dispersed phase is transported by the continuous phase with no relative velocity between bubbles and water; hence fragmentation is due only to turbulent velocity fluctuation. Lasheras et al consider a gaseous dispersed phase and a liquid continuous phase whereas in this work we are concerned with liquid droplets in a gas continuous phase. Nevertheless the formulation of Martinez-Bazan et al may be extended to the present case with some adjustments of the model constant. In equation (4.13) the *sgs* component to the breakup frequency is defined by relating it to the ratio of the aerodynamic disruptive forces acting on a droplet and the stabilizing surface forces, characterized by the surface tension of the liquid.

In order to express the 'stochastic component' of the breakup frequency as a function of the rate of dissipation of kinetic energy, $\Delta N(D)/N(D)$ of equation (4.12) is modeled as

$$\frac{\Delta N(r_p)}{N(r_p)} = exp\left(-\frac{E_c}{\bar{E}}\right) \tag{4.15}$$

where r_p is the droplets radius, $E_c = \pi\sigma D^2$ is the surface energy and $\bar{E} = c_2\rho D^3\overline{\Delta u^2}(D)$, with $\overline{\Delta u^2}(D)$ the mean squared value of the velocity fluctuations between two points separated by a distance $D = 2r_p$. It is assumed that the turbulence is locally homogeneous and isotropic and that the initial size of the droplets is in the inertial subrange, $\eta < D < L_0$, with η being the Kolmogorov microscale and L_0 the integral scale. With this assumption the velocity fluctuations can be written as [27]:

$$\overline{\Delta u^2}(D) = \overline{|u(x+D,t) - u(x,t)|^2} = \beta(\epsilon D)^{2/3} \tag{4.16}$$

where ϵ is the rate of dissipation of kinetic energy, β is an experimental constant and, as stated above, D is the diameter of the droplet. The minimum

surface pressure necessary to restore the deformation of a droplet of diameter D can be written as:

$$\tau_s(D) = 6\frac{\sigma}{D} \tag{4.17}$$

while the aerodynamic deformation force can be written as:

$$\tau_t(D) = 0.5\rho\overline{\Delta u^2}(D) \tag{4.18}$$

when $\tau_t > \tau_s$ the droplet deforms and eventually breakup. Therefore, by imposing $\tau_t = \tau_s$, from equation (4.16) it is possible to find the critical diameter D_c:

$$D_c = \left(\frac{12\sigma}{\beta\rho}\right)^{3/5} \epsilon^{-2/5} \tag{4.19}$$

Droplets with $D > D_c$ will be stable and do not break. As stated in [47] *'the critical diameter D_c applies to the mother particle and defines the minimum particle size for a given dissipation rate of turbulent kinetic energy for which break-up may occur'*. The minimum diameter, on the other hand, applies to the daughter particles and defines the distance over which the turbulent normal stresses just balance the confinement forces of a mother particles of size D_0. The minimum diameter, therefore, gives the minimum length over which the underlying turbulence can pinch off a portion of the mother particle. This length is not arbitrarily selected but, rather, is based on kinematics. The minimum diameter can be obtained by equating the surface energy of a bubble of size D to the deformation energy between points a distance D_{min}, being $0.5\rho\beta\epsilon^{2/3}D_{min}^{2/3} = 6\sigma/D$, thus:

$$D_{min} = \left(\frac{12\sigma}{\rho\beta D}\right)^{3/2} \epsilon^{-1} \tag{4.20}$$

The characteristic breakup time is proportional to the ratio between the droplet diameter and the characteristic breakup velocity: $t_b \propto D/u_b$. The breakup velocity is defined in [47] as the difference between the pressure produced by the turbulent fluctuations on the surface of the particle, $1/2\rho\overline{\Delta u^2}(r_p)$, and the restoring pressures caused by surface tension, $6\sigma/D$.

$$u_b = \sqrt{\overline{\Delta u^2}(r_p) - 6\frac{\sigma}{\rho r_p}} \tag{4.21}$$

Therefore, from equation (4.16) the breakup frequency can be written as:

$$\omega_s(r_p, \epsilon) = K_g \frac{\sqrt{\beta(\epsilon 2r_p)^{2/3} - 6\sigma/\rho_g r_p}}{2r_p} \tag{4.22}$$

In absence of external forces, surface tension tends to pull the liquid into a sphere minimizing surface energy with a equipotential shape. A droplet travelling in a turbulent flow undergoes deformation and fragmentation when the aerodynamic forces disrupt the consolidating influence of the surface tension. Fragmentation can be caused by the aerodynamic pressure due to the relative velocity between the gas and liquid phase, as well as by the interaction of the droplet with small turbulent scales. LES provides only filtered values of continuous phase velocities and consequently the influence of eddying motions with a length scale smaller than the applied filter width is unknown. However, there are many flow situations where a large droplet is transported in a region of fully developed turbulence, where the average slip velocity between the droplet and the gas phase is small. In this case breakup occurs by means of the interaction of the small scales with the droplet surface.
The dependence of the two breakup frequency components on the droplets diameter is shown in figure (4.7) and (4.8) for a typical turbulent test case.
It can be noticed that the deterministic component increases dramatically as the diameter decreases. However, since droplets with diameter smaller than the critical value can not break, we will assume that the maximum value of such function is for $D = D_c$. Moreover, the deterministic frequency decreases monotonically with the diameter, going to zero as the diameter goes to infinity.

The stochastic component of the breakup frequency is zero for $D \leq D_c$ and increases rapidly for droplets just over the size of the critical diameter, up to a maximum value. The diameter corresponding to the maximum stochastic frequency is $D_{gmax} = 1.63 D_c$. For droplets of diameter $D > D_{gmax}$ the function decreases monotonically with the droplets size. The maximum value ω_{max} is given by

$$\omega_{max} \propto (\sigma/\rho)^{-2/5} \epsilon^{3/5} \tag{4.23}$$

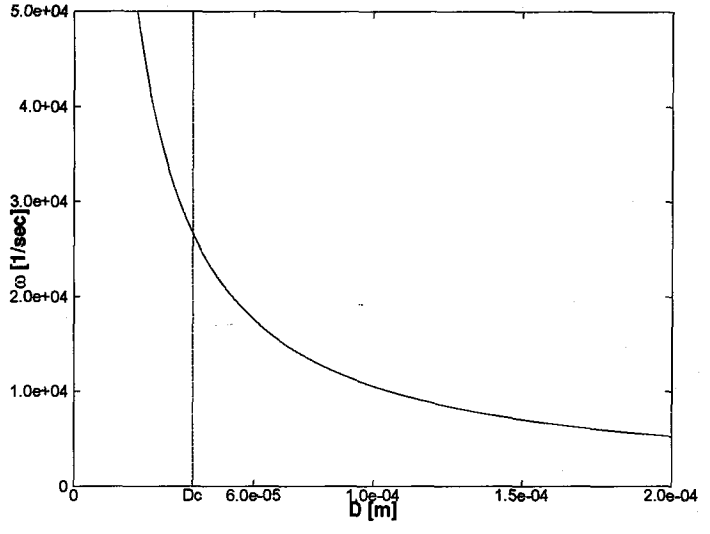


Figure 4.7: Deterministic component of the breakup frequency versus droplet diamter, $\rho_g = 1.2$ kg/m^3, $\rho_l = 817$ kg/m^3, $r_o = 100$ μm, $\sigma =$ N/m

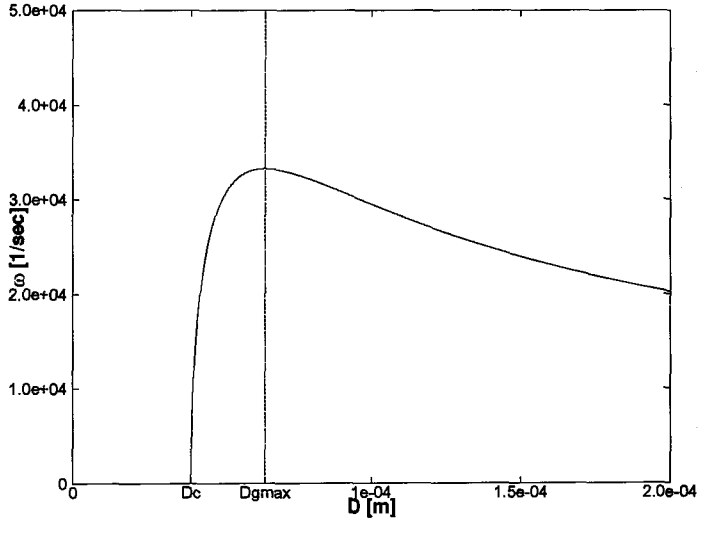


Figure 4.8: Stochastic component of the breakup frequency, $\rho_g = 1.2$ kg/m^3, $\rho_l = 817$ kg/m^3, $r_o = 100$ μm, $\sigma =$ N/m

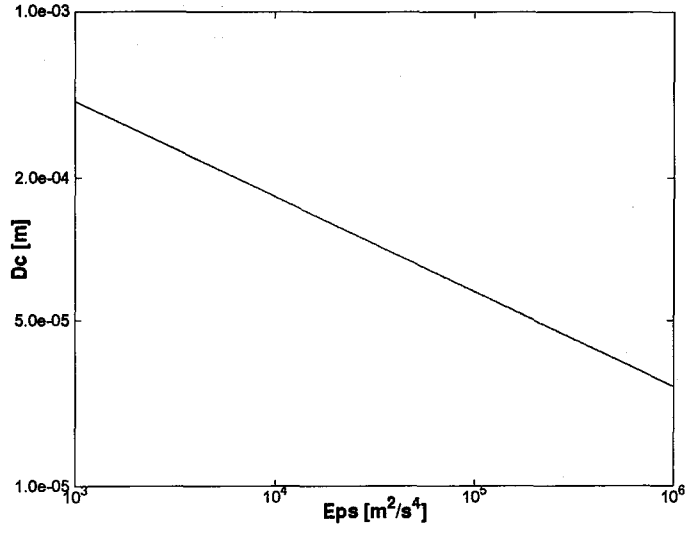
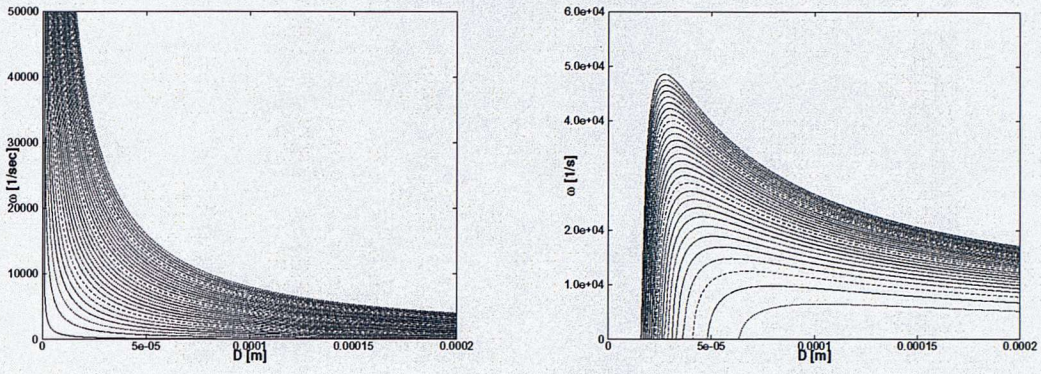


Figure 4.9: Critical diameter versus rate of dissipation of turbulent kinetic energy

When the droplet diameter is much bigger than the critical value, hence $D >> D_c$ the surface tension becomes very small and the breakup frequency tends to its asymptotic value, proportional to $\epsilon^{1/3} D^{-2/3}$.

The critical diameter decreases as the rate of dissipation of kinetic energy increases, being ϵ a measure of the turbulence of the flowfield. Furthermore, the diameter for which the stochastic component of the breakup frequency is maximum depends on ϵ as well.

Figure (4.10) shows the deterministic and stochastic component of the breakup frequency respectively at different relative velocity and rate of dissipation of kinetic energy ϵ. As the relative velocity between the gas and the droplet increases or the rate of dissipation ϵ, so do both the components. Higher relative velocities or ϵ increase the likelihood of the droplets to break.



(a) Deterministic Component (b) Stochastic Component

Figure 4.10: Deterministic component at different relative velocities (a) - Stochastic component at different relative ϵ (b)

4.5.4 Discrete Poisson release process

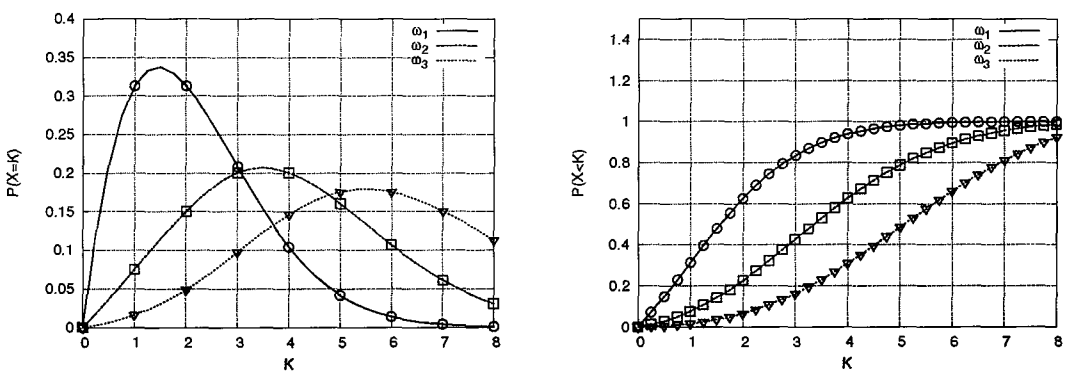
Before introducing the model for the pdf of diameters of the daughter droplets, something must be said on the breakup process. The treatment of droplet breakup from a trajectory point of view, using equation (3.6), requires additional modelling in order for it to be computationally feasible. When a trajectory point of view is adopted, and the break up of a certain amount of droplets has been experienced, the daughter particles produced should a priori follow their own new independent trajectories in phase space. If the break up was modelled as a continuous process, new trajectories, representing the emission of daughter particles, should be released continuously from the mother trajectory. The computational load of such a task would be very high and for this reason a discrete Poisson release process is used.

The probable number of droplets in a stochastic particle which are likely to experience fragmentation is computed each time step as specified by the second term of the right hand side of equation (4.11). However, the stochastic particles do not break continuously. Instead, the global number of droplets which are broken at every instant is stored as: $N^{broken} = \int_{t_0}^{t} \omega(r) N_t dt$, where t_0 and t are respectively the time of birth of the particle and the current time, while N_t is the number of droplets at the instant t. A mother stochastic particle

with characteristic radius r_0 is presumed to fragment if its age is larger than its expected life, defined by a Poisson distribution with characteristic frequency equal to the breakup frequency. The Lagrangian rate of change of the number of droplets represented by a stochastic particle due to the Poisson release process can be expressed as:

$$\delta N_t = -N^{broken} \delta C_t$$

and δC_t is zero if the age of the particle is smaller than the expected life and one otherwise. The expected life is computed [7] as the random variable $pdf(T_{split} = t) = \omega(r)e^{-\omega(r)t}$. A Poisson process is a procedure which is widely implemented in statistics to model random incomes in time and space. Several important probability distributions arise naturally from this process: the Poisson distribution, the exponential distribution, and the gamma distribution. An extensive treatment of all of them can be found in [25]. In the present work the Poisson distribution is used to compute the expected number of breakup occurrences, from which the expected life of each stochastic particle is defined. The pdf of the distribution and relative cdf of the Poisson distributions, shown in figure (4.11) for a typical case, allow the extraction of a random outcome using the inverse transformate sampling technique. This random outcome is divided by a mean rate of fragmentation (essentially a time averaged breakup frequency) so that the result [25] represents the expected time of life of the liquid droplet.



(a) Pdf (b) Cdf

Figure 4.11: Poisson distribution

4.5.5 Pdf of diameters for the daughter particles

Historically, there have been three predominant approaches [5, 47, 82] to the modelling of $f(r, r_0)$. These are statistical models, phenomenological models based on the change in surface energy of a breaking particle and hybrid models, which are based on a combination of both. In the present work a surface energy model, based on a stress balance, has been adopted.

When a mother particle meets the conditions specified in section (4.5.4) and breaks, $q(r)$ stochastic daughter particles with characteristic radii r_1 and r_2 are generated. The number of breaking droplets inside the mother stochastic particle is equally distributed into the two newly added stochastic particles. The daughter particle probability density function of Lasheras et al [47] is used to determine the radii r_1 and r_2:

$$f^*(r^*) = \frac{[r^{*2/3} - \Lambda^{5/3}][(1 - r^{*3})^{2/9} - \Lambda^{5/3}]}{\int_{r^*_{min}}^{r^*_{max}} [r^{*2/3} - \Lambda^{5/3}][(1 - r^{*3})^{2/9} - \Lambda^{5/3}]dr} \tag{4.24}$$

where $r^* = r_1/r_0$, $\Lambda = r_c/r_0 = (r_{min}/r_0)^{2/5}$, $r_{min} = 0.5(12\sigma/(\rho\beta 2r_0))^{3/2}\epsilon^{-1}$ and $r_c = 0.5(12\sigma/(\beta\rho))^{3/5}\epsilon^{-2/5}$. The radii r_1 and r_2 are related by conservation of mass:

$$r_2 = r_0\left[1 - \left(\frac{r_1}{r_0}\right)^3\right]^{1/3} \tag{4.25}$$

as are the radii r_{max} and r_{min}. The method adopted to generate random radii consistent with the given probability distribution function is Inverse transform sampling discussed in appendix B. The variation of the probable number of droplets of the stochastic particle due the droplets of radius $r^* >$ r which break exactly into a droplet of radius r (the so called '*rate of birth*' of equation (4.11)) is added to $n(r, t)$ by merging the stochastic particle with other newly formed stochastic particles with approximatively the same position and dimensions. The pdf as expressed in equation (4.24) is sensitive to the choice of the rate of dissipation of the kinetic energy as shown in figure (4.12) and is an aspect that is extensively commented in the literature.

When a stochastic particle enters a region of high turbulence the probability that small drops are "stripped" from the surface of the liquid is relatively high.

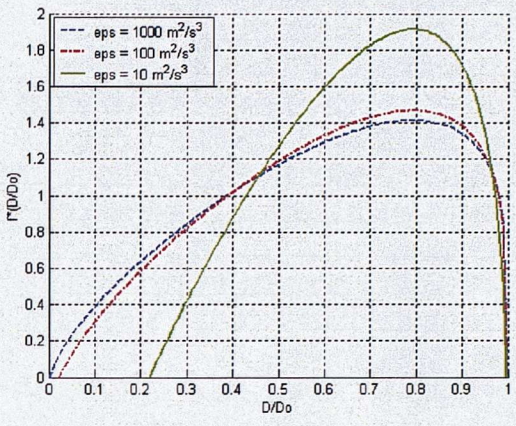


Figure 4.12: Dimensionless pdf of daughter parcels indicating evolution of the pdf with dissipation rate of turbulent kinetic energy, $\rho = 1000\frac{kg}{m^3}$ $r_o = 1.5mm$ $\sigma = 0.072\frac{N}{m}$

Hence the probability is large and thus the formation of small droplets is likely. On the other hand, if the stochastic particle travels into a "quiescent" region, it is more likely that the fragmentation would generate big droplets. When ϵ increases r_{min} decreases, making the formation of smaller daughter particles more probable. Indeed a larger value of ϵ implies that the underlying turbulence is more intense, leading to an increase in the transfer of energy into the smaller scales, [47]. In the case of a mother stochastic particle as its radius r_0 increases an increasing fraction of eddies in the inertial subrange will have sizes that are smaller than the mother particle. Therefore, the probability of creating smaller daughter particles increases. Figure (4.13) from [47] shows the evolution of the pdf of daughter diameters with different $D_0 = 2r_0$:

The presented model has the potential to reduce the computational cost of the simulation, with respect to other breakup models. However this comes at a cost. Whilst the Poisson release process, along with the stochastic particle treatment, reduces the overall computational effort of the simulations the stochastic discontinuous treatment is usually slow to converge and requires longer run times to give a reliable averaged solution.

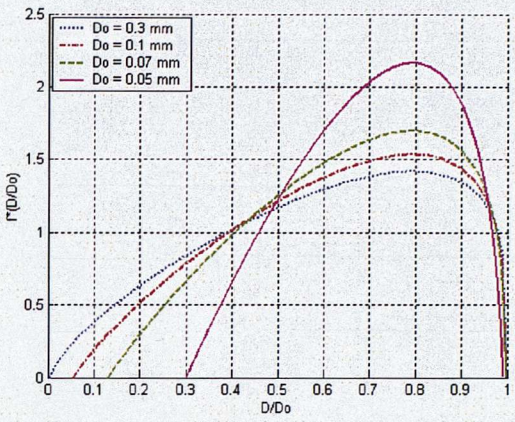


Figure 4.13: Dimensionless pdf of daughter parcels indicating evolution with the radius - $\rho = 13.57kg/m^3$, $\epsilon = 200000\frac{m^2}{s^3}$, $\sigma = 0.0295N/m$

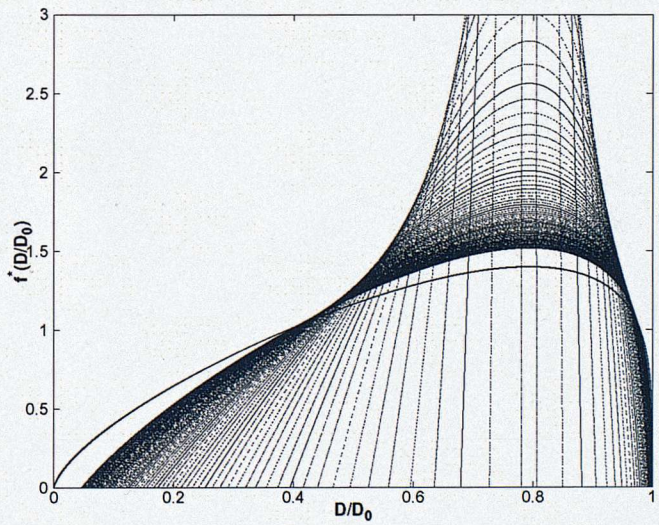


Figure 4.14: Dimensionless pdf of daughter parcels indicating evolution with the diameter collected approximatively 1 million breakups

Finally, figure (4.14) shows a collection of 1 million different pdf distributions generated during the breakup of droplets in the MERCATO test case, to be described later. It can be noticed that even if the shape of the pdf varies greatly, most of the breakup occurs in similar conditions so that the resulting pdf is quite similar.

4.6 Results

The particle breakup model described above is combined with a conventional LES, using a Smagorinsky sub-grid model, to simulate the droplet characteristics in two configurations. In both the cases the LES approach implements a standard Smagorinsky model with the model constant set to 0.12. The drag coefficient of the droplets is modified in order to take into account of droplet deformation as reported in section (3.3) of chapter (3). Droplets vaporisation is neglected.

4.6.1 Diesel spray in still flow

The first case to be considered corresponds to the experimental diesel injector study of Hiroyasu and Kadota, [34] where diesel fuel is injected into a closed cylinder, of length 13.8 cm and diameter 5.6 cm, containing pressurised nitrogen at ambient temperature. The injector comprises a single hole nozzle. Since the chamber temperature is low, evaporation of the liquid fuel is negligible, allowing the study of droplet breakup alone.
The injection methodology is an important issue which must be properly addressed before proceeding with the description of the experiment. The physics of the liquid jet injection is indeed very complex (see 4.3.1). Numerical studies of this problem can use several approaches, and the most common methods are reported in figure (4.6.1). Because of the importance of primary and secondary breakup, a *'direct simulation'* using an interface tracking method [32, 33] would capture most of the physics involved. With this approach the complex interactions between the liquid and gas phase are simulated, leading to an accurate

description of primary and secondary breakup. However, as already pointed out earlier, such methods are often unfeasible for practical applications because of the high computational cost required. One example of a simplifying approach is the *'complete secondary breakup modelling'* as reported by [3] in which a Lagrangian methododology is adopted and the liquid column in not simulated while only secondary breakup is taken into account. In this case, droplets of the same size are injected into the flow, and the breakup is simulated only in the form of secondary atomisation. Another interesting procedure is given by [69] who combined the Lagrangian methodology with empirical correlations. The authors used simple laws for the column breakup in order to derive as initial droplet size distribution (see appendix C). From the initial distribution breakup is simulated numerically. A method that combines an empirical model for the liquid column with a model for secondary breakup has been investigated by Senoner, [83]. The simplest approach is the *'modelled droplet size distribution'* which completely neglects primary and secondary breakup. Instead, atomisation is modelled through a droplet size distribution which can be derived with empirical studies based on the injector type and the characteristics of the flowfiled. Being the simplest approach, the latter is also the least accurate.

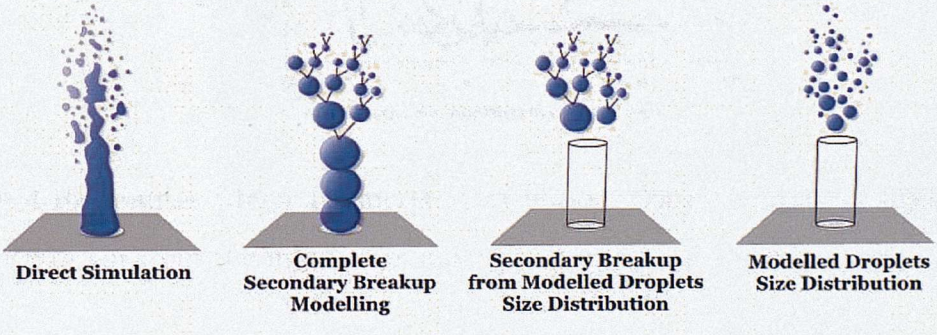


Figure 4.15: Injection methodologies

Similarly to [3], in the present simulation large droplets of diameter 300 μm corresponding to the nozzle diameter are injected and the time step is held constant at 1.5 μs. Initially, the nitrogen is quiescent but recirculation zones eventually arise through momentum transfer from the liquid jet to the gas-phase. A single case at a pressure of 1.1 MPa is simulated. The mass flow rate of the liquid

is obtained from the injection velocity, nozzle diameter and the time of injection. The diesel fuel density is $840 kg/m^3$, the surface tension is 29.5 mN/m, the gas pressure is 1.1 MPa and the density of the gas phase is thus 13.57 kg/m^3. The viscosity of nitrogen is 1.77×10^{-05} kg/ms and its temperature is 20 C. As a consequence droplets are injected with a velocity of 102 m/s at a position corresponding to $x = 0$, $y = 0$ and $z = 0.0002$ m. The results of the simulations are presented in figures (4.16)-(4.18). The variation of the Sauter Mean Diameter (SMD) of the droplets along the axis of injection are compared in figure (4.16) with results taken from [3], in which the authors present the data obtained for the very same test case using several breakup models. The breakup models used in the comparison are presented in the literature review of section 4.4. A single point representing the experimental findings is also presented.

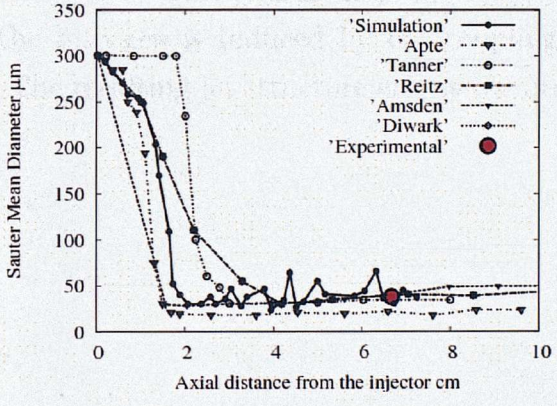


Figure 4.16: Sauter Mean Diameter distribution along the axis of injection - Distance in cm from the injector (x axis) SMD in μm (y axis)

The simulated spray penetration, displayed in Figure (4.17), is also in very close agreement with the measured data.

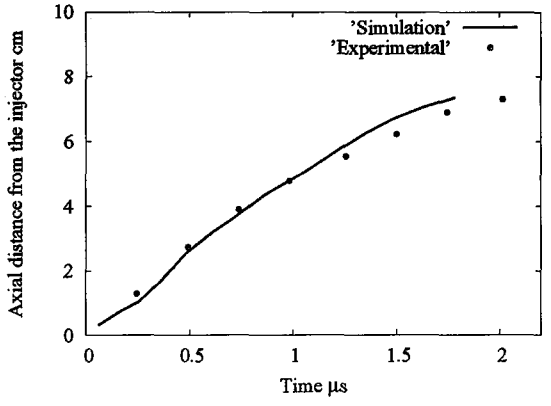


Figure 4.17: Spray penetration, time in μm, distance in cm

Figure (4.26) shows an instantaneous snapshot of the spray with both the droplets and the flow field of the continuous phase being displayed. The flow and turbulence of the nitrogen is induced by the coupling of the liquid phase with the gas phase. The resulting jet structure effects the droplets dispersion and atomisation.

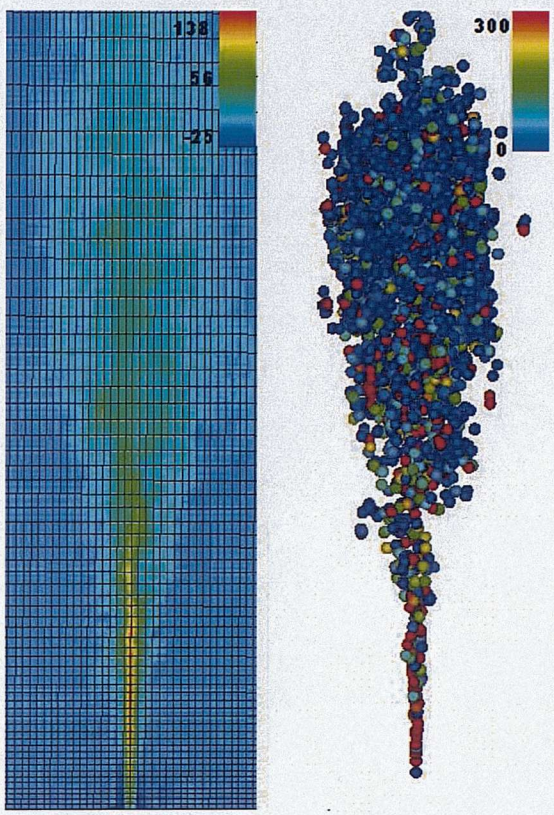


Figure 4.18: Snapshot of the diesel injection - Left gas phase axial velocity contour [m/s] - Right droplets colored by diameter [μm]

4.7 Atomisation of mono-dispersed diesel droplets in a cross-flow air stream

The second case to be considered corresponds to the experimental investigation of Park et al, [65] in which a sequences of diesel droplets are injected at right angles to a high Reynolds number air jet. A schematic diagram of the test case is presented in figure (4.19).

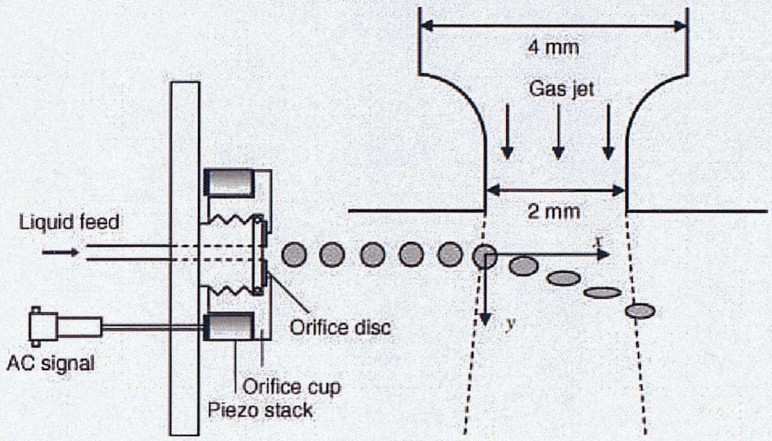


Figure 4.19: Schematic diagram of the experimental droplet generator and gas nozzle

The droplets are generated by a vibrating orifice injector which results in droplets of approximatively uniform size (around 180 μm) being injected a velocity of 13.4 m/s. The air jet emanates from a nozzle of inner diameter 2 mm and the injector is located 1.5 mm downstream of the nozzle exit. Because of the rounded passage feature and the dimensions of the nozzle, the boundary-layer effects are minimized, ensuring that the thickness of the shear layer penetrated by the drops at the edge of the jet is as thin as possible. The droplets transverse the air jet and consequently disintegrate and are deflected. The atomisation results in a variety of different diameter droplets. As can be seen in figure(4.20), the experimental measurement points are located at intervals of 2mm in both axial and radial directions within the range in which the breakups actively occur. The origins of the z and r coordinates of the simulation are placed accordingly with the experimental ones.

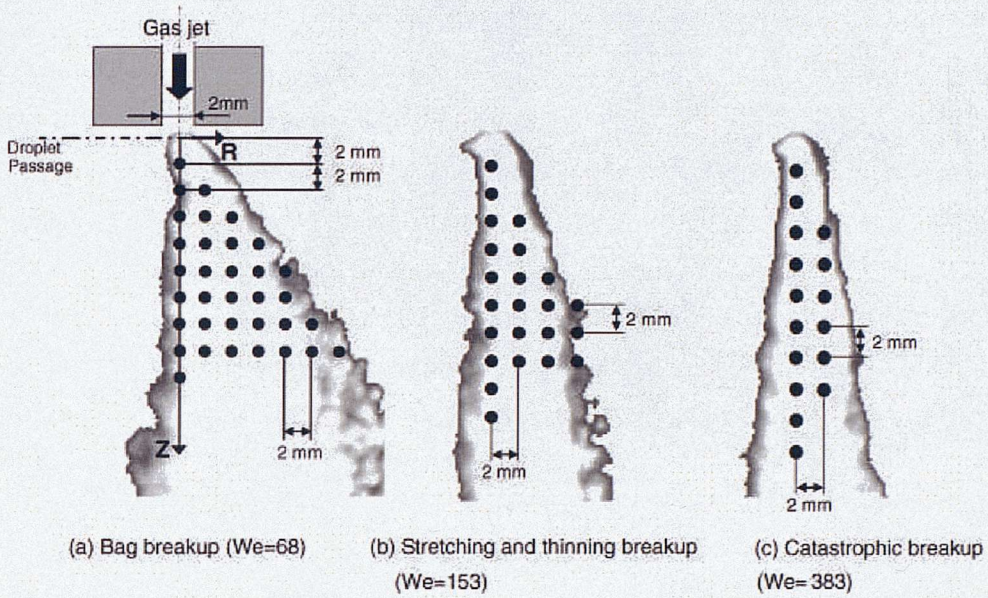


Figure 4.20: Measurement points of th PDA experiment according to th breakup regimes

Simulations are carried with two different grid. A first set of simulations is performed with a grid of approximatively 700000 nodes. A more refined grid of approximatively 2 millions elements is used in order to investigate the grid independence of the adopted model. The Weber number is an important parameter which indicates the potential of the droplet breakup. As the Weber number increases from the critical Weber, three different Breakup regime are investigated.

4.7.1 Air Jet

Before proceeding to the analysis of the two phase problem the particle-free flowfield is examined. Unfortunately, the measurements reported in the droplet breakup experiment [65], considered later for the validation of the model, are relative only to the liquid phase. No data is available for the continuous gas phase. However, an analysis of the jet has been performed considering the data from different experiments [13, 45, 72, 99], which give an overall clear picture of the features of the still jet. The case considered is an air jet at room temperature in

still air, the nozzle diameter is 2mm and the velocity for the gas phase is 100 m/s. Simulation with the Smagorinski constant Cs equal to 0.12, 0.135 and 0.16 were performed. Figure (4.21) shows the variation with axial distance of the mean velocity along centerline of the jet with the different Cs. It is possible to argue that the ratio between the distance and the number of cells in the present case does not allow one to notice any appreciable difference. The implementation of a dynamic calibration of the Smagorinsky model constant could lead to the best value of Cs for the test case adopted, but the few changes in the velocity profile with different constants suggest that there is no need to use such a computational expensive device. Another important issue highlighted by references is the effect of a turbulent inflow condition and a inflow velocity profile on the jet velocity fluctuations. However, even in this case no important difference is noticed in the behavior of the jet, even if initial perturbations are added to the inlet conditions. A value of Cs equal to 0.12 is adopted for the present test case .

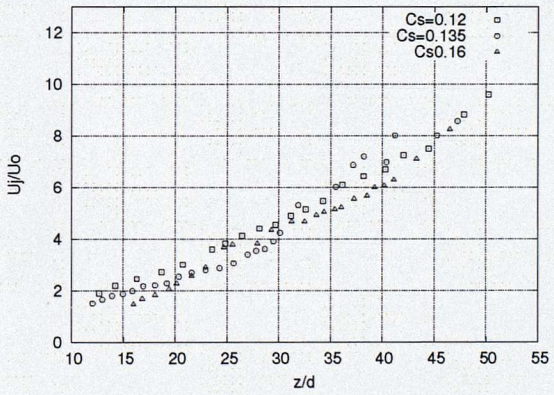


Figure 4.21: Variation with axial distance of the mean velocity along the centerline in the jet with different Cs

4.7.2 Bag breakup regime (We=68)

The first regime considered is the one with We=68. When the Weber number is slightly higher than the critical value, a thin hollow bag originates at the droplet stagnation point. The bag grows and bursts forming a number of small and big

fragments [51]. Some large fragments are able to cross the jet intact and experience further fragmentation in the quiescent flow area, where the Weber numbers are much smaller. In contrast small fragments with low momentum are captured by the jet and are transported by the turbulent eddy structure of the fast moving air jet. Figure (4.22) shows a comparison between the global experimental and simulated contours of SMD: the results of the simulations are in good agreement with the measurements. In the bottom right region, overprediction of the simulated SMD occurs if compared to the experimental values. However, it is possible that as this is an stagnant region, the wrong estimation is due to an accumulation of big droplets.

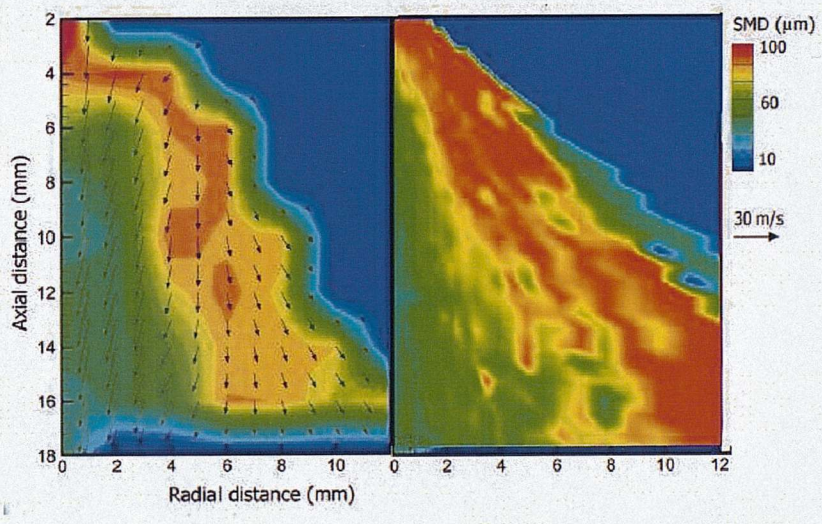


Figure 4.22: Sauter Mean Diameter of droplets: left experimental, right simulated

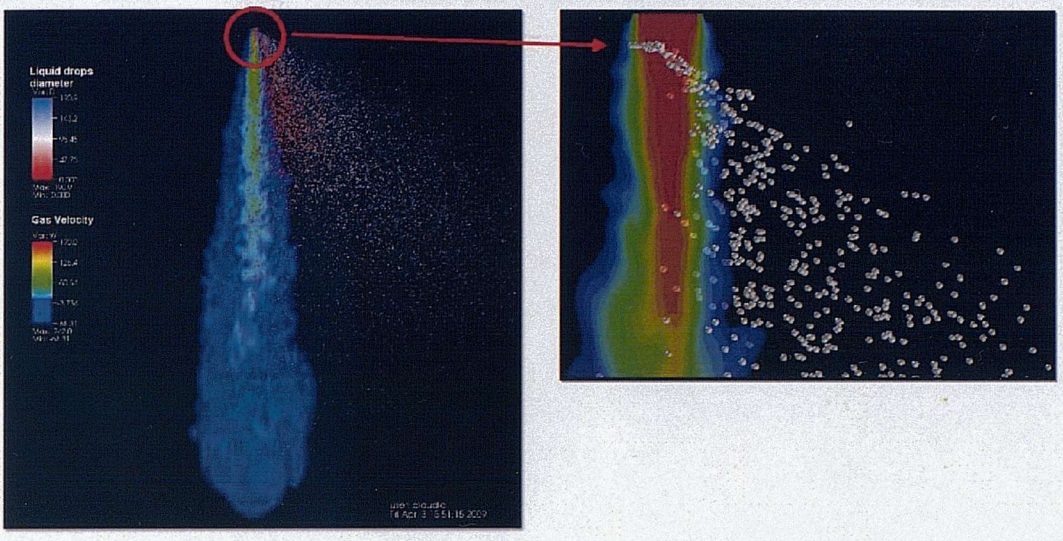


Figure 4.23: Breakup in cross flow

Figure (4.24) shows the general behavior of the experiment compared with the simulation where it is evident that the global physic of the system are well simulated.

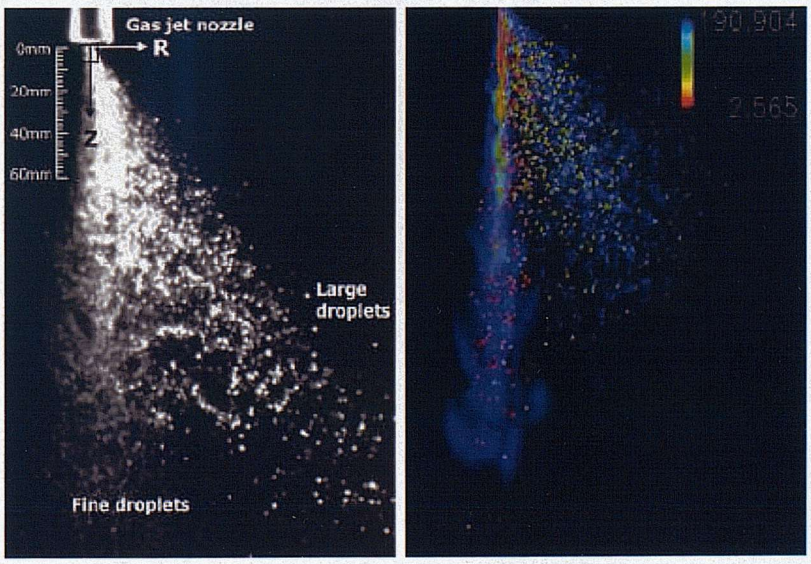


Figure 4.24: Sauter Mean Diameter of droplets: left experimental, right simulated

Small droplets(red) and large droplets (blue) have separate trajectories, accordingly with their momentum, as also reported by the experimental analysis.

The SMD profiles along the radial direction are compared with the experimental data at an axial distance of 8,12 and 16 mm from the centre of the reference frame. The results of the simulation and measurements are in good agreement: the simulated diameter is very close to the experimental findings with an error of $10 - 20\mu m$ at most.

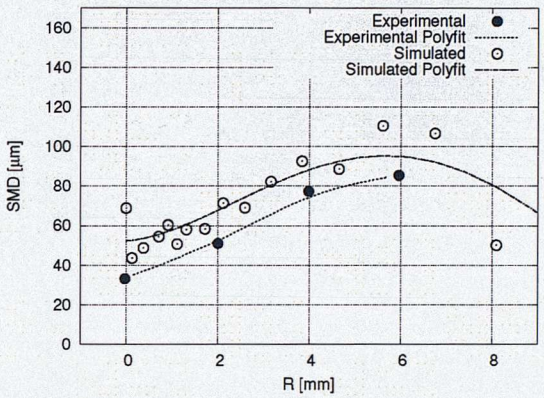


Figure 4.25: Size distribution according to radial distance at a distance of 8 mm from the jet nozzle. Distance in mm (x axis) SMD in μm (y axis)

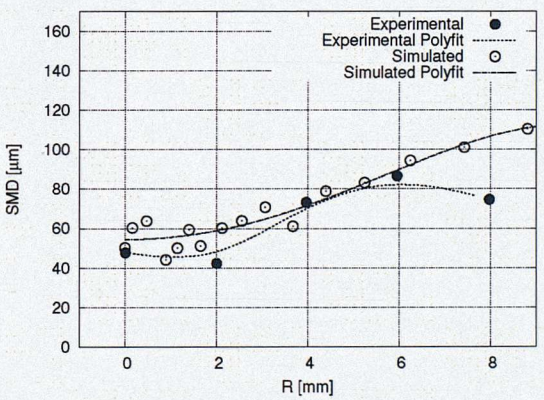


Figure 4.26: Size distribution according to radial distance at a distance of 12 mm from the jet nozzle. Distance in mm (x axis) SMD in μm (y axis)

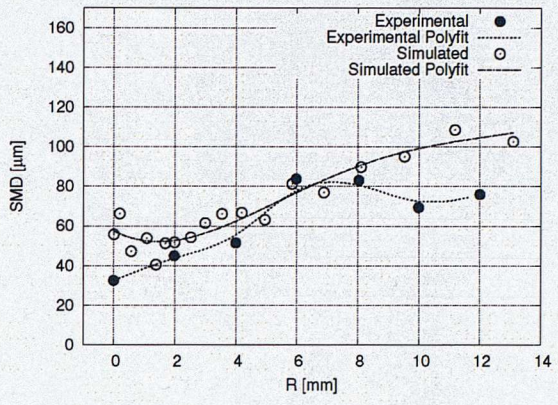


Figure 4.27: Size distribution according to radial distance at a distance of 16 mm from the jet nozzle. Distance in mm (x axis) SMD in μm (y axis)

The global behavior is well represented, and the simulations appear to reproduce with good accuracy the droplets sizes, with an error which is in the worse case of about 20-40 μm. In the 12 and 16 mm profile the predicted SMD is very well represented in the area close to centre line. The same overprediction discussed in the contour plot is visible in the far field and leads to the observed divergence of the simulated SMD from the experimental one.
The axial mean velocity of the droplets is also compared with experimental data at the same locations:

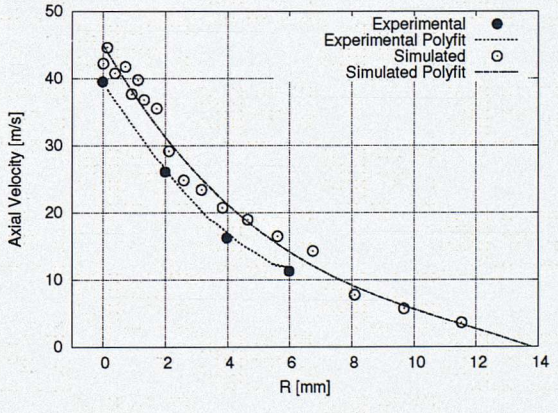


Figure 4.28: Droplet Mean Axial Velocity according to radial distance at a distance of 8 mm from the jet nozzle. Distance in mm (x axis) Velocity in m/s (y axis)

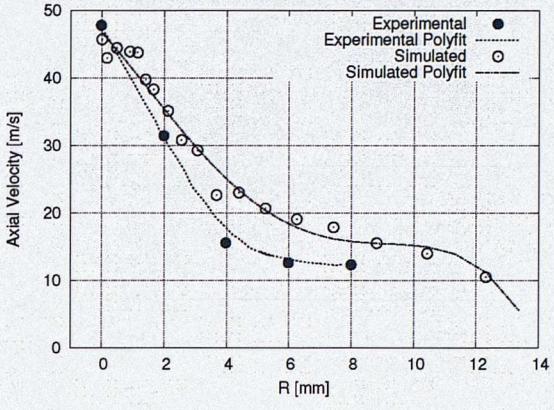


Figure 4.29: Droplet Mean Axial Velocity according to radial distance at a distance of 12 mm from the jet nozzle. Distance in mm (x axis) Velocity in m/s (y axis)

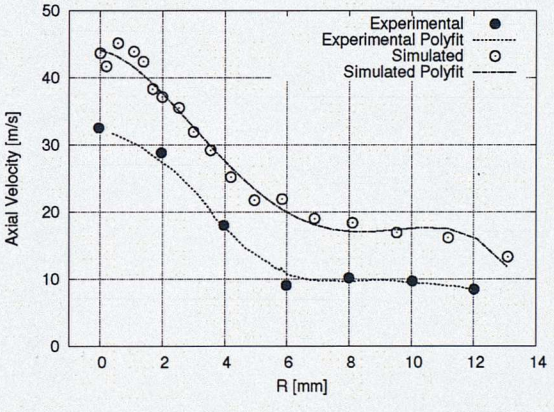
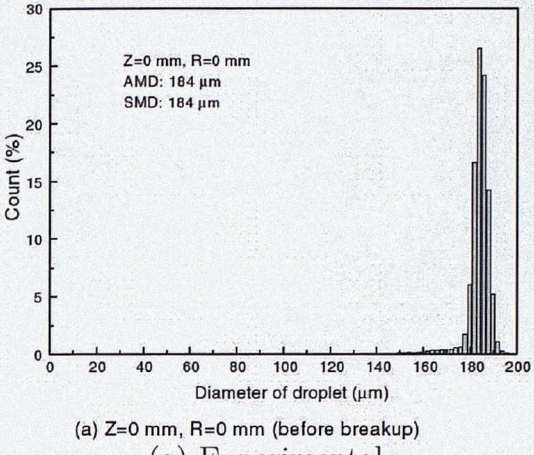
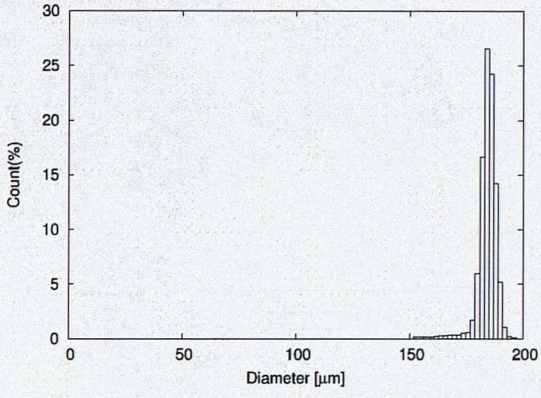


Figure 4.30: Droplet Mean Axial Velocity according to radial distance at a distance of 16 mm from the jet nozzle. Distance in mm (x axis) Velocity in m/s (y axis)

The results are found to yield good agreement with the experiment. A slight overprediction of the velocity along the axis of injection is observed, where the simulated small fragments appear to move faster than the experimental ones. The PDF of droplet diameter at the injection point (Z=0mm, R=0mm) and at two specific locations (Z=12mm, R=8mm) and (Z=4mm,R2mm) are considered below.

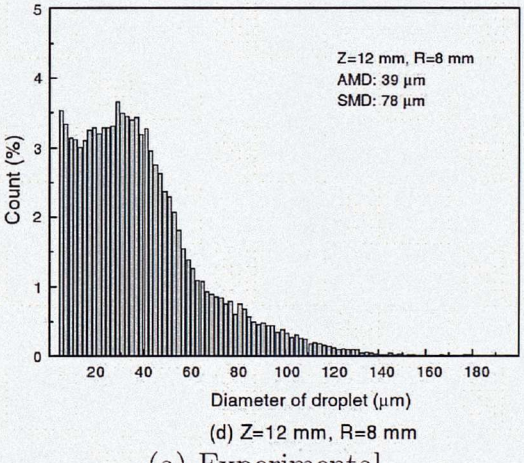


(a) Experimental

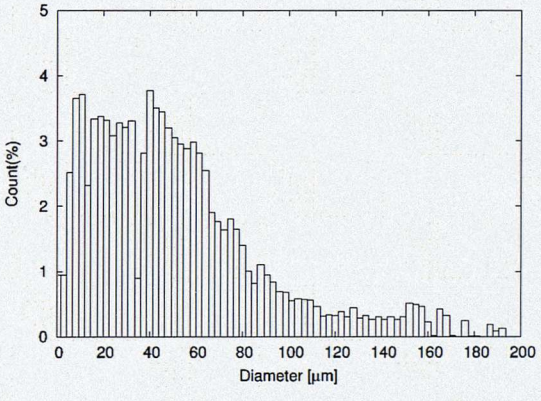


(b) Simulated

Figure 4.31: Probability density function of droplet diameter at injection

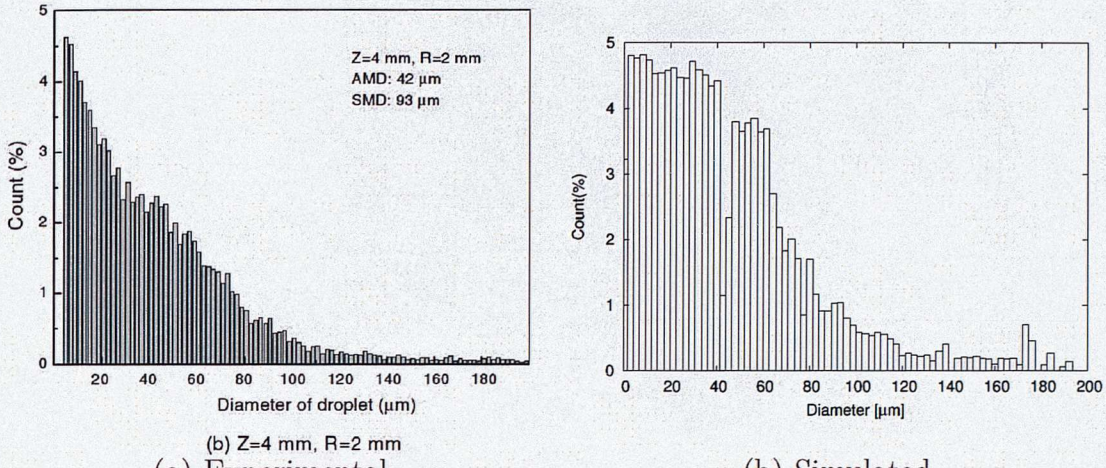


(a) Experimental



(b) Simulated

Figure 4.32: Probability density function of droplet diameter at $z = 12$ mm , $r = 8$ mm



(a) Experimental (b) Simulated

Figure 4.33: Probability density function of droplet diameter at $z = 4$ mm , $r = 2$ mm

The pdf in the injection point was imposed to be equal to the experimental one, while the registered profile in the second location shows that the model is capable of reproducing the physical behavior, even with some inaccuracy in the prediction of the number of big (greater than 80 μm) fragments. In contrast to the experiment the simulations indicate a finite but small probability of observing large droplets of diameter 180 μm, though in other respects the shape of the pdf appears to be well reproduced with an error that in the worse case scenario is about 10%.

4.7.3 Stretching and thinning breakup regime (We=153)

In the stretching and thinning breakup regime, droplets are observed to disintegrate [65] at their edge because of a suction stress toward the flow direction generated at the surface of the droplet. In this case, a shearing action due to the high-speed gas flow on the droplet causes the deformation and separation, leading to the formation of smaller fragments (compared to the previous regime). The simulated mean diameter and mean axial velocity along the axis of injection are investigated.

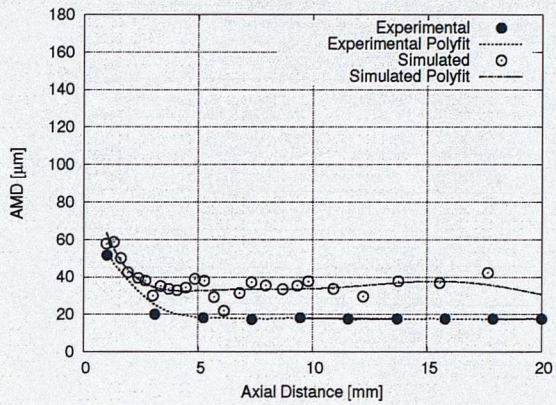


Figure 4.34: Mean Diameter according to axial distance (We=153). Distance in mm (x axis) AMD in μm (y axis)

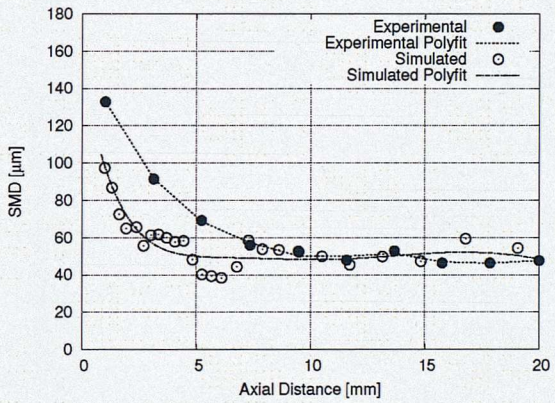


Figure 4.35: Mean Diameter according to axial distance (We=153). Distance in mm (x axis) SMD in μm (y axis)

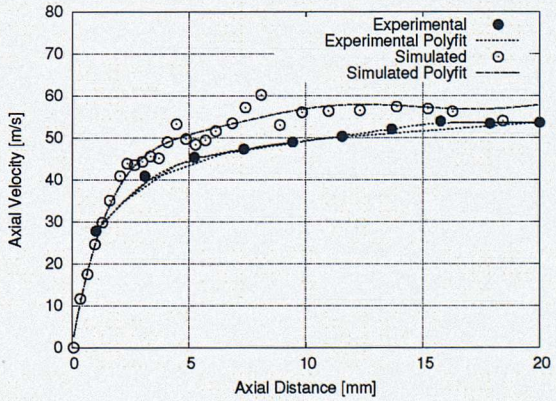


Figure 4.36: Droplet Mean Velocity according to axial distance (We=153). Distance in mm (x axis) Velocity in m/s (y axis)

The mean diameter appears to be well reproduced, while the velocity is over-predicted in the area immediately after the injection. However, the overall agreement is satisfactory.

4.7.4 Catastrophic breakup regime (We=383)

As the Weber further increases, the breakup regime transitions to the catastrophic breakup. The breakup of the droplet occurs suddenly due to the wave instability on the droplet surface. The diameter of the daughter droplets is smaller than in the previous regimes, as the droplets appears to disintegrate almost immediately generating a big number of very small fragments. Again the profiles of the mean diameter and the mean axial velocity are investigated along the axis of injection.

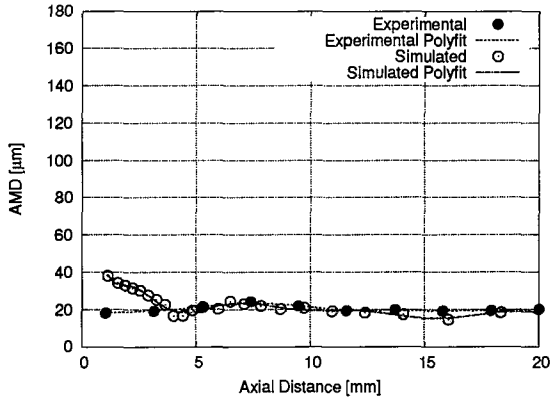


Figure 4.37: Mean Diameter according to axial distance (We=383). Distance in mm (x axis) AMD in μm (y axis)

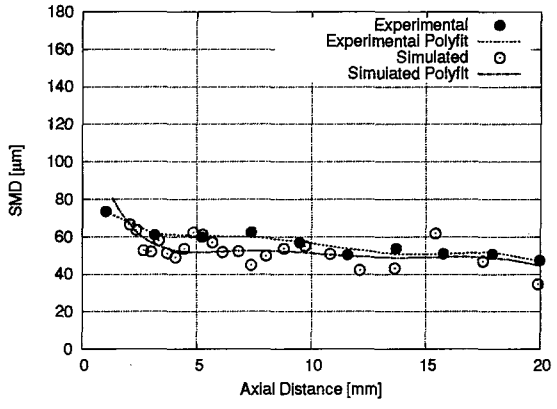


Figure 4.38: Mean Diameter according to axial distance (We=383). Distance in mm (x axis) AMD in μm (y axis)

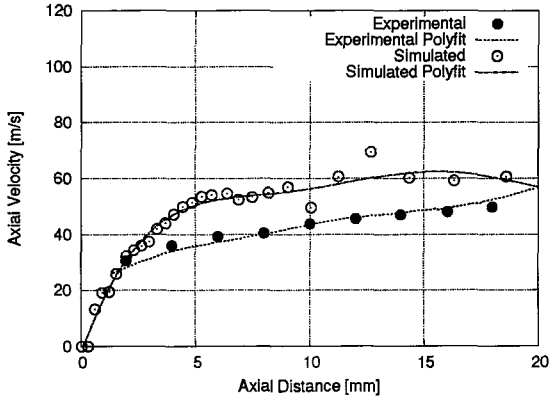


Figure 4.39: Droplet Mean Velocity according to axial distance (We=383). Distance in mm (x axis) Velocity in m/s (y axis)

The comparison of the predicted values with the experimental ones shows an underestimation of the mean diameter (about 10 μm) and a substantial overprediction of the mean velocity. However, the discrepancy between the simulated mean diameter and the experimental one is small and the results are acceptable.

Refined test case

Finally figures (4.40) - (4.45) show the results of the refined grid, suggesting grid independence of the model adopted.

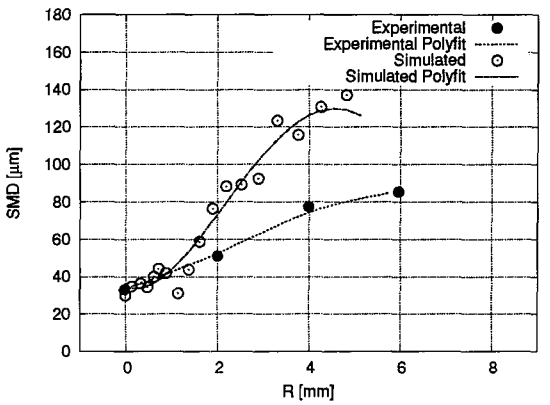


Figure 4.40: Size distribution according to radial distance at a distance of 8 mm from the jet nozzle. Distance in mm (x axis) SMD in μm (y axis)

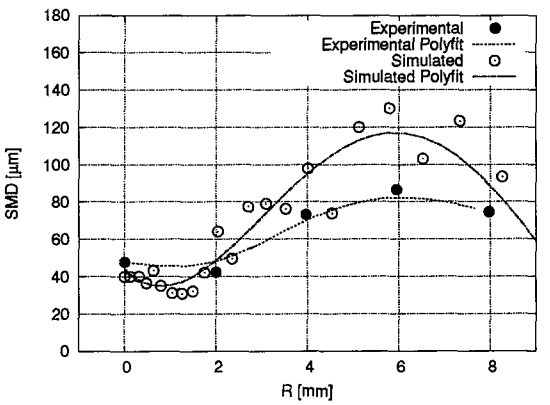


Figure 4.41: Size distribution according to radial distance at a distance of 12 mm from the jet nozzle. Distance in mm (x axis) SMD in μm (y axis)

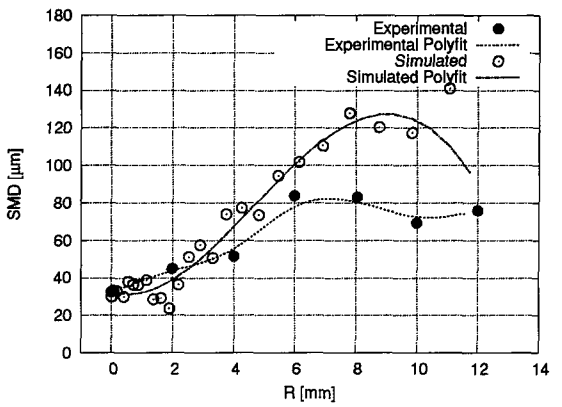


Figure 4.42: Size distribution according to radial distance at a distance of 16 mm from the jet nozzle. Distance in mm (x axis) SMD in μm (y axis)

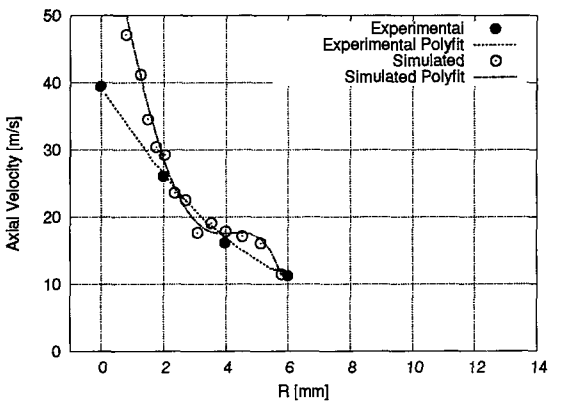


Figure 4.43: Droplet Mean Axial Velocity according to radial distance at a distance of 8 mm from the jet nozzle. Distance in mm (x axis) Velocity in m/s (y axis)

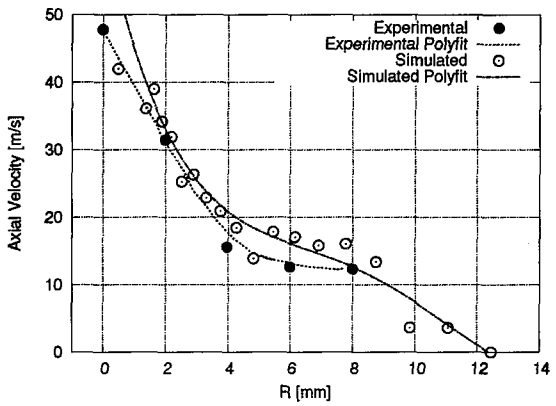


Figure 4.44: Droplet Mean Axial Velocity according to radial distance at a distance of 12 mm from the jet nozzle. Distance in mm (x axis) Velocity in m/s (y axis)

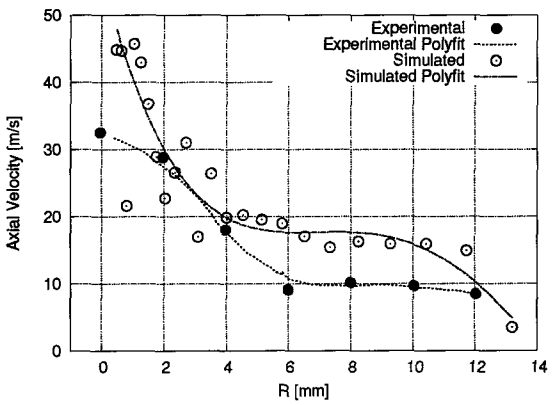
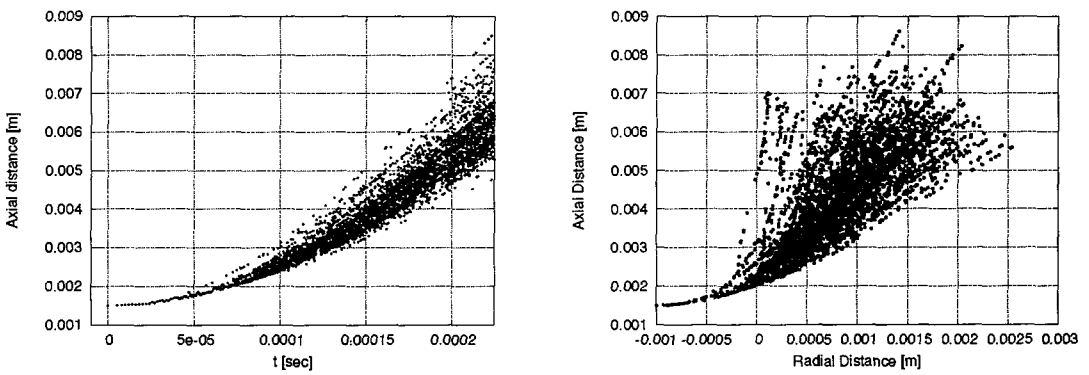


Figure 4.45: Droplet Mean Axial Velocity according to radial distance at a distance of 16 mm from the jet nozzle. Distance in mm (x axis) Velocity in m/s (y axis)

4.7.5 Evolution of the system of one single droplet

The Park et al [65] experiment represents a perfect test case for the study of the properties of the breakup of a single droplet. Liquid diesel mixture is injected into the gas in the form of single droplets, allowing one to follow the evolution of any monodispersed particle. The present analysis is made by injecting a single

droplets in the fully developed flow and collecting important data such as droplet position, velocity and breakup properties. The droplet is injected with a diameter of 184 μm, in the x direction, with a velocity of 13.4 m/s in a cross flow which corresponds to We=68, similarly to what was done in the first test case of the experiment [65]. Figure (4.46)a shows the droplets axial coordinate in time. Each point on the graph corresponds to a position occupied in time by a droplet. The initial particle travels in the flow and is deflected. Ramifications soon appear in the graph showing evidence of the generation of multiple fragments due to breakup. The tiny fragments have small mass and are deviated by the gas, while big fragments tend to keep a more straight trajectory. Figure(4.46)b shows the projection in a x-z plane of the location instantaneously occupied by the droplets. Also in this figure it is evident that the single droplet breaks into a constellation of fragments which are separated by the action of the air jet. The angle of deflection of the droplets is an important parameter which can be compared with the experimental data, showing the performance of the numerical simulation into predicting droplets dispersion and atomisation. The agreement appears to be good (see figure 4.22).

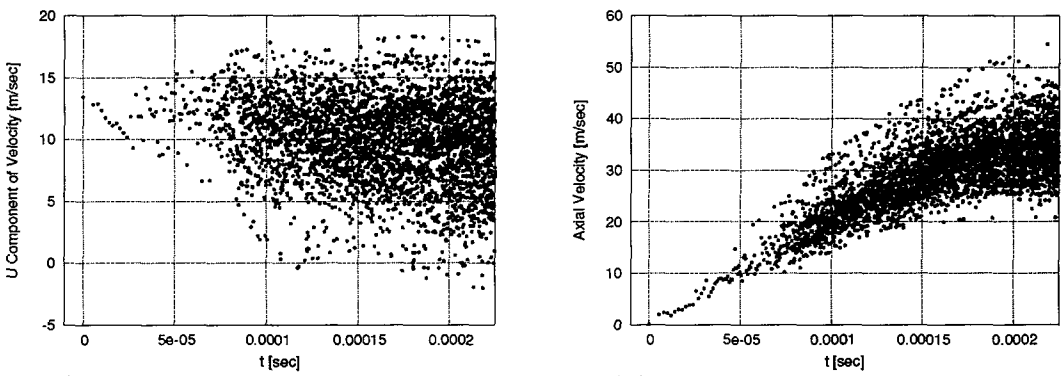


(a) Axial distance versus time (b) X-Z projection

Figure 4.46: Droplets characteristics from fragmentation of a single particle in the Park at al. experiment

Figures (4.47)a and (4.47)b show respectively the radial and axial velocity component of each droplets at different instants. The radial velocity is randomly distributed around the initial value of 13.4 m/s. The injected droplet undergoes acceleration in the radial direction due to the velocity fluctuation in the jet.

The axial velocity shows the acceleration of the initial droplet and its fragments as they are deviated by the jet. The newly formed fragments have different accelerations depending on their size. As most of the fragments have a size close to the mean value of 40 μm, the points are condensed around the medium axial velocity measure of about 40 m/s.

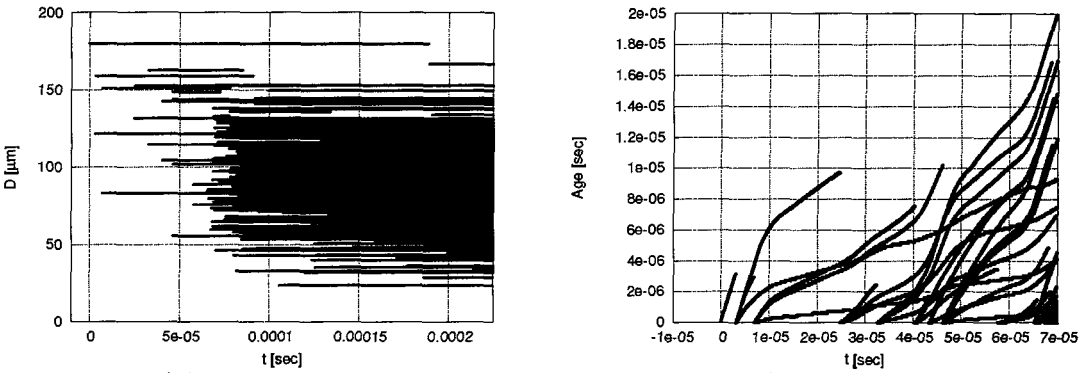


(a) Radial velocity versus time (b) Axial Velocity versus time

Figure 4.47: Droplets characteristics from fragmentation of a single particle in the Park et al experiment

In figure (4.48)a the diameter of the droplets is presented as a function of time. The first droplet of 184 μm splits under the influence of the external gas forces into fragments of smaller diameter. The creation of new droplets is clearly displayed by new diameters appearing in the graph. The diameter sizes are distributed around the mean value with some smaller or bigger droplets demonstrating that a constellation of droplets of different diameters is generated. During each breakup event, a new stochastic particle is generated and liquid mass is removed from the mother parcel in order to form new fragments. If the mother parcel has enough mass to supply the creation of the new fragments, the original stochastic particle continues to exist. However, at a certain point all the liquid is stripped from the mother parcel which will disappear. It can be noticed in the plot how the original droplet (the line at 180 μm) generates several fragments (other lines with different diameters) before exhausting all its mass and disappearing ($t = 1.8 \times 10^{-04}$ sec). In figure (4.48)b the age of the stochastic particle is plotted against the time. The age of a droplet is $\sum_t t_0 + dt$, where t_0 is the time of generation, breakup or injection of the particle. Each breakup occurrence is defined by the computation

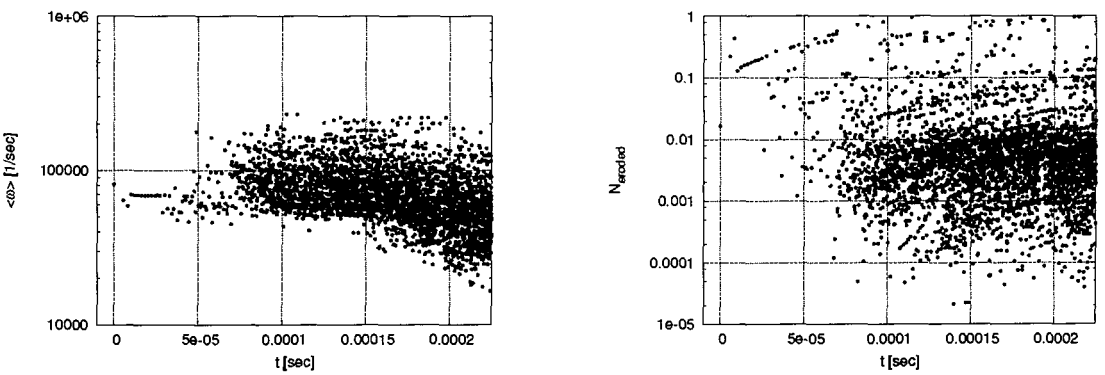
of an expected life of the droplet as explained in one of the previous sections. The expected life is compared with the actual age of the particle. When a droplet breaks new particles are generated and they start their life cycle. In the figure the generation of new droplets is clearly visible by the generation of new lines coming from the death of old ones.



(a) Diameter (b) Age

Figure 4.48: Droplet Diameters versus time (a) - Droplets age versus time (b)

Figure(4.49)a and (4.49)b show respectively the main rate of fragmentation and the number of droplets eroded at each step from the mother parcels. The first represent the average in time of the global breakup frequency which is used in order to calculate the expected life of the particle. The second is instead the probable fraction of the stochastic particle which would break each step. This number is summed and when the particle breaks n=n_{eroded} new droplets will form a new stochastic particle. The number goes from 0 to 1 where 1 denotes that the whole stochastic particle breaks.

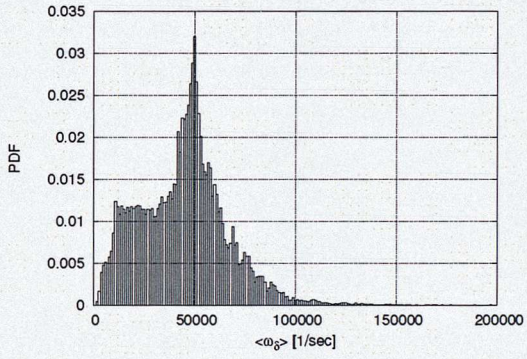


(a) Mean Rate of Fragmentation versus time (b) Number of erosion versus time

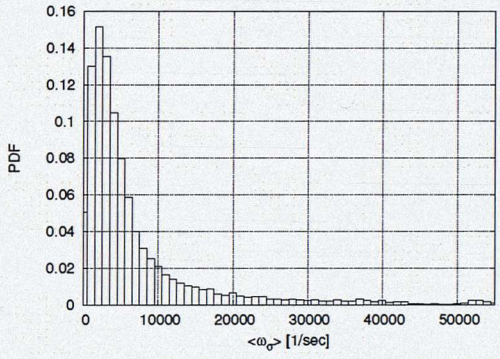
Figure 4.49: Droplets characteristics from fragmentation of a single particle in

the Park at al. experiment

Finally figure (4.50) shows the pdf among particles of the deterministic and sub-grid breakup frequencies. Initially the deterministic component is prominent, as it depends from the droplet relative velocity. Liquid diesel is injected in a fast cross flow and the relative velocity (which has a maximum of around 90 m/s) is the main reason for droplets to break. For this reason, in the bar chart the order of magnitude of the deterministic frequency is almost 10 times bigger than the stochastic contribution. It is evident that the role of the stochastic term becomes more important in the far field, when the droplet relative velocity decreases.



(a) Deterministic frequency



(b) Stochastic frequency

Figure 4.50: Droplets characteristics from fragmentation of a single particle in the Park Lee experiment

4.8 Conclusions

An LES probabilistic approach for droplet secondary breakup has been formulated and validated. Overall the formulation was found to yield good agreement with experimental data. The predicted droplet SMDs were compared with two test cases: a single cycle of diesel fuel injector issuing droplets into quiescent pressurised nitrogen and mono-dispersed droplets injected into a cross flow. In the former case the size of the droplets and the spray penetration show a reasonably good agreement with the measurements and compared with other breakup models proposed by different authors. The global behavior of the system is well captured,

and the droplets appear to break, generating a constellation of fragments with diameters in agreement with the measured data. For the case of droplets injected into a cross flow a range of Weber numbers are encountered. It is found that the model is able to generate droplet fragments with different sizes as well as reproducing the global features of the experiment. The simulations indicate that large droplets with high momentum cross the jet whilst small droplets do not. They are captured and transported by the turbulent eddying structures thus reproducing the observed SMD distribution. The simulation showed predicted SMDs in good local and general agreement with measurements. The analysis of different breakup regimes with different Weber numbers proved that the model is able to adapt to the different breakup mechanisms. As the relative velocity between the gas and the liquid phase increases, the Weber number increases and the droplets break up displaying completely different physical behaviours. Even though the implementation of an LES solver which treats droplets as point sources does not allow one to simulate the real physical mechanism of fragmentation, the statistical model appears to be able to reproduce the global behavior with good accuracy. By dynamically relating the breakup frequency, the pdf of daughter droplets, the critical diameter and the expected life of the particles to the local Weber number, the model has been demonstrated to be suitable for the simulation of more complex geometries and cases, such as swirling stabilized burners of typical aeronautical turbine configuration.

Chapter 5

Large Eddy Simulation of the two-phase flow in an experimental swirl-stabilized burner

5.1 Introduction

In the present chapter LES is applied to the simulation of two-phase flow in a practical application. The test case considered is the MERCATO experiment: the set-up is essentially an aeronautical-type swirl-stabilized spray burner, fuelled by liquid Kerosene. A database described in [49] containing measurements of the mean and rms of both gas and liquid phase is available and represents and ideal tool for the validation of the simulation method. Computations are performed using the in-house LES code Boffin, which was described in the previous chapters. Dispersion, evaporation and break-up of the droplets are considered with the models for the sub grid scale contributions being presented in chapters 2, 3 and 4.

The first part of the chapter introduces the MERCATO experiment by breifly

showing the features of the experimental set-up and presenting some informations about the optical measurements. In the second part the results of gas and liquid phases are compared to the experimental findings, demonstrating that the essential features of the flow are reproduced to a good accuracy.
Finally, a discussion of the results of the gas and liquid phases is presented, and it can be divided in two parts. In the first part the predicted statistics are compared with the experimental findings, commenting the quality of the results and discussing eventual differences. In a successive section the flowfield topology is discussed, with special emphasis on the interactions between the continuous and dispersed phases.

5.2 Configuration

The case considered is the MERCATO combustor, which is a test rig used by ONERA in order to investigate extinction and ignition phenomena in flight and in altitude conditions. The experimental set up resembles an aeronautical-type swirl stabilized spray burner. The following figures (5.1) and (5.2) show the MERCATO test bench:

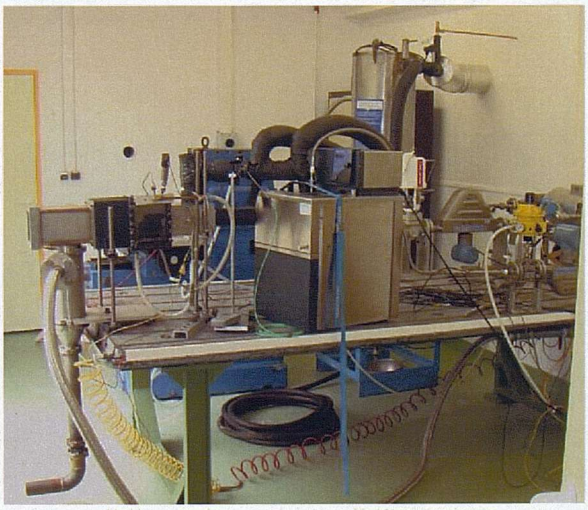
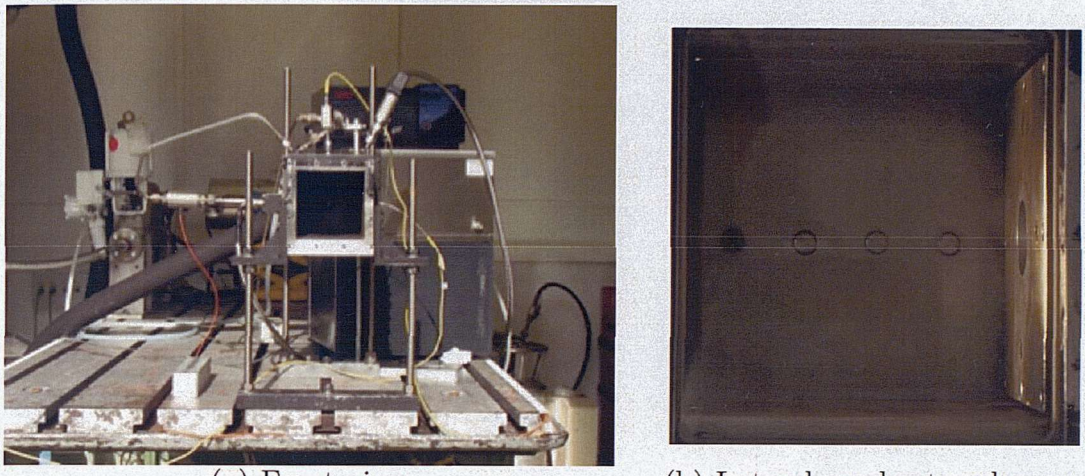


Figure 5.1: Lateral view of the MERCATO experimental rig



(a) Front view (b) Lateral combustor close-up

Figure 5.2: MERCATO Test bench - front view (a) - Combustor (b)

The rig consists of a square section plenum chamber, which contains the injection system. The plenum is connected to a test chamber which also has a square section. Optical access in the combustor is provided by a side window. Pre-heated air flows into the plenum, passes through the vanes of the swirler and flows into the combustion chamber. The test area has a square section 129 mm wide and 235 mm long. A schematic of the configuration is shown in figure (5.3).

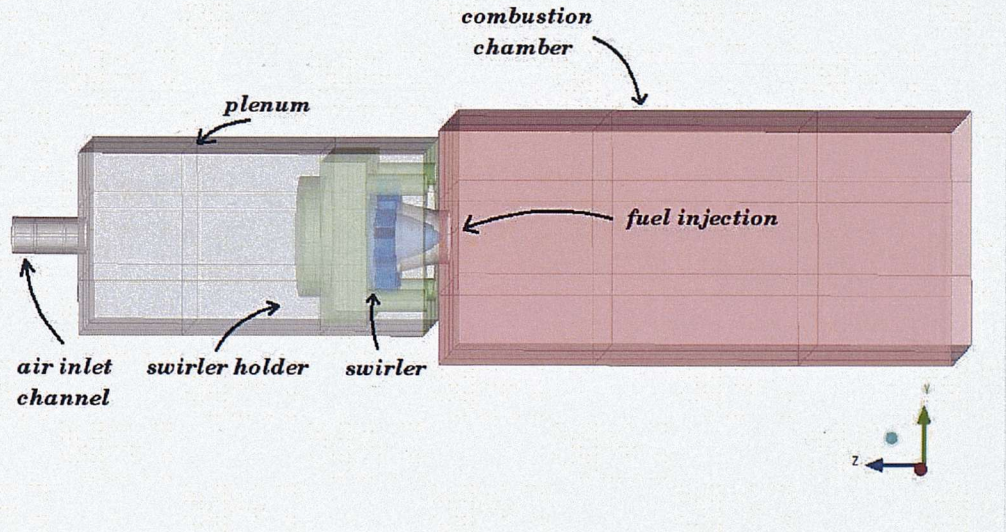


Figure 5.3: Sketch of the MERCATO test bench

Test case	WR ($Kg/sec\sqrt{K/bar}$)	$\dot{m}_a(g/s)$	$\dot{m}_f$ (g/s)	T(K)	P(MPa)
Case I low flow	0.142	6.6	0.45	463	0.1
Case I high flow	0.142	6.6	0.9	463	0.1
Case II low flow	0.284	13.2	0.6	463	0.1
Case II high flow	0.284	13.2	1.2	463	0.1
Case III low flow	0.426	19.8	1.0	463	0.1
Case III high flow	0.426	19.8	2.0	463	0.1
Ignition I	0.142	6.6	0.9	463	0.1
Ignition II	0.201	11.9	1.9	293	0.1

Table 5.1: Test cases

Optical access to the chamber section is available from the side window of the chamber which allows measurements to be made in a volume of dimensions: 129x129x129 mm^3. In the reacting case one lateral window is replaced by a plate holding the spark-plug. An additional square section 220 mm long is located behind the test chamber in order to be able to operate the combustor at pressures lower than atmospheric. The air ejector is perpendicular to the test chamber axis so that a window can be placed at the end of the interface part, allowing visibility of the injection face.

In the present work several regimes involving different mass flow rates are simulated, as reported by table (5.1). Each test case was carried out on the same geometry and differs from the others either by the air flow rate, the volume flux of injected Kerosene, or the gas temperature. All the experiments were performed at atmospheric pressure. The non-reacting test cases (Case I-III) have a temperature of 463K. In the non-reacting tests three different air mass rate conditions are investigated. For each of them, liquid Kerosene is injected at ambient temperature in two configurations; high and low mass flow rates of injected Kerosene. During the two reacting tests air is injected into the plenum at a temperature of 463K and 293K. Ignition is achieved by mean of a train of sparks located at different abscissae and along the combustion chamber. The spark abscissa and the Kerosene liquid mass rate are selected with considerations based on the results

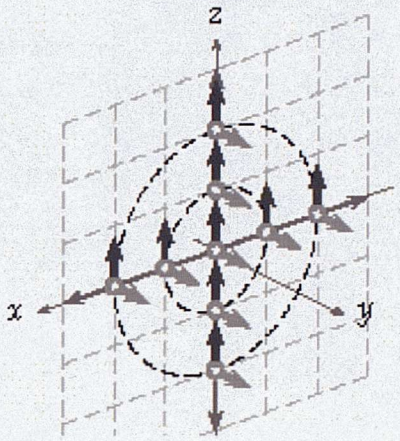


Figure 5.4: Definition of the axis and measured velocity components.

of the technical report provided by Onera [48]. The corresponding results for the ignition case are presented in chapter (6).
The experimental findings come in the form of Laser Doppler Anemometry (LDA) and Particle Dynamics Analysis (PDA) measurements contained in a data base, [49], [48] which is used in order to validate simulated data. The database includes the mean and the rms measurements of the gas phase velocity, the mean and the rms of the liquid droplets velocity, the volume fluxes and various diameter size measurements. LDA measurement of the gas phase are considered first. Velocity means and rms measurements are taken from a side windows and along perpendicular directions at different locations along the axis of the combustor. Figure (5.4) shows the definition of the axis and measured velocity components along two perpendicular axes.

Measurement are taken at a distance of 2mm from each other along perpendicular directions to the chamber axis and include two velocity components. The axial velocity component is measured in each location. Depending on the axis orientation either the radial or tangential velocity is measured. It is presumed that the flow is axial-symmetric. The gaseous phase measurement axes are located at 8, 26, 56, 86, 116 mm from the entrance of the combustor. PDA measurement are taken in a similar way, but with the slight difference that the first location

is at 6mm from the entrance of the combustor, rather than 8mm. Figure (5.5) shows the measurement planes:

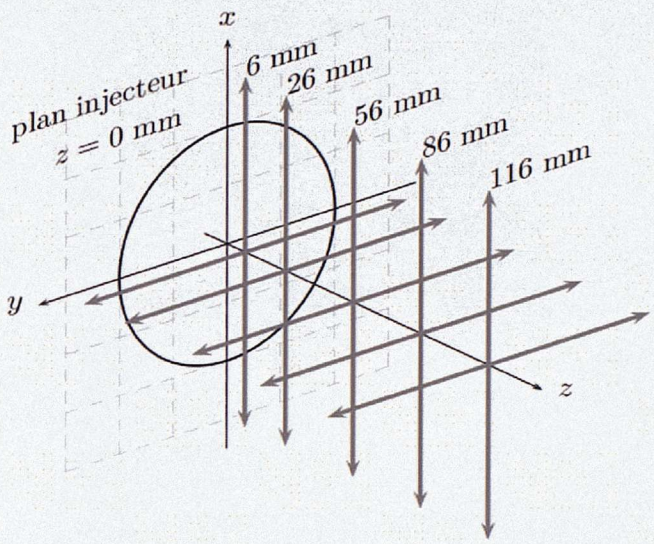


Figure 5.5: Measurement planes

Unfortunately, liquid phase measurement were only taken in the first one or two locations. This is because of kerosene accumulation on the windows which did not allowed the experimentalists to perform measurements in most of the sections. In particular, liquid measurements are available in the 6 and 26 mm sections for the low Kerosene flowrate case, and only in the 6 mm section for the high flow regimes.

5.3 Meshing

All the computations are performed on a fully structured multi-block mesh. A number of simulation were performed on several meshes, which differs for the domain extension and the number of elements. Table (5.2) is a summary of the adopted girds.

Initially, simulations are performed on a block structured grid of 3.7 millions cells which extents from the inlet of the plenum up to the exit of the combustor. The

Mesh	Number of Nodes	Number of domains
Complete	3.5 M	190
Coarse Partial Grid	1.0 M	34
First Partial Refinement	2.5 M	91
Second Partial Refinement	3.7 M	181

Table 5.2: Multi-block Meshes

air flow rate is computed from the mass flow rate given for the experiments [49] and the area of the section of the inlet of the plenum. Figure (5.6) shows the velocity vectors for the simulation of the complete geometry.

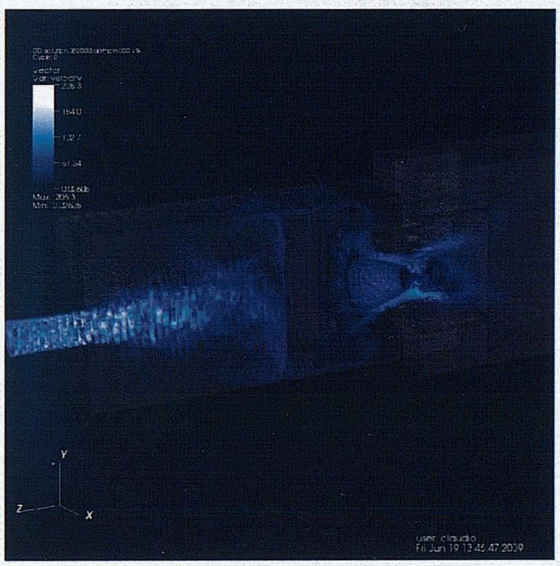
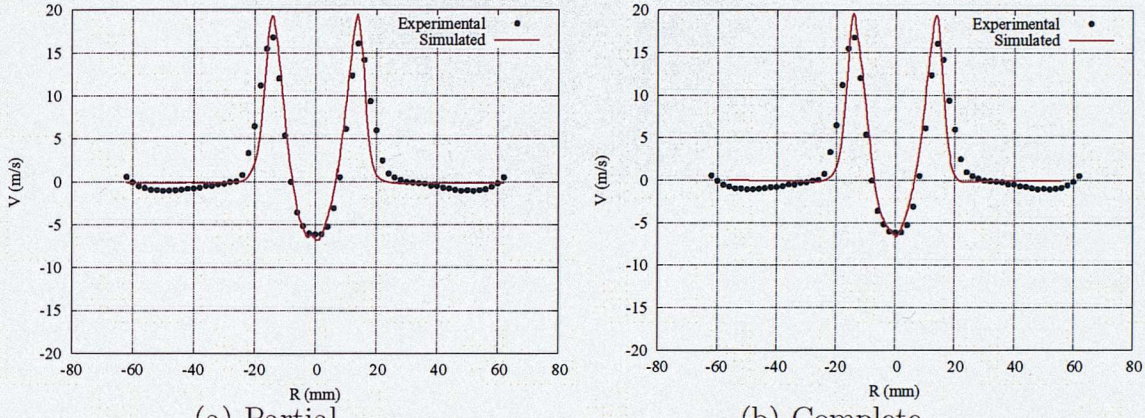


Figure 5.6: Velocity Vectors. Complete Grid

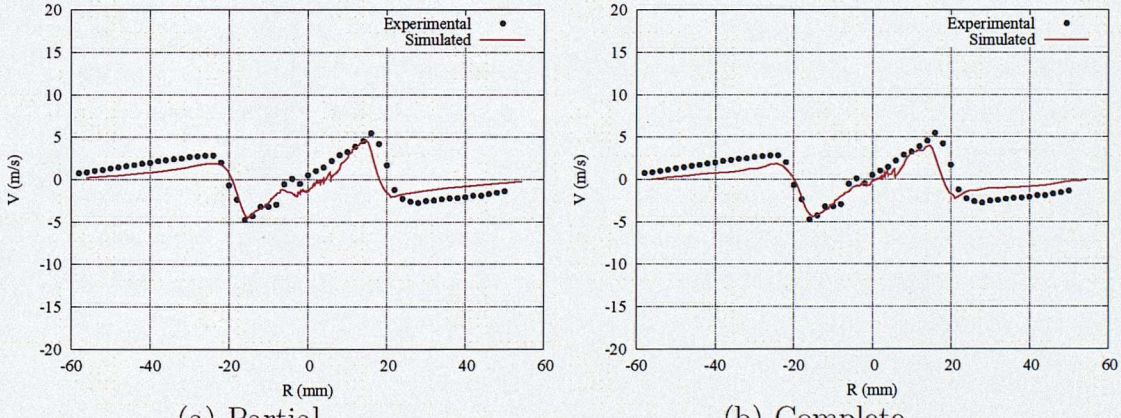
Air flows from the circular section of the injection system into the square plenum at a velocity of 27.6, 55.2 and 82.7 m/s respectively for the three mass flow rates : $WR = 0.142$, $WR = 0.284$ and $WR = 0.426$ $Kg/sec\sqrt{K/bar}$. The flow immediately slows down on entering the large squared section diffusing into a jet like structure. When the flows arrives at the liquid injector holder the velocity of the flow has dropped to an average value of 4.56, 9.12 and 13.7 m/s respectively. Further simulations demonstrated the flow in the plenum chamber

and the exhaust pipe could be omitted from the computations, since they had no appreciable effect on the flow field in the combustion chamber. Evidence of this can be found in the prfiles shown in figures (5.7) - (5.9) , which show the mean axial, tangential and radial velocity profiles at 8 mm for the two cases: the dots represent the experimental data, the lines are the simulated results.



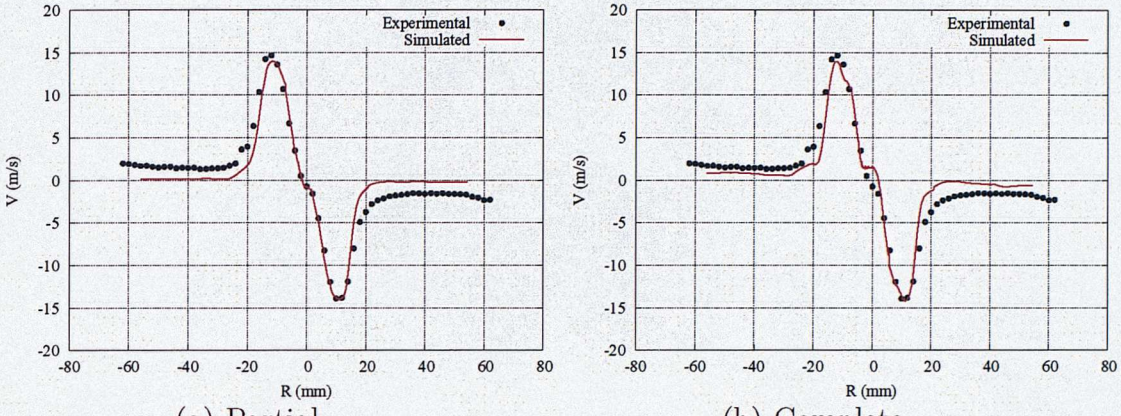
(a) Partial (b) Complete

Figure 5.7: Mean axial velocity profiles for the partial and complete grid



(a) Partial (b) Complete

Figure 5.8: Mean tangential velocity profiles for the partial and complete grid



(a) Partial (b) Complete

Figure 5.9: Mean radial velocity profiles for the partial and complete grid

The profiles of the complete and partial geometry show little if no difference, and both the computations yield good agreement with the experimental data. Neglecting the initial part of the geometry could help lower significantly the computational cost.

The partial solution domain extends from the entrance of the swirler to the exit of the combustion chamber. The cell size varies in the domain, with the most refined elements in the area close to the injector and with dimensions of the order of 200 μm for the refined mesh case. Local refinements are present on the wall of the vanes, in the swirler, close to the walls in the combustion chamber and on the tip of the injector. Figures (5.10)-(5.12) show the partial geometry mesh.

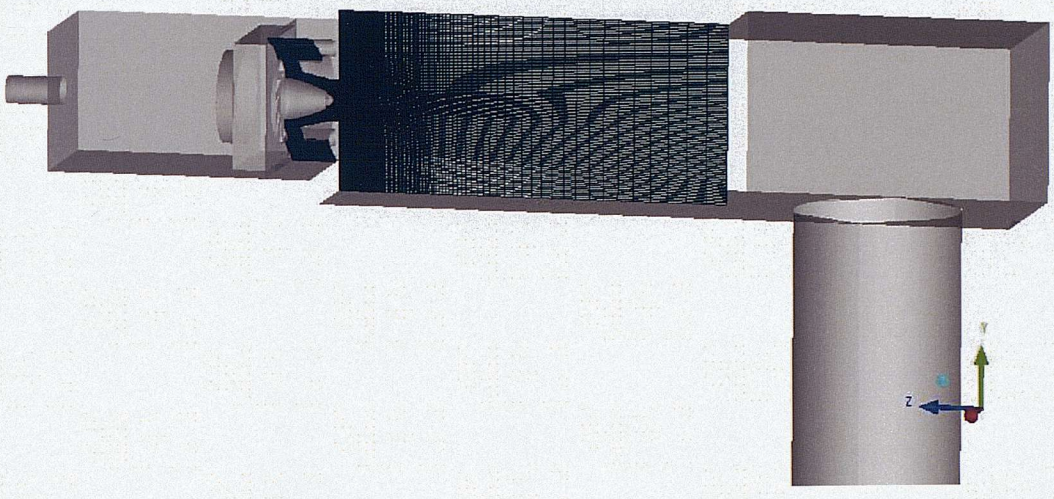


Figure 5.10: Partial geometry grid

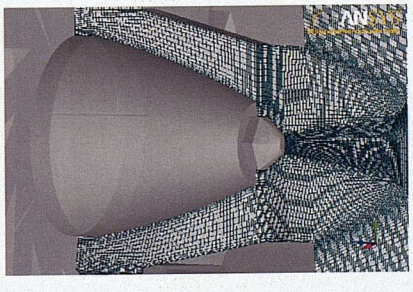


Figure 5.11: Injector area close-up

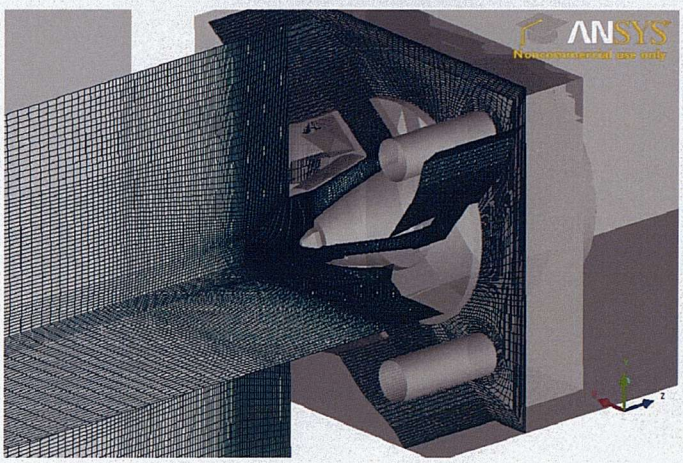
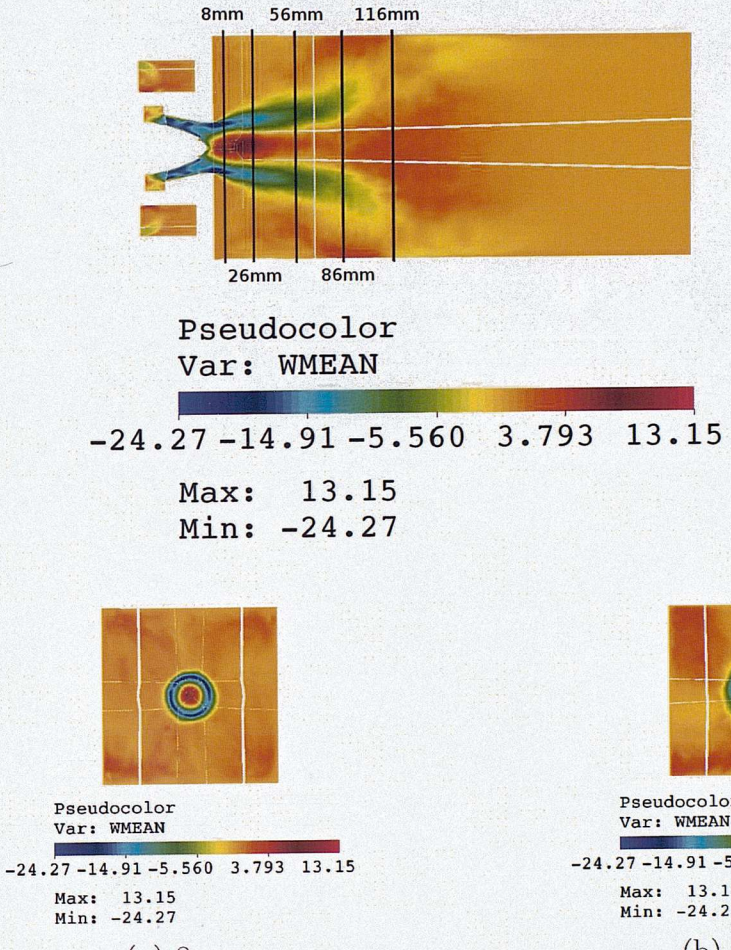


Figure 5.12: Planar sections

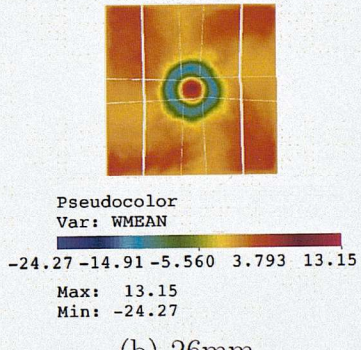
The injector tip has an hexagonal base with an angle of 17.3 degrees to the x-direction (the axes are oriented as shown in the figure). On one side, the injector base is connected to the circular section of the injection which ends in the 12 vanes of the swirler. On the other side the injector tip changes into a semi-conical shape and is linked with a cylindrical connector to the combustion chamber of square section. Local refinements and domain splitting at the injector tips and in the injector-combustor connection are necessary in order to apply a structured mesh to the geometry. Moreover, because the grid structure propagates from the injector tip to the vanes of the swirler, the same number of cells used on each side of the hexagonal injector tip must be equal to the number of cells in two of the vanes of the swirler. This led to further refinements in the injector area. However, this refinement does not have a negative effect on the computational cost of the simulation. Because of the Lagrangian particle methodology applied, the computational load depends both on the number of cells and the particle concentration of each domain. Splitting the injector area in domains with an equal number of cells increases the number of domains in this region where the particle concentration is relatively high.

5.4 Gas Phase

An evaluation of the ability of the LES formulation to reproduce the velocity field characteristics of the continuous gas phase is undertaken first. Clearly an accurate representation of the carrier gas flow is necessary if the properties of the dispersed phase are to be reproduced successfully. The mean axial, radial and tangential velocities of the flow field, as well as the *rms* profiles are compared with the experimental data. Air at a temperature of 463 K and a well defined flow rate and density is injected into the plenum and acquires a swirling motion as it passes through the vanes of the swirler. The geometry of the swirler exerts a dominant influence on the flow field downstream of it. The z-axis chosen in the experiment is oriented in direction opposite to the flow field so that the velocities are negative when the flow is towards the outlet. Figures (5.13)-(5.25) show the comparison of the mean and rms of the velocity profiles for the test Case I. Figure (5.13) shows the contour plot of the mean axial velocity in a plane perpendicular to the y direction, and in two planes perpendicular to the combustor axis at 8mm and 26mm locations. The axial component appears to be well reproduced (figure (5.14)) in the sections at 8, 26 and 56 mm. There appears to be a slight overestimation of the maximum in the far field at 86 and 116mm. All the simulated axial profiles reproduce to a good accuracy the measured data: the location of the maximum and minimum values as well as the global shape of the profiles are well reproduced. Finally, figure (5.15) shows an instantaneous snapshot of the axial velocity in a plane perpendicular to the y direction for y=0 and in two sections perpendicular to the axis of the combustor at 8 and 26 mm. The contour shows clearly the shear layer of the swirler and the various recirculation regions, which are discussed in the following section about the flow topology.



(a) 8mm



(b) 26mm

Figure 5.13: Mean Axial velocity. Top: Lateral view. 8mm Front section (a) - 26mm Front section (b)

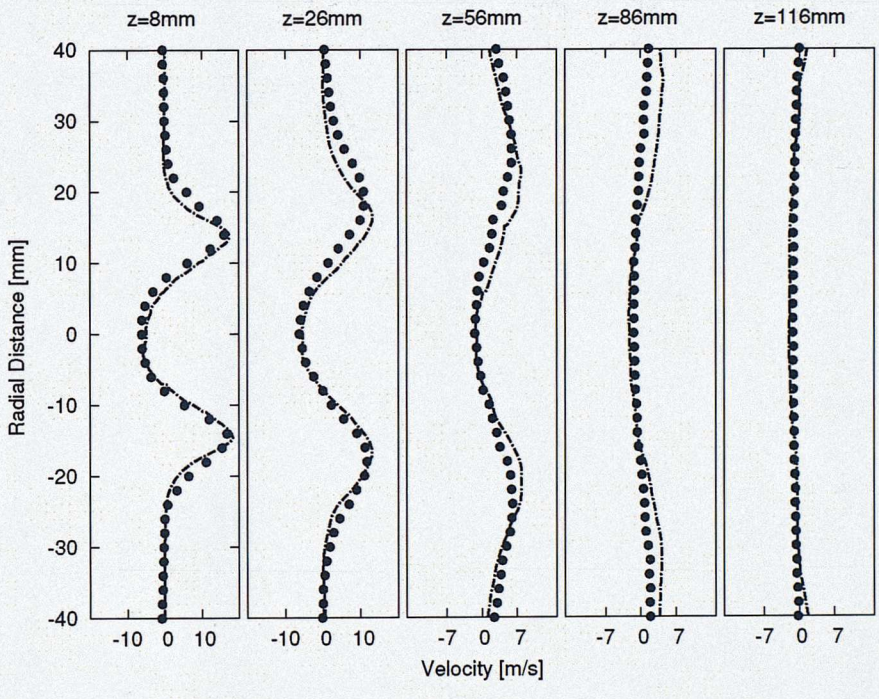
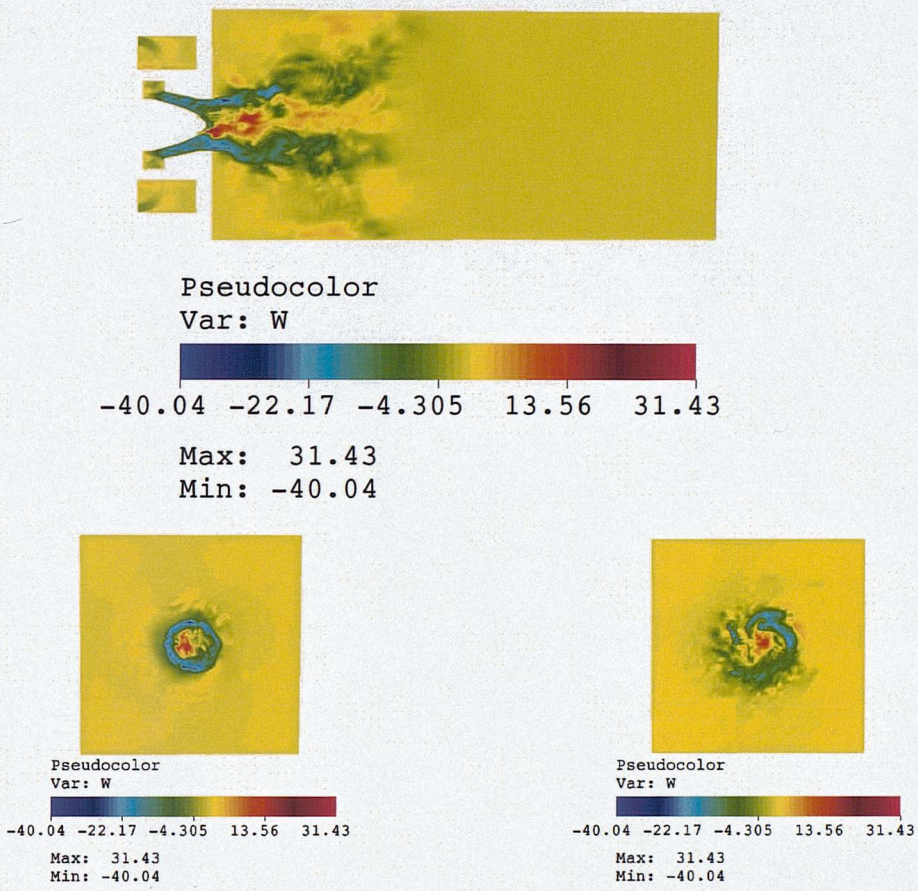


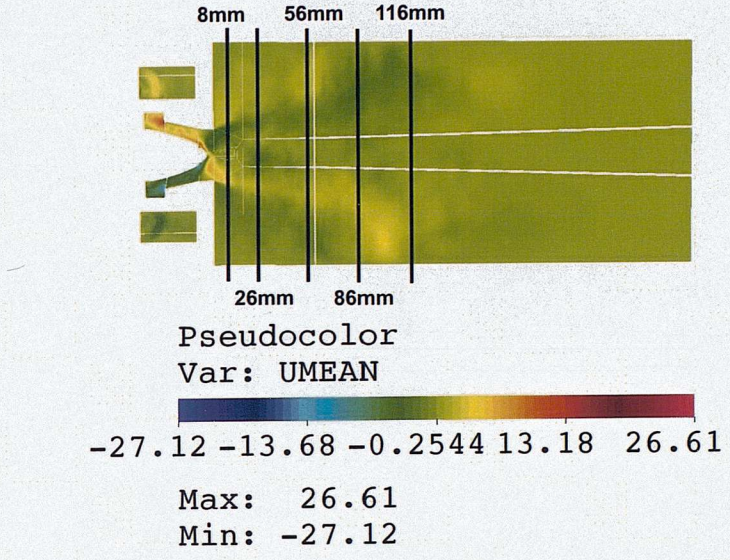
Figure 5.14: Mean Axial velocity

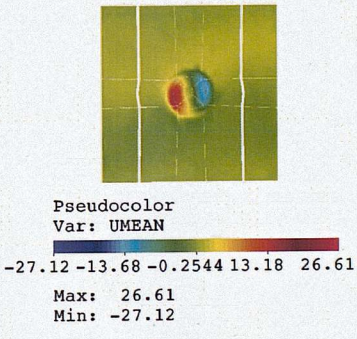


(a) 8mm (b) 26mm

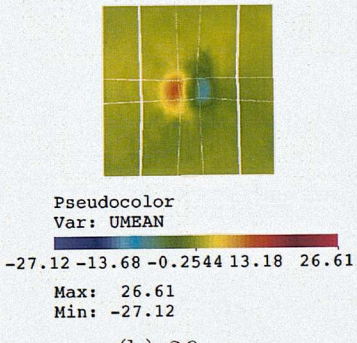
Figure 5.15: Instantaneous snapshot of the axial velocity. Top: Lateral view. 8mm Front section (a) - 26mm Front section (b)

The contour of the mean tangential velocity is displayed in figure (5.16). The comparison with experimental results in figure (5.17) show that the tangential component is well represented. The simulated profiles at each location follow those reported by the experiments with good agreement. The contour of the instantaneous tangential velocity component are also reported in figure (5.18).





(a) 8mm



(b) 26mm

Figure 5.16: Mean Tangential velocity. Top: Lateral view. 8mm Front section (a) - 26mm Front section (b)

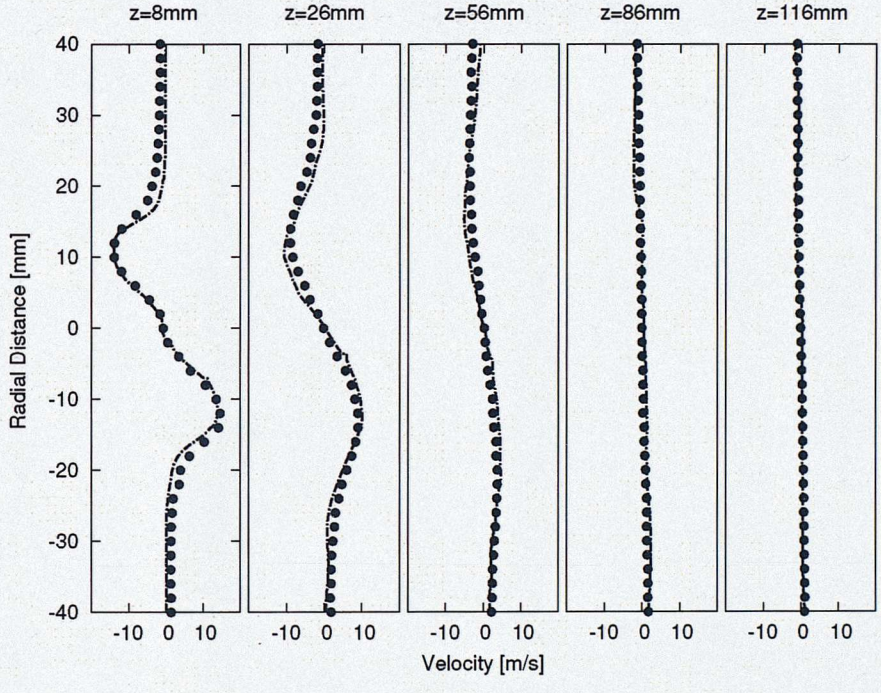
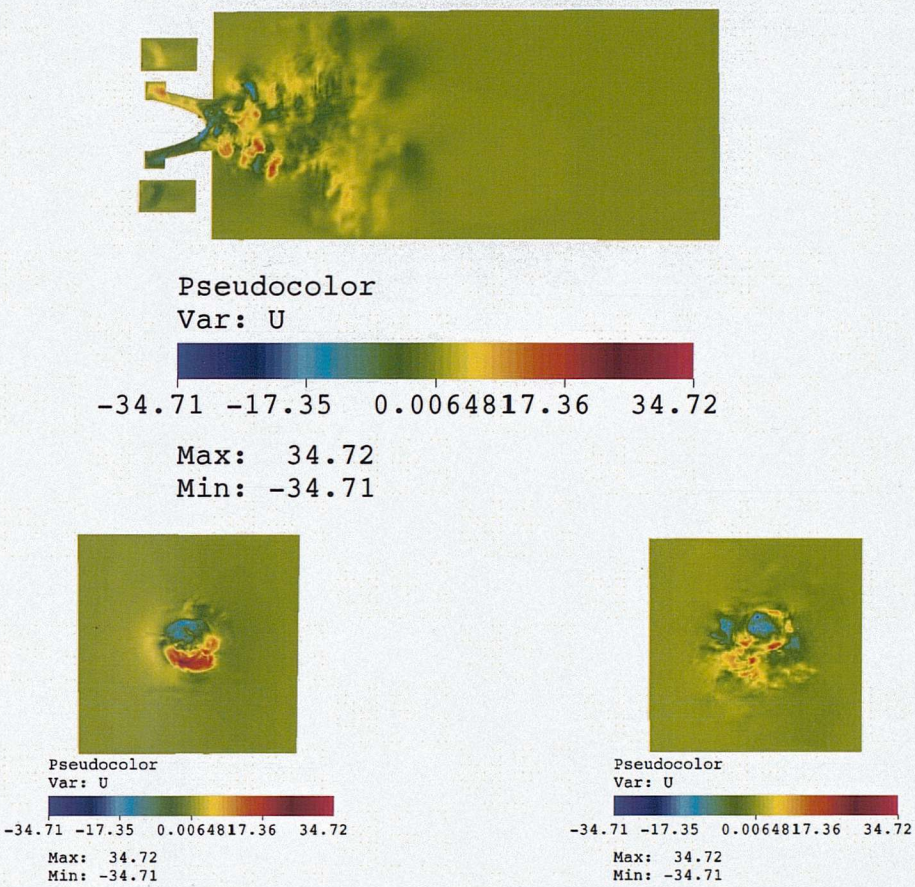


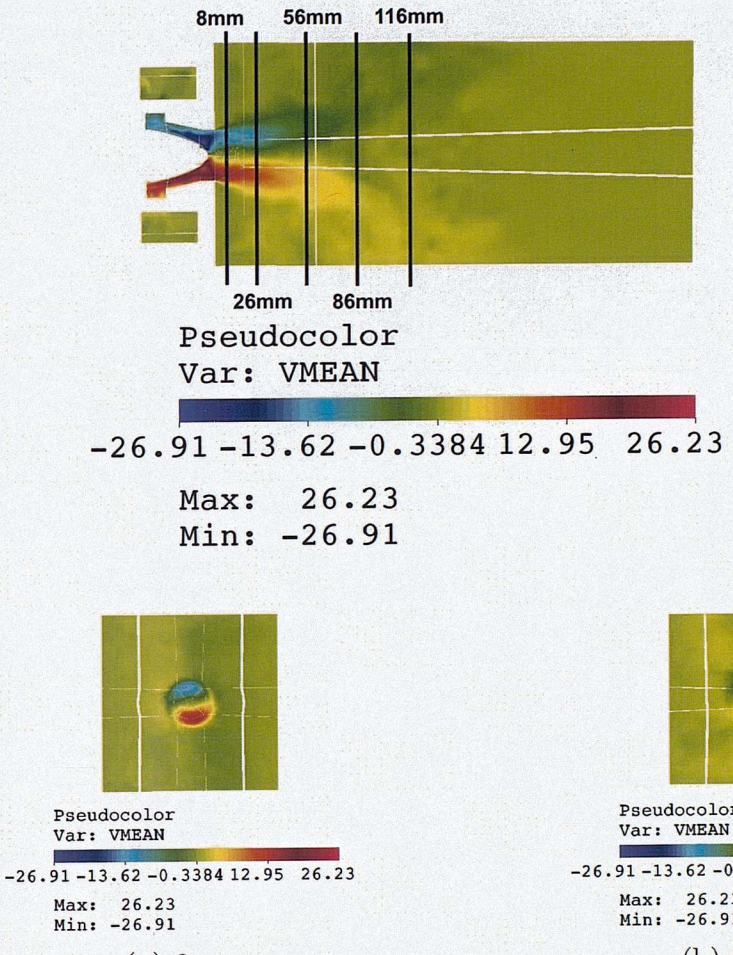
Figure 5.17: Mean Tangential Velocity



(a) 8mm (b) 26mm

Figure 5.18: Instantaneous Tangential Velocity. Top: Lateral view. 8mm Front section (a) - Air Mixture Fraction 26mm Front section (b)

The radial component profiles of figure (5.20) show a slight underestimation of the maximum velocity in the 26mm section which also effects the section at 56mm. A small overextimation of the predicted values is also observed in the same section. In both the cases the error is small and within the experimental uncertainty. Again, the global trend is well captured showing that LES is capable of reproducing the physics of the system.



(a) 8mm (b) 26mm

Figure 5.19: Mean Radial velocity. Top: Lateral view. 8mm Front section (a) - 26mm Front section (b)

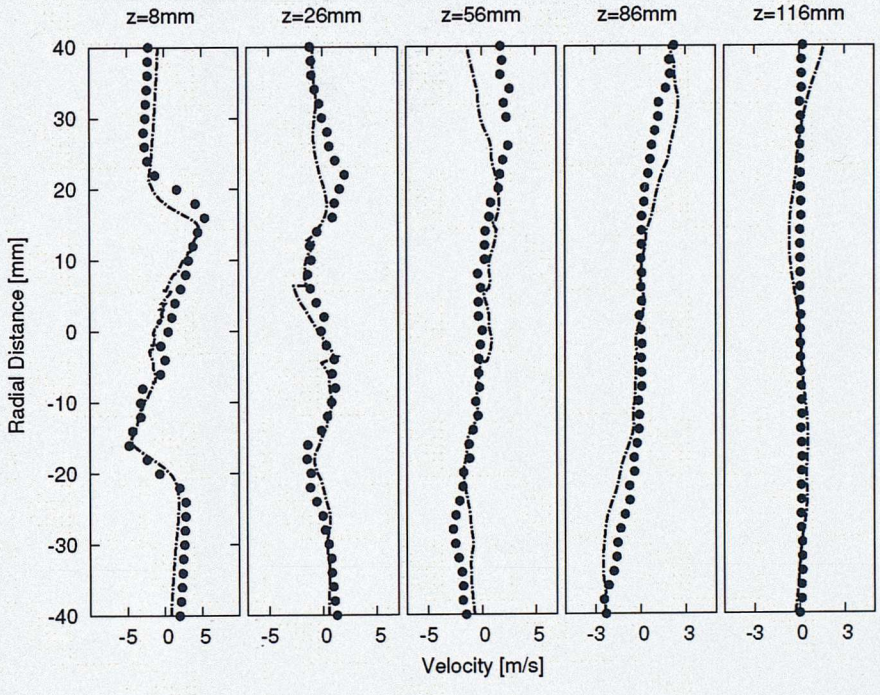
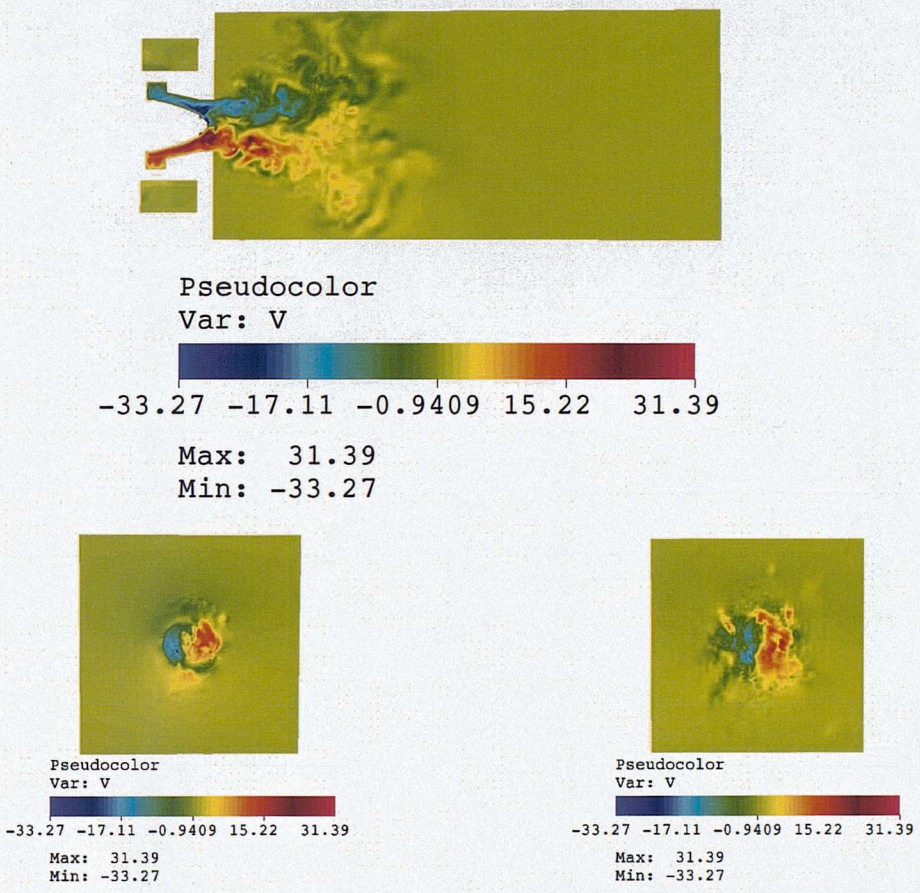


Figure 5.20: Mean Radial Velocity



(a) 8mm (b) 26mm

Figure 5.21: Instantaneous Radial Velocity. Top: Lateral view. 8mm Front section (a) - 26mm Front section (b)

The rms of all three components of velocities are compared in figures (5.22)-(5.24). The axial rms velocity shows an offset of the computed values in respect to the experiments at 8 and 26 mm. The maximum simulated value is in accordance with the observations, but its radial distance from the centerline is 2mm larger. The values at 56, 86 and 116 mm are in good agreement, with a slightly underestimation of the value in the center of the section at 56mm distance, and a slightly offset of one of the peaks in the same location. The overall agreement is

good and the rms of the simulated values is within $2m/s$ from the experimental data . The profiles of rms tangential velocity, figure(5.23) show an overestimation of the two maximum values in the 8 and 26 mm, 56 mm sections. However, the simulated values differs from the measurements for no more than $1m/s$. Finally the profiles of the rms of the radial component, figure(5.24) yield good agreement in all the sections.

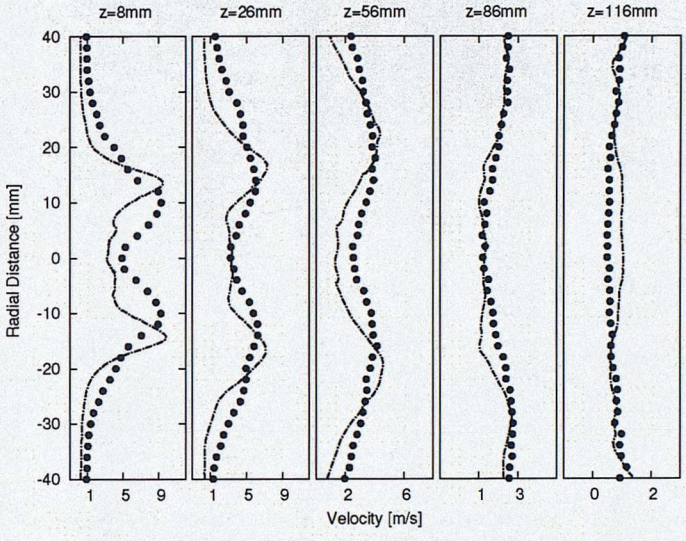


Figure 5.22: *Rms* of Axial Velocity

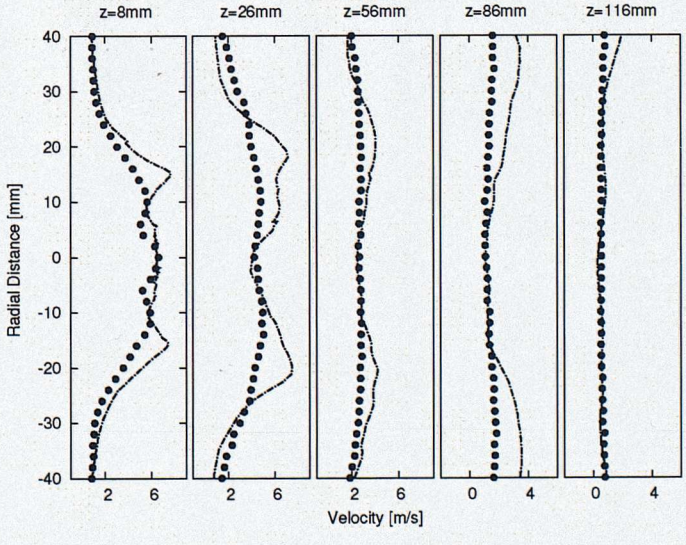


Figure 5.23: *Rms* of Tangential Velocity

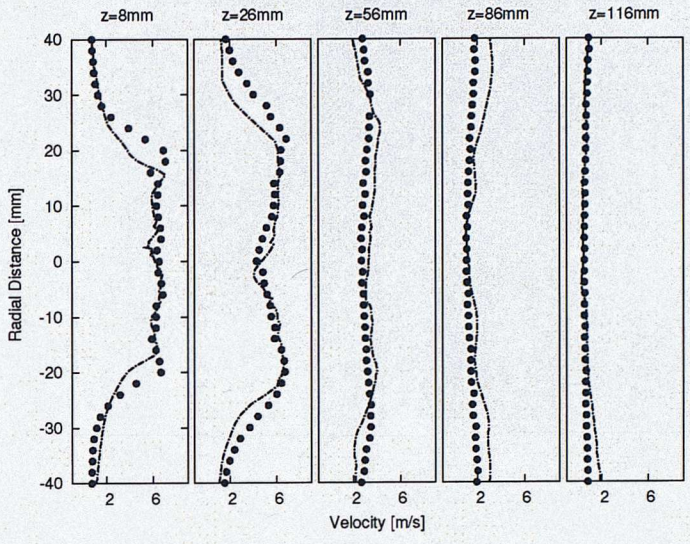


Figure 5.24: *Rms* of Radial Velocity

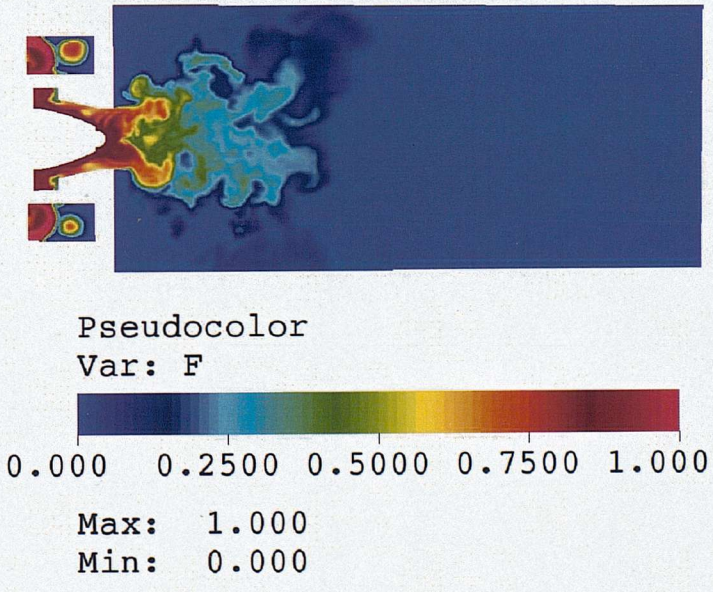


Figure 5.25: Air mass fraction

The velocity profiles presented correspond to the profiles of mean and rms

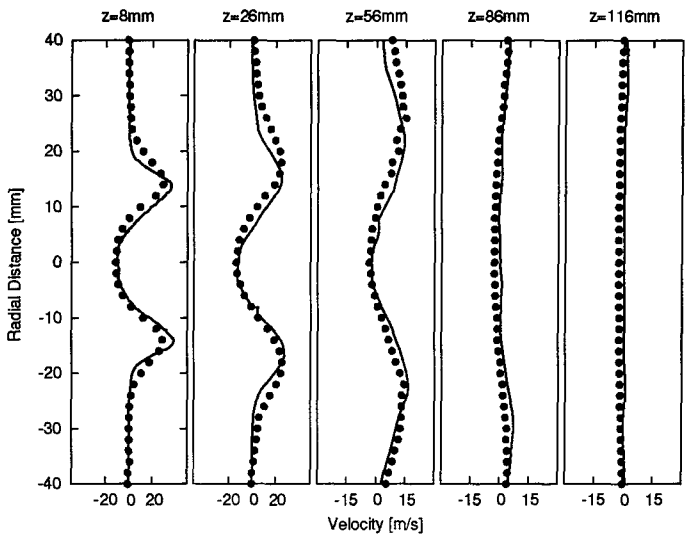


Figure 5.26: Mean Axial velocity - WR=0.284 $Kg/sec\sqrt{K/bar}$

of the three velocity components at a flow rate $WR = 0.142\ Kg/sec\sqrt{K/bar}$. Comparisons of the simulated and measured velocity profiles at flow rates of $WR = 0.284$ and $WR = 0.426\ Kg/sec\sqrt{K/bar}$ demonstrate a similar level of agreement and are reported in figures (5.26)-(5.37).

5.5 Simulation Remarks

In this section the flow topology is discussed. Attention is focused on those turbulent structures which are of interest for the characterisation of the two phase flow. Shear layers generates areas in which the stresses may increase droplet fragmentation. Recirculation zones are responsible for phenomena such as droplet segregation and the creation of fluid pockets in which the local fuel concentration is high.

The swirling flow coming from the injector generates a shear layer which expands in the combustion chamber. The detached flow on the outer corner of the injector-combustor connector creates zones of strong shear at the border of the separation bubble. These areas with high shear can be visualized through vorticity methods.

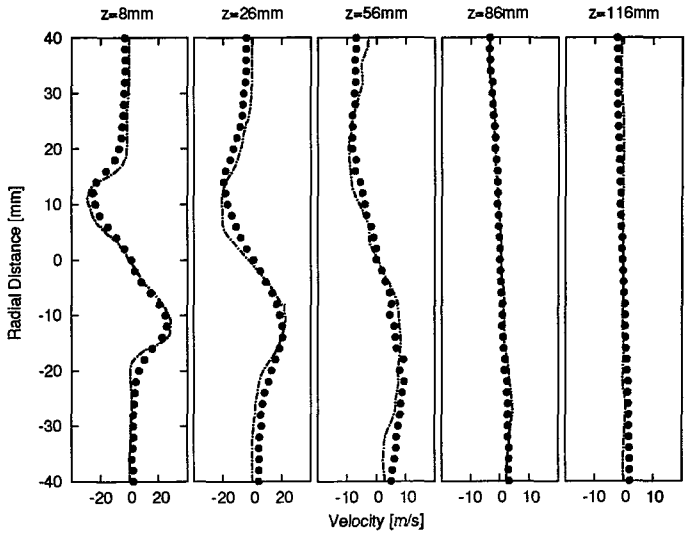


Figure 5.27: Mean Tangential Velocity - WR=0.284 $Kg/sec\sqrt{K/bar}$

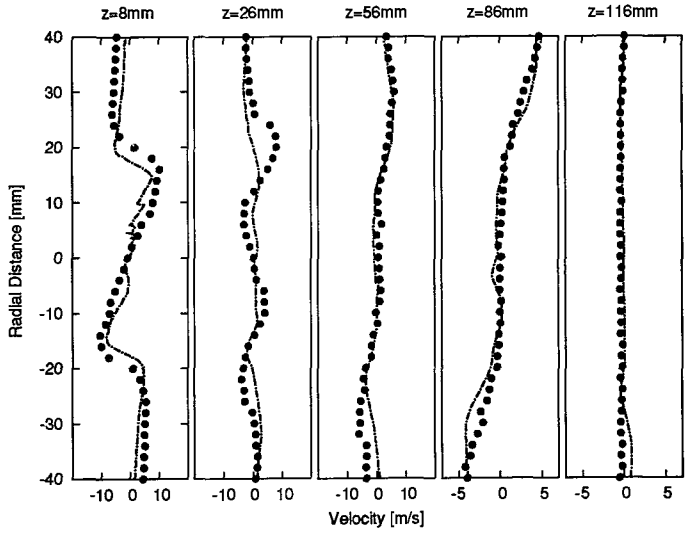


Figure 5.28: Mean Radial Velocity - WR=0.284 $Kg/sec\sqrt{K/bar}$

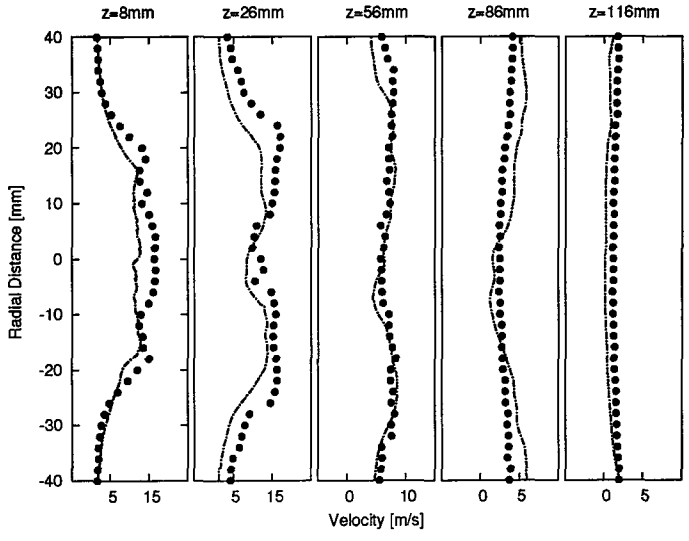


Figure 5.29: *Rms* of Radial Velocity - WR=0.284 $Kg/sec\sqrt{K/bar}$

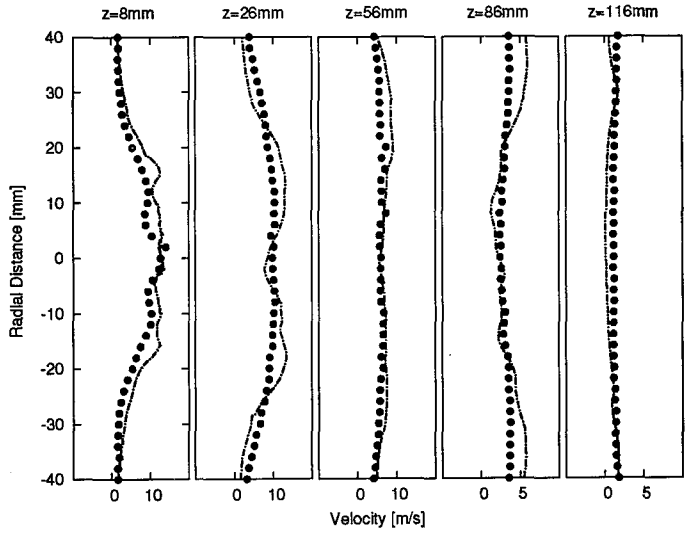


Figure 5.30: *Rms* of Tangential Velocity - WR=0.284 $Kg/sec\sqrt{K/bar}$

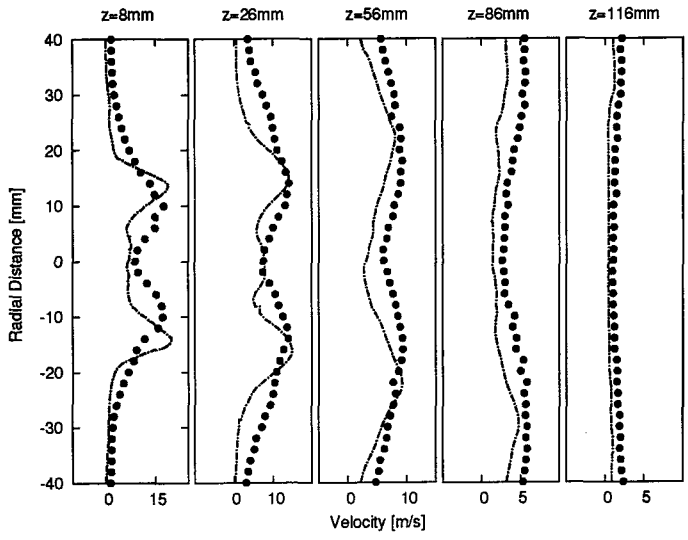


Figure 5.31: *Rms* of Axial Velocity - WR=0.284 $Kg/sec\sqrt{K/bar}$

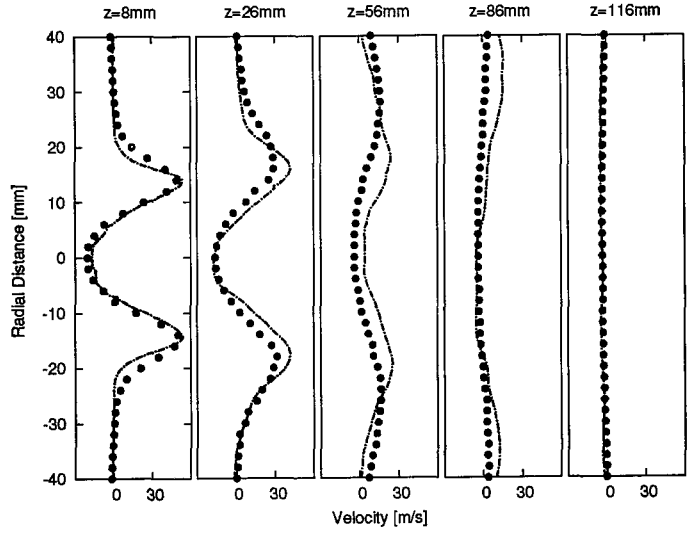


Figure 5.32: Mean Axial velocity - WR=0.424 $Kg/sec\sqrt{K/bar}$

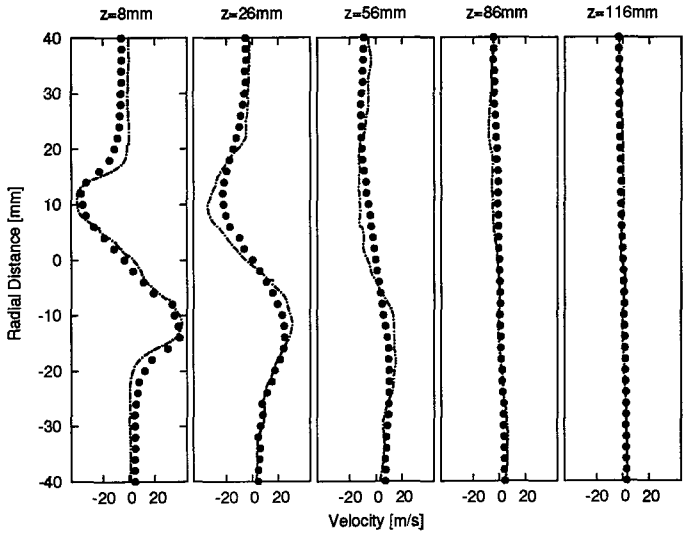


Figure 5.33: Mean Tangential Velocity - WR=0.424 $Kg/sec\sqrt{K/bar}$

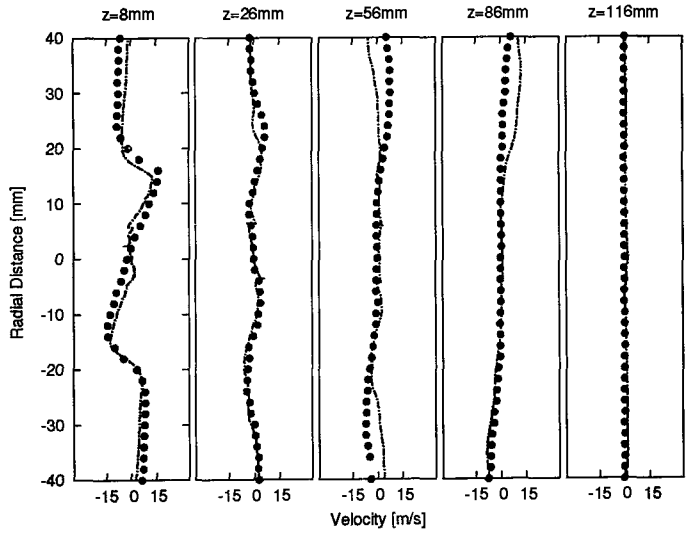


Figure 5.34: Mean Radial Velocity - WR=0.424 $Kg/sec\sqrt{K/bar}$

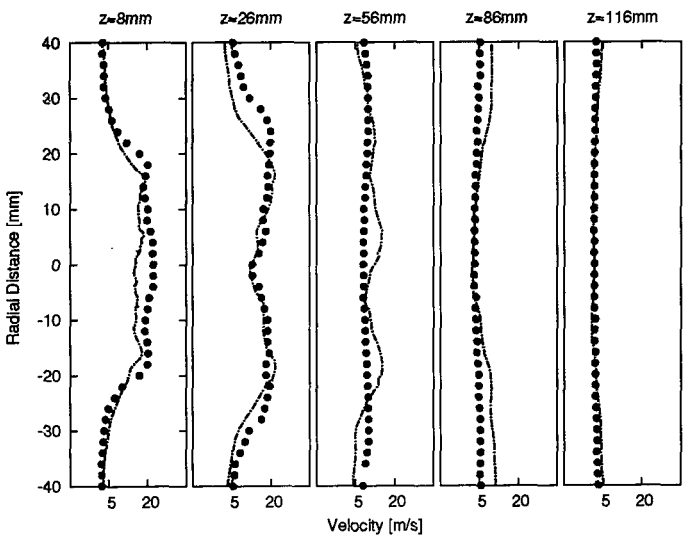


Figure 5.35: *Rms* of Radial Velocity - WR=0.424 $Kg/sec\sqrt{K/bar}$

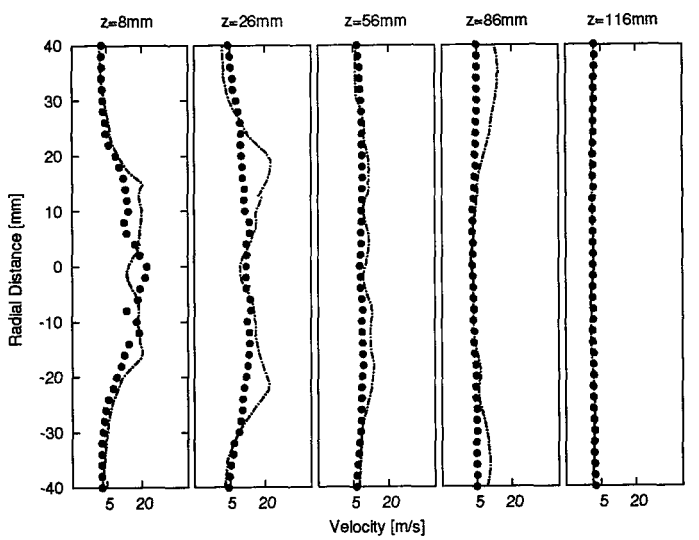


Figure 5.36: *Rms* of Tangential Velocity - WR=0.424 $Kg/sec\sqrt{K/bar}$

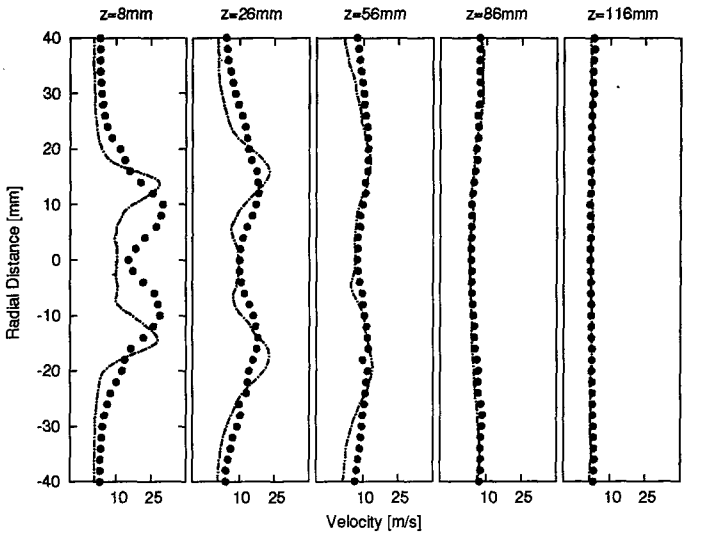


Figure 5.37: *Rms* of Axial Velocity - WR=0.424 $Kg/sec\sqrt{K/bar}$

Recirculation areas are common in aeronautical engines and are often used to create relatively cold air regions in order to prevent the hot gas from the flame to reach the walls of the combustor. In the MERCATO combustor these regions are found in the corners of the chamber, on the sides, forming an annular recirculation zone. The air flow detaches from the wall on the injector tip, due to the sharp geometric edge, generating a burble which evolves into a central recirculation which is clearly visible in all the contour plots of the velocity components. The recirculation areas are shown in figure (5.38) in which the test filtered iso-surfaces of the axial velocity contour displays the recirculation boundaries.

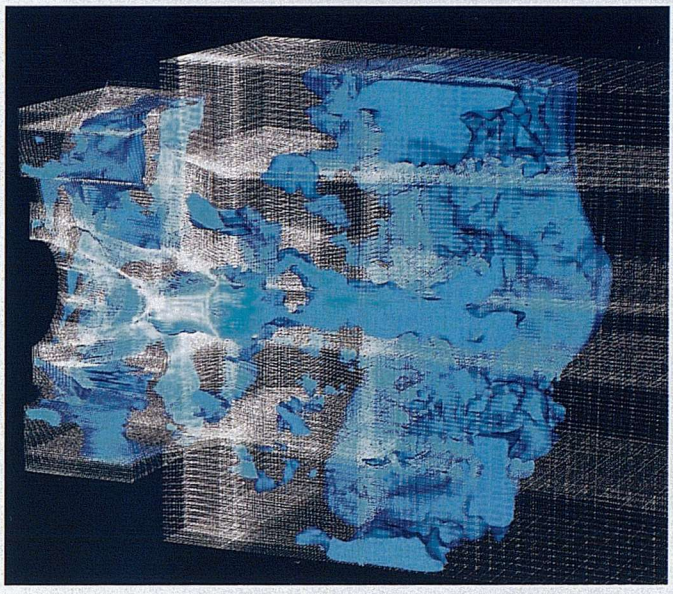


Figure 5.38: Contour plots of recirculation areas

The swirler creates a complex vortex structure which develops in the combustion chamber enhancing mixing and diffusion. This complex structure can be divided in different layers of vortices. A precessing vortex core (PVC) is observed at the tip of the injector. The notion of a vortex itself is widely used in fluid dynamics, however its definition is not straight forward. The most common ways to refer to vortices are not objective as they identify different structures as vortices in frames that rotate relative to each other. However a frame-independent vortex definition is essential. Haller [31] presents a extensive analysis of vortex structure definition which is used in the present work. The PVC is displayed using the q-criterion. This criterion defines a vortex as a spatial region where:

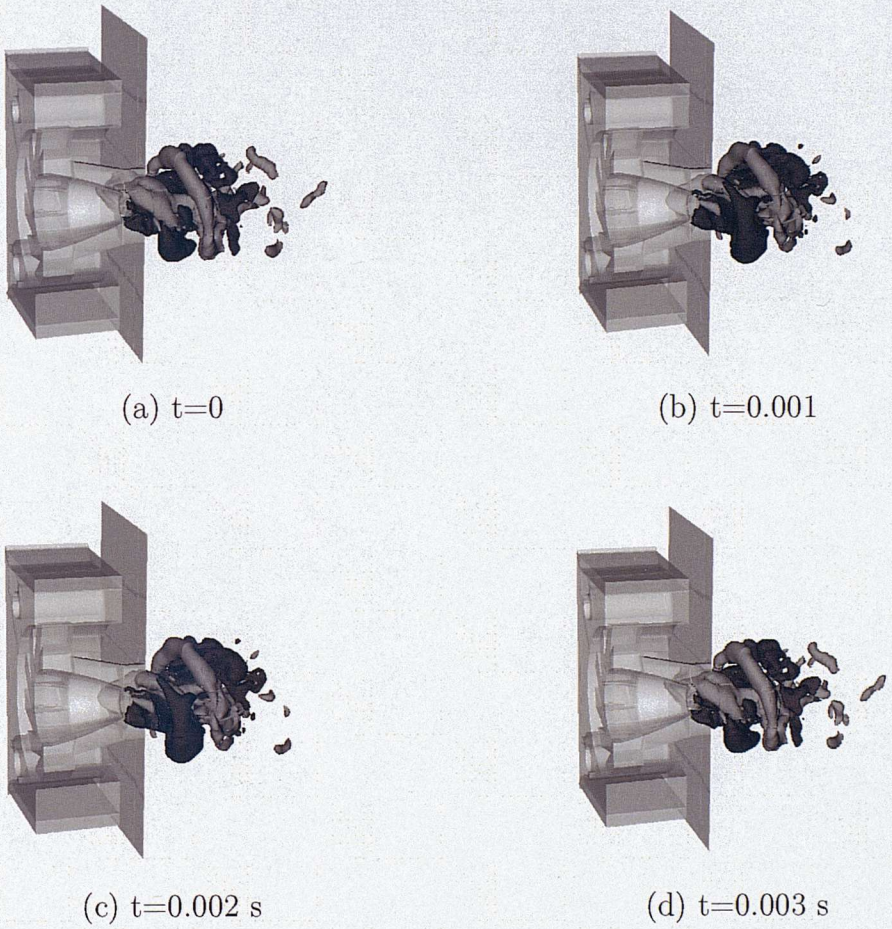
$$Q = \frac{1}{2}(S_{ij}S_{ij} - Q_{ij}Q_{ij}) > 0 \tag{5.1}$$

where S_{ij} is the rate of strain tensor as defined in equation (2.4) and Q_{ij} is the rotation tensor, defined by

$$Q = \frac{1}{2}(\frac{\partial u_j}{\partial x_i} - \frac{\partial u_i}{\partial x_j}) \tag{5.2}$$

Another possible method to isolate the vortex structure is the one which uses the pressure fluctuation [63]. The latter can be computed as $p' = p - < p >$. In

figure (5.39) the isosurface of test-filtered q-criterion show clearly the PVC which forms two distinct substructures which rotate approximatly around the axis of injection. These kind of vortices are characteristic of swirling flows in combustion chambers [78] but also of vortex breakdown in general [30] [52].



(a) t=0 (b) t=0.001

(c) t=0.002 s (d) t=0.003 s

Figure 5.39: Isosurface of Q-criterion at different times (a) - (d)

Experimental evidence of the vortex is given by [49] through the observed values of the velocity and pressure at specific locations. Microphones were placed 8mm downstream from the entrance of the combustion chamber and at 4 locations along one of the measurement directions and 14 mm from the axis of the combustion chamber. The signal from those probes was then processed in order to construct Power Spectral Density (PSD). The frequency of rotation of the

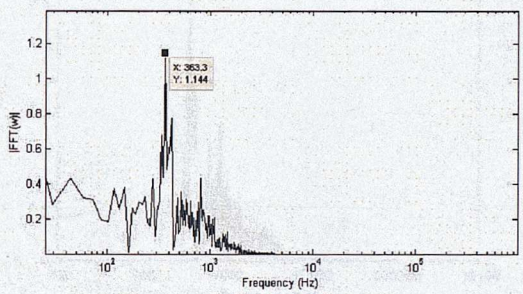
Probe Number	X [mm]	Y [mm]	Z[mm]
Probe 1	14	0	8
Probe 2	0	14	8
Probe 3	-14	0	8
Probe 4	0	-14	8
Probe 5	21	0	10
Probe 6	0	21	10
Probe 7	-21	0	10
Probe 8	0	-21	10
Probe 9	42	0	10
Probe 10	0	42	10
Probe 11	-42	0	10
Probe 12	0	-42	10

Table 5.3: Position of pressure and velocity probes

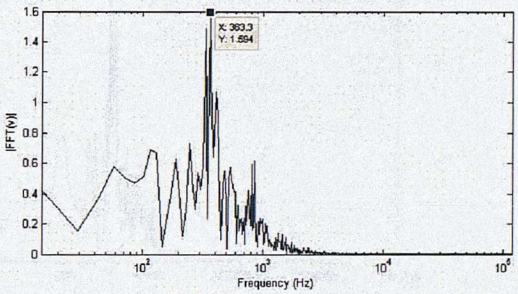
PVC is reported in [49] to have values of about 350 Hz for the $WR = 0.142$ test case and 930 Hz for the $WR = 0.426\ Kg/sec\sqrt{K/bar}$ case. Comparison of the simulated PVC frequency is done via a fast Fourier transform (FFT) of pressure and the three velocity components at specific locations. A common use of Fourier transforms is to find the frequency components of a signal buried in a noisy time domain signal. If data in the form of pressure or velocity components with a well defined frequency is sampled then the PVC rotation frequency will be hidden in the random noise characteristic of turbulent motion. The FFT allows the decomposition of the global signal in harmonics which will display how the " *information*" related to the signal is distributed in the frequency space. In this way the passing of the PVC through at a probe location is analysed and extracted by the FFT. The computational probes are positioned as reported in table (5.3).

The FFT analysis of the pressure and the three velocity components shows a peak at a frequency of 363 Hz for the $WR = 0.142$ case and 953 Hz for the

$WR = 0.426\ Kg/sec\sqrt{K/bar}$ test case. Comparison of the computed values with the experimental findings of [49] as reported above show that the simulation is able to capture the correct frequency of the PVC. Figures (5.40)-(5.42) show the FFT of the axial and the transverse velocity components and the pressure for Probe 1 for the two test cases along with the value of the frequency of the maximum of the FFT. The same analysis is performed for all the probes and typical results are reported in figures (5.43) to (5.45). Probes 9 to 12 are intentionally positioned far from the PVC area so that the analysis of the spectra does not contain the peak which is characteristic of the PVC. In these graphs the energy is distributed over low frequency due to the relative slow motion of the recirculation area where the probes are located. An example of probe signal is displayed in figure (5.46).

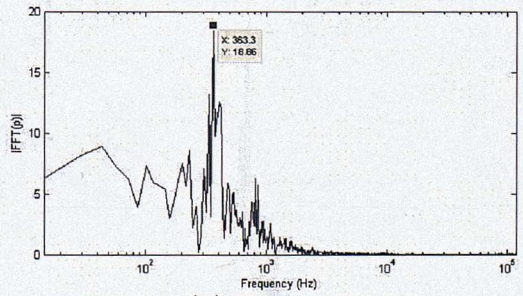


(a) Axial

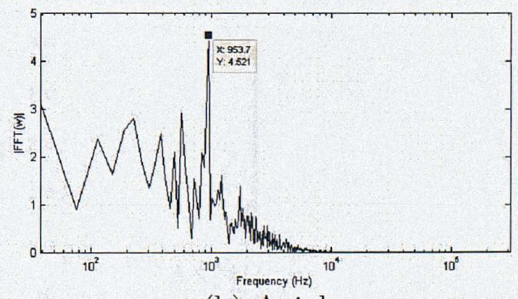


(b) Transverse

Figure 5.40: FFT of velocity components of test case WR=0.142 for Probe 1 - Axial (a) Transverse (b)

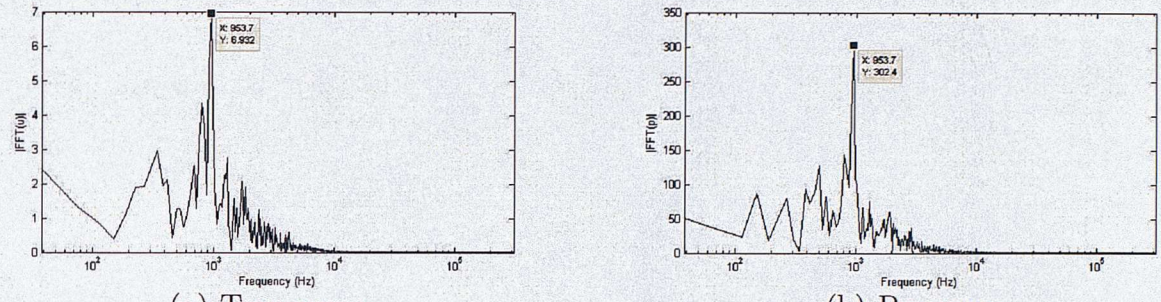


(a) Pressure



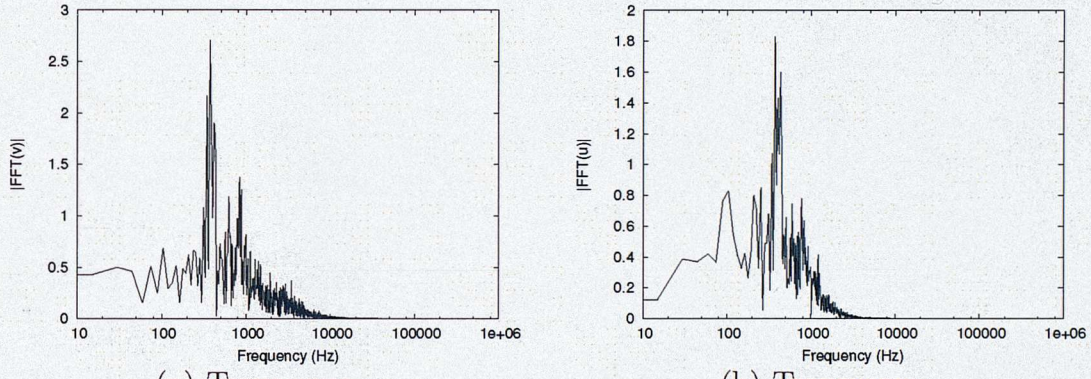
(b) Axial

Figure 5.41: FFT of pressure of the test case WR=0.142 and velocity component of test case WR=0.426 for Probe 1 - Pressure (a) Axial (b)



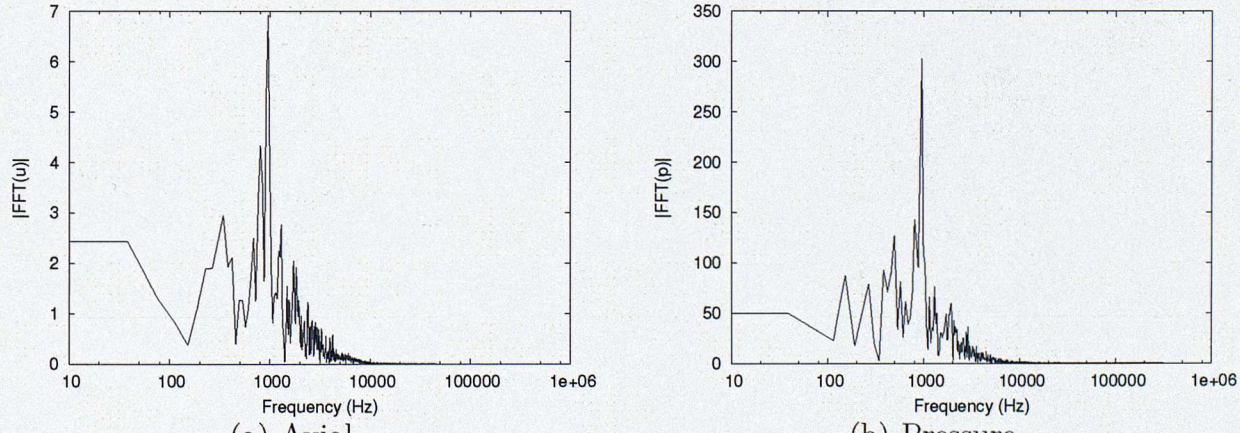
(a) Transverse (b) Pressure

Figure 5.42: FFT of velocity components and pressure of test case WR=0.426 for Probe 1 - Transverse (a) Pressure (b)



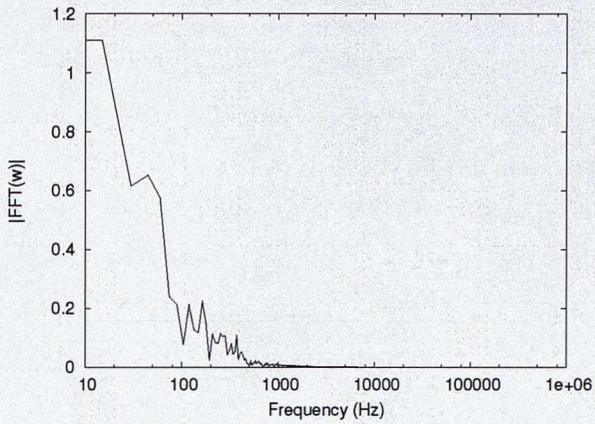
(a) Transverse (b) Transverse

Figure 5.43: FFT of Transverse velocity components case WR=0.142 - Probe2 (a) Probe5 (b)

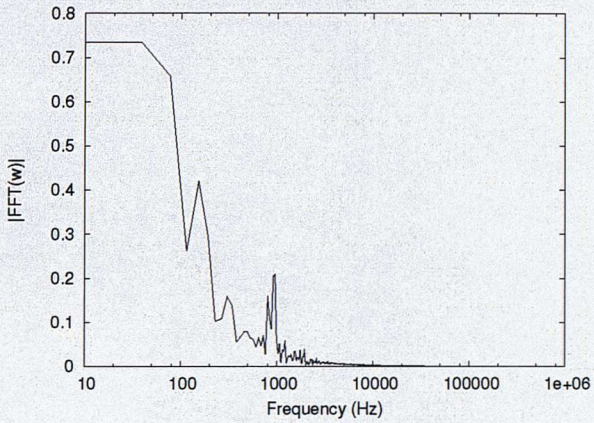


(a) Axial (b) Pressure

Figure 5.44: FFT of Axial velocity component and pressure for case WR=0.426 - Probe5 (a) Probe6(b)

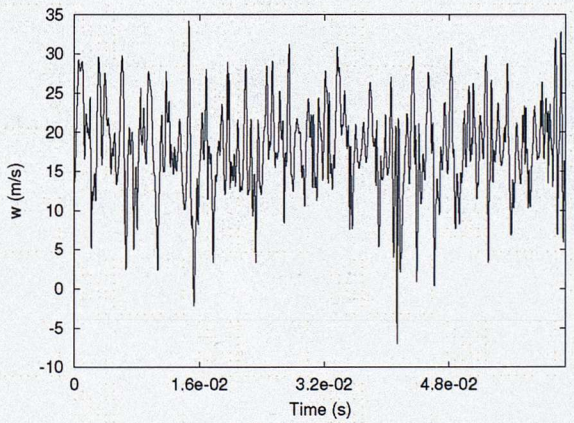


(a) Axial

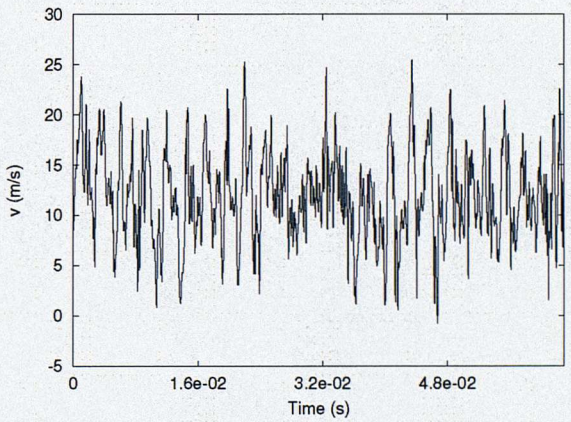


(b) Axial

Figure 5.45: FFT of Transverse velocity components for probe 10 - case WR=0.142 (a) case WR=0.426 (b)



(a) Axial



(b) Transverse

Figure 5.46: Probe signal of test case WR=0.142 - Axial velocity component(a) Transverse velocity component (b)

5.6 Two Phase Flow

In the two-phase flow simulation liquid Kerosene is injected into the combustion chamber starting from a well established solution of the gas phase flow. Several injection regimes were studied experimentally. However, in the present case only the low flow rate configuration is considered, as measurements at high kerosene flow rates were restricted exclusively in the 6mm plane, due to the observation window being 'flooded' by liquid kerosene as a result of impinging droplets. In all the simulations breakup, evaporation and dispersion of the droplets are considered, along with two way coupling of mass and momentum between the gas and liquid phase.

5.6.1 Injector characterisation

The injector characterisation represents the greatest uncertainty as the droplets diameter and velocity distribution at the injection point are unknown. Experimental PDA measurements are taken at a distance of 6 mm from the inlet of the combustion chamber or 10 mm from the injector. Additional uncertainty is added because of the lack of precise data about the injector operating regimes, in the form of pressure, velocity and internal perturbation of the initial liquid jet. The injector is a Delevan model 46917-13, which has a hexagonal base and a tip of 2.79mm. The injection system itself has a rather simple geometry. The air circuit is composed of a pure radial swirler and an axial convergent nozzle with a cylindrical exit. Inside the convergent nozzle, shaping its inner wall, an ovoid nose holds a pressure swirl fuel injector. This ensembly is held by four columns on a plate, which forms the injection face and, thus, the head end wall of the test chamber. A schematic and a picture of the injector are shown in figures (5.47) and (5.48).

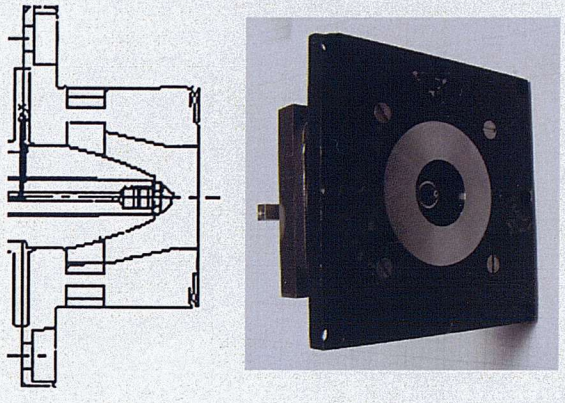


Figure 5.47: Injector schematic and perspective view

Liquid Kerosene is injected from the tip of the injector with an hollow cone pattern into the combustion chamber, as is illustrated in figure (5.49). The angle of injection is estimated using the experimental data at 6mm downstream of the injection point where droplets are found to encompass a circular area of about 30 mm radius. The angle of injection can be estimated after taking into account the liquid deflection due to the gas flow, as shown in figure (5.50).

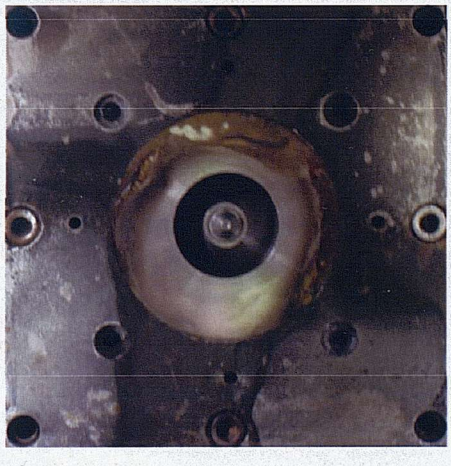


Figure 5.48: Injector, frontal view

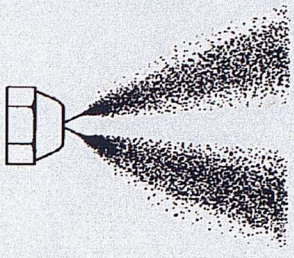


Figure 5.49: Hollow cone pattern

The spray angle α is defined as the apex angle of the spray and is often measured by drawing two straight lines from the discharge orifice to some specified distance downstream of the nozzle where the jet narrows under the influence of the surrounding gas. In the MERCATO experiment droplets were found in a circular section of diameter $\overline{A'B'} = 60mm$, at a distance of 10mm from the point of injection forming a modified injection angle α'. Bayvel and Orzechowski [6] give a different expression for α depending on the gas velocity, the injector discharge pressure and flow rate, the liquid fuel composition and density, the droplet diameter distribution and the angle α'. In the present work, because of the lack of data on the injector, α was found empirically by trial and error for each test case until the correct α' was reproduced at the 6mm downstream location.
In the simulation, droplets of diameter corresponding to the nozzle size are injected following the same injection methodology used in section 4.6.1. The liquid injection velocity is obtained from the nozzle diameter and the kerosene mass flow rate and applies to all the droplets. The injection volume flux distribution consistant with the measured distribution is achieved by using the acceptance inverse transformate sampling over the measurement of the volume flux at the 6mm downstream location. The breakup constants β and C_b are adjusted in order to reproduce the injector characteristics.

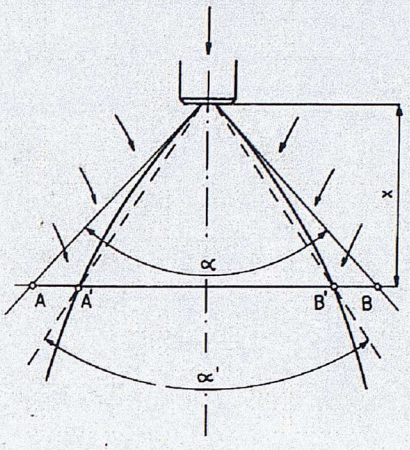


Figure 5.50: Schematic of injection configuration and angles

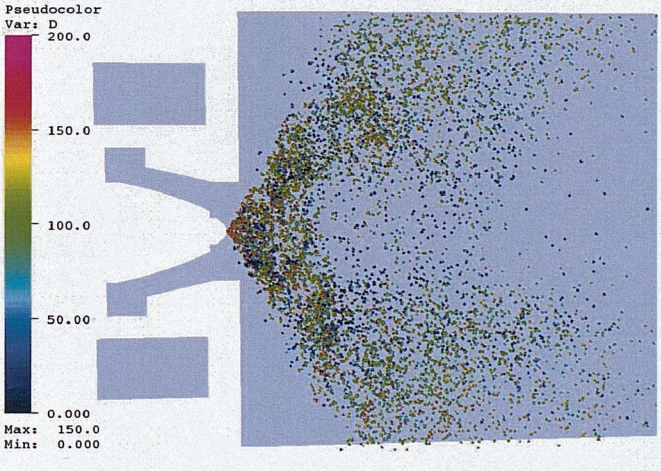


Figure 5.51: Kerosene Droplets by diameter

5.6.2 Validation

Results for the liquid phase for $WR = 0.142\ Kg/sec\sqrt{K/bar}$ and low kerosene flow rate are presented in figures (5.52)-(5.60) in the form of a comparison of the measured (filled dots) and computed (open circles) radial profiles of the Sauter

Mean Diameter, mean radial and transverse velocities and mass flow rate of Kerosene droplets at several axial distances from the entrance of the combustion chamber. A polynomial fit of the computed values is presented in the figures along with the experimental and computational data. Because of the Lagrangian particle tracking methodology adopted, computational results show the presence of droplets close to the center line. However, it is clear from the analysis of the contour plot that droplets are found in this region only occasionally. This "empty" zone shows scattered points which arise from the random passing of a single particle. The liquid phase statistics are effected by this one-time occurrence. As the statistics are slow to converge in these areas, the polynomial fit of the computed values is shown in order to indicate the global trend.

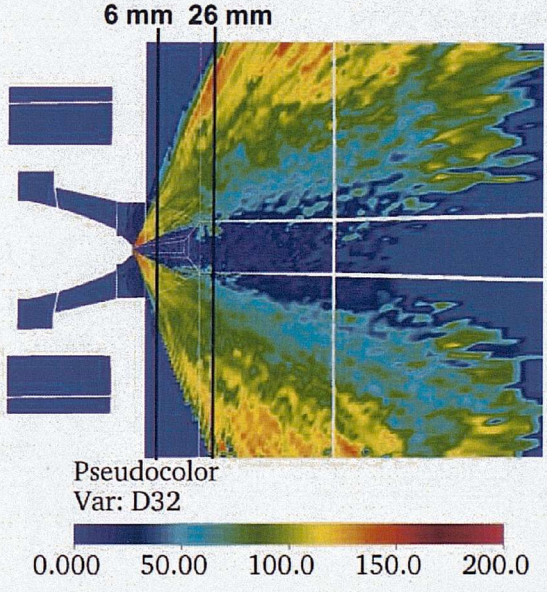


Figure 5.52: Sauter Mean Diameter contour with measurement locations

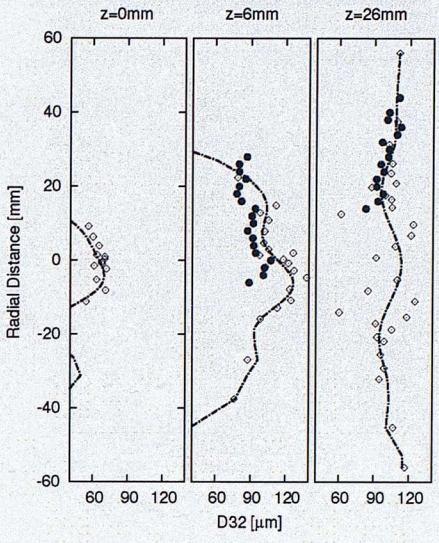


Figure 5.53: Sauter Mean Diameter. Filled dots represents experimental data, dots represents the results of the simulations, lines are polynomial fit of the computed values

The SMD profiles, figure (5.53) show good agreement between the simulated values and the experimental data. The profile at z=0 is plotted in order to show the evolution of the droplets diameters starting from the chamber entrance: at z=0 droplets are clustered in a circular section of 10 mm radius. The SMD is almost constant on the center line with a value of $90\mu m$. The droplets break rapidly from the injection diameter of $200\mu m$ in the first 4mm with small and big fragments moving together. Tiny pockets of droplets are formed on the sides and are visible in the profile and the contours. At z=6mm there is a slight overestimation of the size in the centre and at a radius of 20 mm from the combustor axis. The droplets spread covering a wider area with the large fragments in the middle, with the small droplets being transported outside by the swirling motion of the gas phase. From the instantaneous snapshot, figure (5.51), it is evident that the large recirculation zone in the central area traps the large fragments. The profile at z=26mm section yields good agreement with the experimental data. The large droplets evident at z=6mm are captured by the recirculation and do not reach the downstream location z=26 mm. The trend is reversed with small fragments in the centre and some larger droplets transported outside by the swirling motion.

In the simulated profiles the presence of a few scattered droplets passing in the centre is clearly visible. However, the contour plot in figure (5.54) shows clearly the hollow cone structure of the spray.

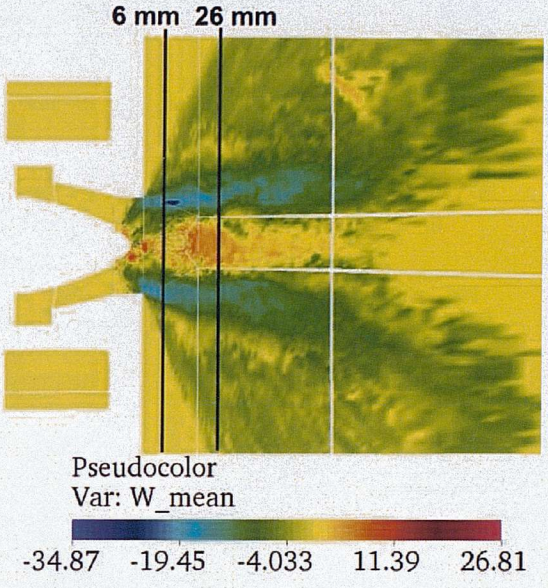


Figure 5.54: Liquid Mean Axial Velocity contour with measurement locations

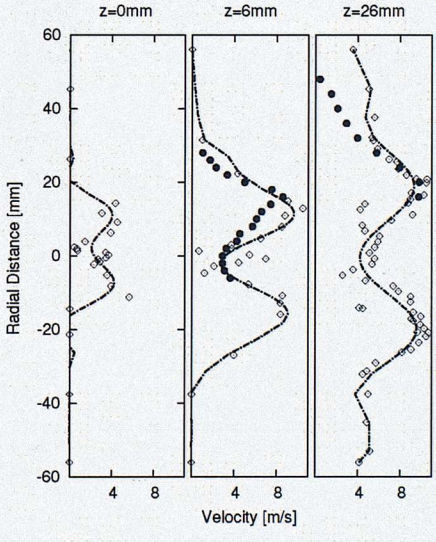


Figure 5.55: Liquid Mean Axial Velocity. Symbols are the same as figure (5.53)

The mean axial velocity in figure (5.55) appears to be well reproduced. A small over prediction of the velocity of the droplets is evident far from the center

line in both the measurement locations. The global behavior is well represented: the droplets are injected with a fixed velocity and by interacting with the gas phase the particles decelerate in the central recirculation area, and accelerate in the shear layer. The resulting profile is in good agreement with the experimental data. From the contour plot the presence of two small recirculations is evident on the sides of the tip of the injector which capture the droplets and generate segregation.

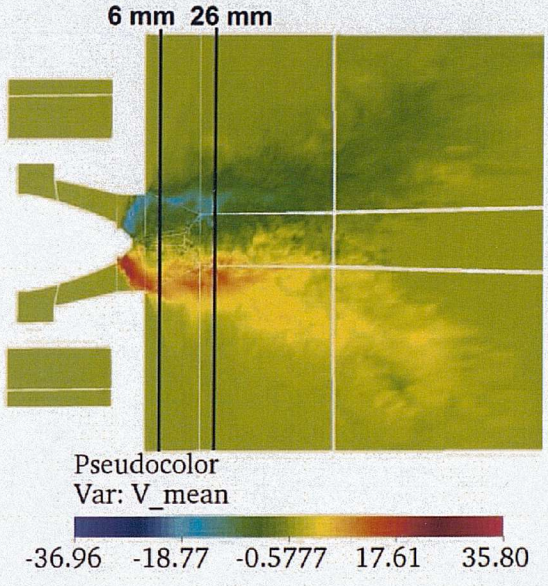


Figure 5.56: Liquid Mean Transverse Velocity contour with measurement locations

The liquid azimuthal velocity (figure 5.57) shows a small overestimation of the value at z=6mm, where the droplets appear to be 'rotating' slower than in the experiment. However, this behavior is likely to be due to the fact that droplets are injected without any swirling velocity in the simulation. The lack of information about the injector did not allow accurate boundary conditions to be applied for the liquid phase. In many atomizers the flow exits the nozzle with an initial swirling velocity which serves to enhance fragmentation. However, the under estimation of the azimuthal velocity is small and the behavior of the droplets seems to be well reproduced at z=26 mm.

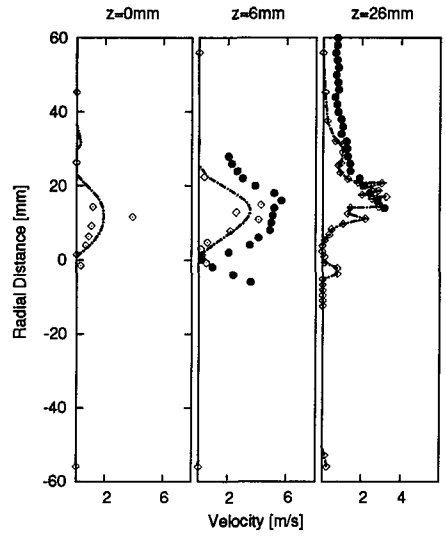


Figure 5.57: Liquid Mean Transverse Velocity. Symbols are the same as Figure 5.53

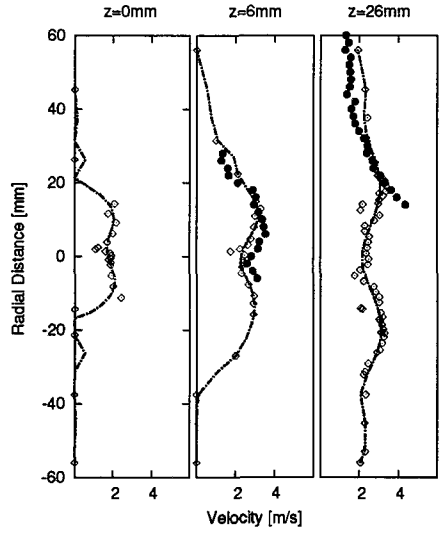


Figure 5.58: *Rms* of Liquid Axial Velocity. Symbols are the same as Figure 5.53

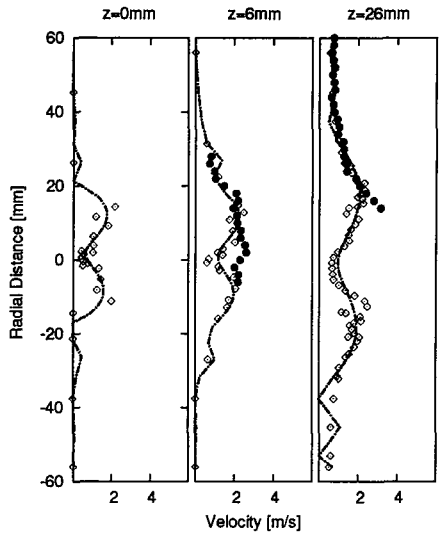


Figure 5.59: *Rms* of Liquid Transverse Velocity. Symbols are the same as Figure 5.53

The simulated rms of the axial and traverse velocity are in good agreement with measurements in both the locations.

The computed volume flux in figure (5.60) shows a peak along the center line which is not evident in the experimental data. The overall agreement between the measured and simulated profiles is, however, good.

5.7 Discussion

The analysis of the interactions between continuous and dispersed phase is important for understanding of the liquid phase results such as droplet distribution and velocities. In section 5.5 some of the main features of the turbulent flow are reported, including the observation of a PVC. This turbulent structure influences strongly the spray properties, defining droplet segregation, enhancing evaporation and generating droplet breakup.

Figure (5.61) is the instantaneous isosurface of gas temperature showing the region of the flowfield where the temperature is colder than the injected value of

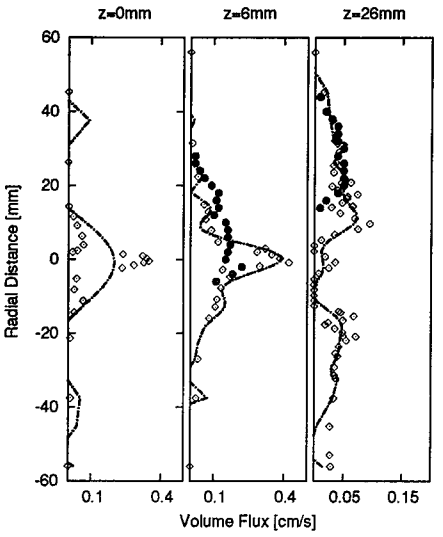


Figure 5.60: Liquid Volume Flux. Symbols are the same as Figure 5.53

463K. When the liquid droplets are injected, some of them are captured by the PVC core. In this region the particles encounter suitable conditions for break up: in chapter(4) the relation between breakup frequency and ϵ is introduced, explaining how the droplet fragmentation is effected by the turbulence. The droplets atomise inside the PVC and evaporate faster; some droplets are also trapped inside the vortex structure. The results is that the internal temperature of the PVC is colder than that of the outside gas. Figure (5.62) represents an instantaneous snapshot of the droplets at a time t=0.005 sec after injection when droplets are observed to fill the combustion chamber. From the figure it is clear that particles are concentrated in the shear layer, in the PVC and the central recirculation. Several droplets are captured by the lateral recirculation and transported to the corner area, so that the observation of the droplet distribution inside of the domain clearly reflects the gas phase flow structure. Recirculation areas are responsible for creating pockets of droplets which in time generate regions of the flow particularly rich in Kerosene vapour. The Kerosene mass fraction contour plots are discussed in chapter (6).

The effect of the PVC on the droplet size distribution is analysed in figures (5.63) and (5.64). The figures show the SMD at z=6mm and z=26 mm for the

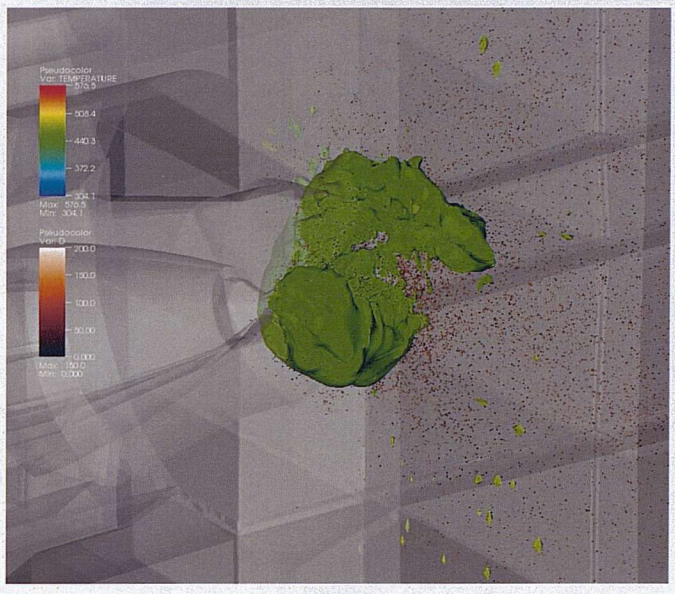


Figure 5.61: Isosurface of Temperature showing evaporation in the PVC

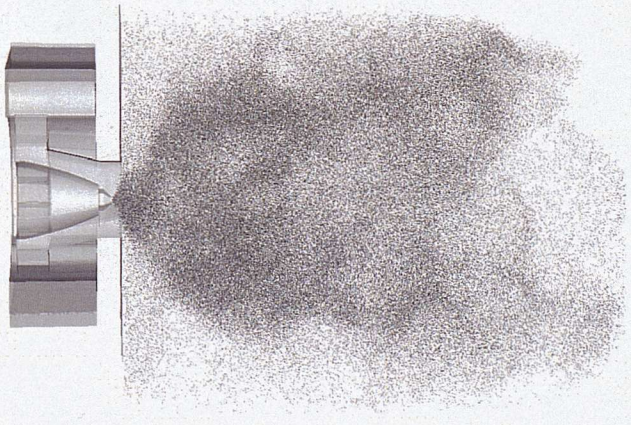


Figure 5.62: Liquid Injection

test case I, with the low resolution grid. In this case the PVC is not properly reproduced, probably because of the low resolution of the grid in the swirler and on the walls of injector channel. In spite of this at z=6mm the predicted droplets size are in good agreement with the experimental findings. It is clear, however, that at z=26 mm the slope of the diameter distribution is wrongly captured. From the analysis of the breakup characteristic properties of the single fragments it is clear that the PVC exerts a dramatic effect on breakup. Without the PVC droplets are less likely to break and there appear to be little droplet segregation, in contrast with the experiment.

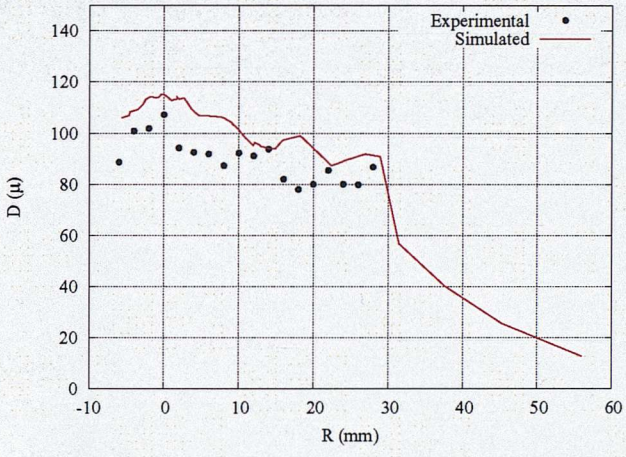


Figure 5.63: Sauter Mean Diameter z=6mm

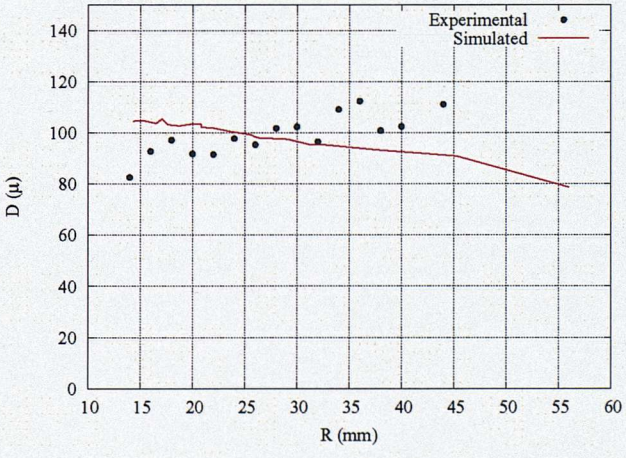


Figure 5.64: Sauter Mean Diameter z=26mm

The relative importance of breakup in reproducing the correct droplet size distribution is demonstrated also by the analysis of the profiles of mean and Sauter mean diameters in figures (5.65) and (5.66) taken from [80, 81]. The figures represent the size distribution profiles for a simulation on the very same MERCATO test bench, but with different inflow conditions and without a breakup model. Droplets were injected into the combustor with a initial estimated distribution and only evaporation and dispersion were considered. The simulated values fail to reproduce the experimental findings, suggesting that the inclusion of the breakup process is probably essential if the correct physics of the process are to be captured.

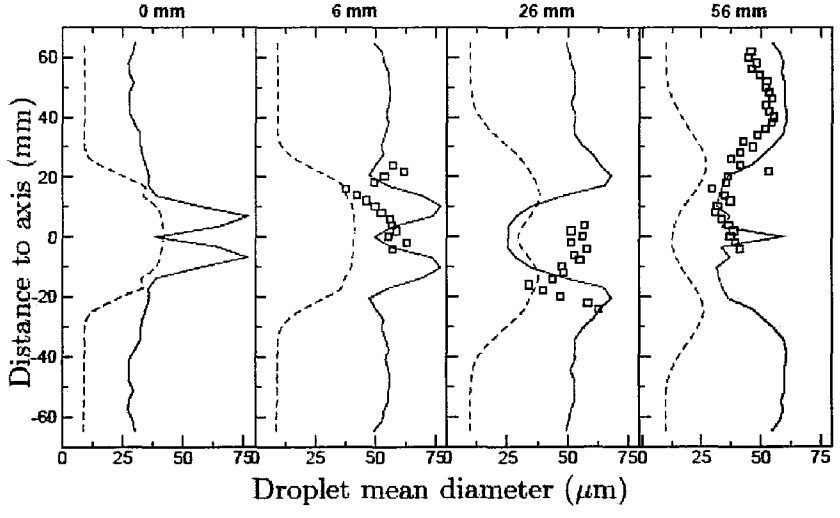


Figure 5.65: Mean droplet diameter

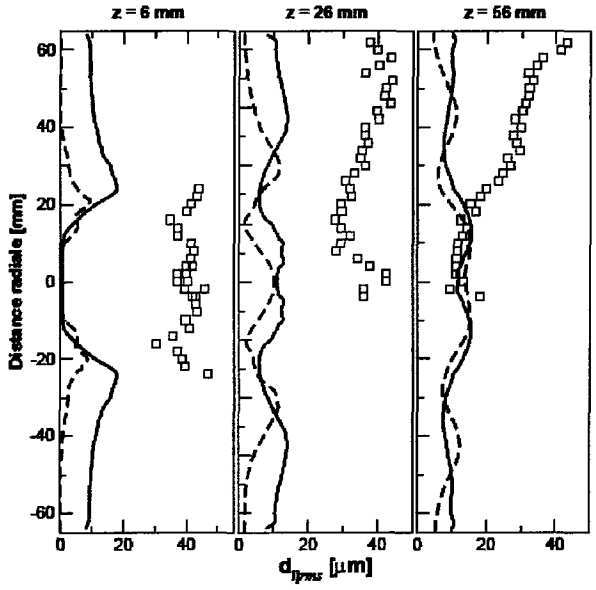


Figure 5.66: SMD

5.8 Conclusions

The present chapter has presented a comparison of simulations obtained using the LES-Lagrangian particle methodology with measurements in an experimental burner. The predicted profiles of the mean and *rms* velocities of the gas phase are in good agreement with measurements, demonstrating the efficacy of the LES implementation. Droplets are injected into the combustion chamber with a fixed diameter and at room temperature. The liquid droplets on interaction with the turbulent structures of the shear layer of the swirled air jet, undergo fragmentation and vaporization. The good agreement of the predicted profiles of droplets size and velocities with the experimental data demonstrate the effectiveness of the models implemented.

Globally the physics of the two phase flow appears to be well represented by the simulations. A central gas recirculation at the injector tip captures the droplets which by the 6mm plane form a solid cone spray of approximately 60 mm diameter. At increasing distance downstream of the injector, the spray evolves into a hollow cone with droplets that form dense pockets in the shear layer of the

swirler flow. A relative low droplet density is observed close to the centre line at a 26 mm section from the entrance of the combustion chamber. With regard to the liquid phase, improvement to the simulations could probably be achieved if the geometric details of the injector were known to a greater accuracy. In this regard the choice of a test case with more detailed information on the injector would represent a good case for further investigation.

Chapter 6

Large Eddy Simulation of turbulent reacting flow in an experimental burner - Ignition

6.1 Introduction

The present chapter considers an investigation of the ignition of the MERCATO combustor. The geometry of the case considered is closely similar geometry to that considered in the two phase-flow simulations of the previous chapter. The simulations are performed starting from a well established solution of the two-phase flow and then igniting it with a spark. The inlet conditions of the gaseous and liquid phases are adjusted in order to achieve conditions suitable for combustion. A number of test cases are considered in which ignition was not successful. Combustion is observed after ad-hoc modifications of the inlet conditions and is studied through the analysis of scatter plots of the fuel mixture fraction and temperature and mean profiles of the gaseous phase.

The first part of the chapter briefly introduces the test case considered, providing key information about the experimental procedure. In the second part a case of failed ignition is presented. The main reasons for the failure in generating a stable

combustion are analysed, leading to modification of the test conditions. Finally a case in which ignition produced a nearly extinguishing flame is reported, with detailed information about the flame characteristics. Finally the results of the simulations are analysed and possible solutions to the problem are proposed.

6.2 Overall features of the ignition experiment

The ignition tests are performed on the same experimental set up as the one used for the two-phase flow characterization, which is extensively described in chapter (5). The objective of the experimental campaign is to determine, at ambient conditions, the ignition boundary as a function of flow rate, kerosene flow rate and spark-plug position. The experiments were conducted at room temperature and involved a train of sparks which was applied continuously for a duration of 5.5 s. The deposition of the sparks starts after t=0.1 s from a well developed two-phase flow condition in the combustion chamber. The spark system is located on one of the walls by substituting one of the observation windows used in the isothermal study. The ignition of the mixture was clearly visible from the recorded pressure curves, because of the increase in the chamber pressure at ignition, which causes a pressure drop in the ignition system. Figure (6.1) shows the spark sequence and the pressure drop for a typical ignition test case. Figure (6.2) represents a close-up of the spark sequence versus pressure drop at the instant when the flame ignites. The interval between two successive sparks was approximately 0.16 s, and a single spark lasts about 10 ms. Ignition is usually achieve after at least 10-20 unsuccessful sparks with the train of sparks held active after the ignition and during flame propagation. The ignition process lasts roughly 50-100 ms: results come in the form of images of the flame obtained from the front and side windows from which the flame centre, area and perimeter are estimated. Images of the flame were obtained taken for 0.25 up to 1 sec. Seventy two different configurations were investigated by changing the air flow rate, the kerosene injection rate and the position of the spark. The spark plug locations were positioned on the wall at 26, 56, 86 and 116 mm from the inlet of the combustion chamber. The spark was also moved slightly inside the chamber, corresponding to a 2mm

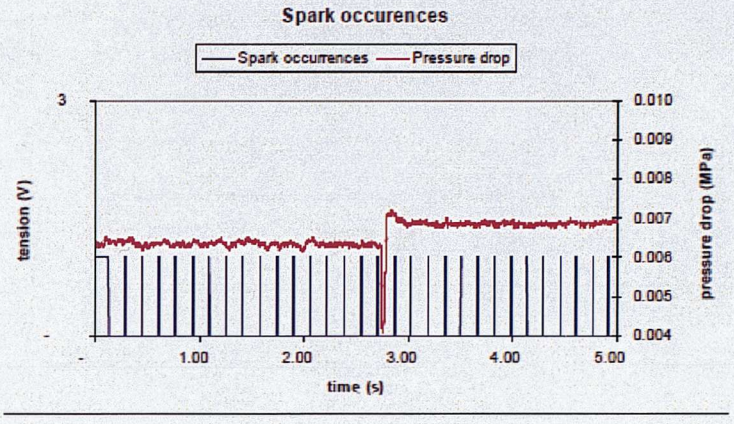


Figure 6.1: Spark occurrence (Volt) versus pressure drop

protuberant. For each of these configurations, several tests were performed, leading to a total of 596 tests.

6.3 Simulations

The simulations are performed with the in-house LES code Boffin. The energy deposition of the spark is modelled by the addition of a source term in the enthalpy equation. The model adopted is the Energy Deposition (ED) model, described by [46]. The volumetric source term added to the enthalpy equation has a Gaussian distribution in space and time and is defined by:

$$\dot{q}_{sp}(r) = \frac{Q_{sp}}{4\pi^2\sigma_s^3\sigma_t} exp\left[-0.5\left(\frac{r}{\sigma_s}\right)^2 - \left(\frac{t-t_0}{\sigma_t}\right)^2\right] \tag{6.1}$$

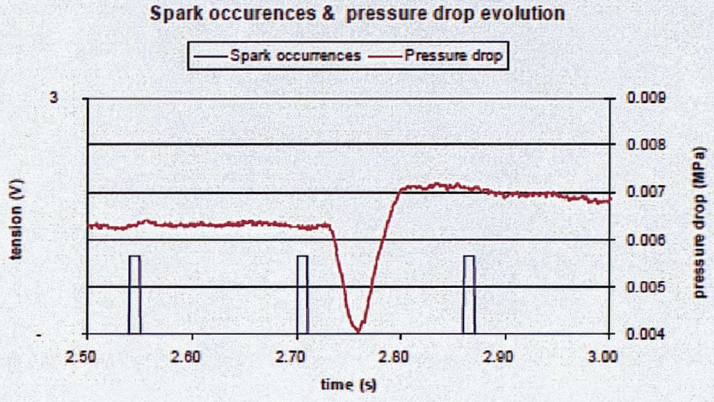


Figure 6.2: Spark occurrence (Volt) versus pressure drop - Ignition close-up

where $\sigma_s = \frac{\Delta_s}{a}, \sigma_t = \frac{\Delta_t}{a}$ determine the size and length of the spark. Δ_s can be estimated from $\Delta_s \approx \left(\frac{Q_{sp}}{\rho C_p (T_{max} - T_0}\right)^{1/3}$, where $T_{max} = 3500$ K as suggested by Lacaze et al. [46]. Q_{sp} is of the order 10 mJ. With this given approximation, Δ_s is about 4 mm and the spark duration is about 10ms. This model has been shown to ensure that the correct energy is deposited, whilst not creating unphysical high temperatures for a long time period. Figure (6.3) shows the theoretical evolution in time of the maximum temperature.

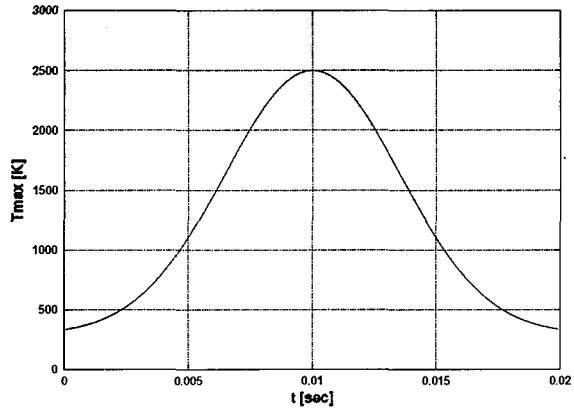


Figure 6.3: Gaussian distribution of spark Temperature

The combustion of kerosene is approxinaed by a four step mechanism [98] and sub-grid scale fluctuations are handed with the sgs-pdf [97]. Ignition tests are simulated starting from a well established solution of the two-phase experiment. At $t = 0.05$ sec after the beginning of the kerosene injection the flow and the droplet distribution appears to be fully developed and the spark deposition is started. Simulations are conducted over selected test cases selected from the ignition experiments presented in [48]. Figure (6.4) shows the experimentally observed ignition boundaries versus the spark plug abscissa. The plot also shows the different values of the fuel-air ratio (FAR) for each mass flow rate.

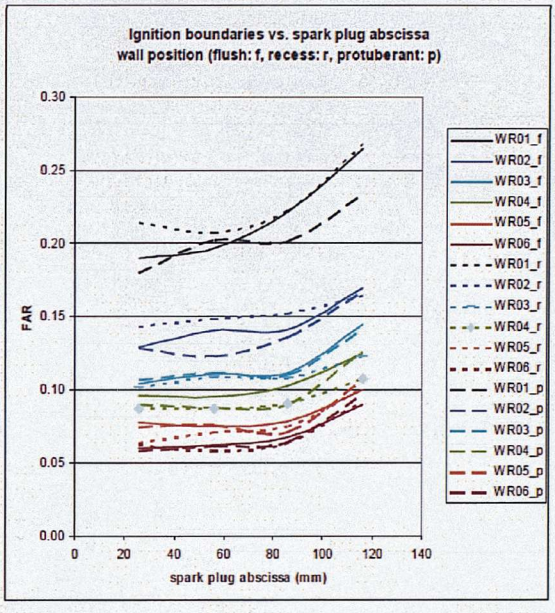


Figure 6.4: Spark plug abscissa versus FAR

At first, attention is focused on the experiments with a mass rate and kerosene flow rate similar to those considered in the two-phase cases of chapter (5). This is because of the demonstrated ability of the method in reproducing the correct physics of the gas and liquid phase for these specific conditions. A preliminary analysis reported in section (6.3.1) showed that most of the two-phase characterisation cases were performed with low values of the FAR, making the air-fuel mixture relatively lean and thus difficult to ignite. In this regard, the test cases in the range of WR=0.2 represent a good compromise. The flow rate is similar to

the validated two-phase experiments while the kerosene flow rate is twice as big as those considered in the high flow test cases of chapter (5). The experimental visual observation of the combustion for these test cases displayed flames mainly yellow and white, a sign of rich combustion.
The typical computational time required by an LES for the solution of flow is relatively high: the global time required by a single run depends on the computational resources available and the accuracy requirements dictated by the time resolution. In most of the cases the overall time period which can be investigated by mean of LES is small compared to the duration of the spark sequence. A simulation of the complete ignition procedure covering a period of 5.5 sec is practically unfeasible from a computational point of view. Given the spark train duration and the necessity of having an adequate gap between sparks, in a typical LES simulation no more than one or two sparks can be investigated. This makes the selection of a good test case an important issue. In this respect, the test cases with WR=0.2 represent a good choice as it has been demonstrated to have a good ignition probability, with successful ignition occurring after 7-15 sparks compared to the 20-30 of the other cases. In what follows both unsuccessful and successful ignition test cases are reported.

6.3.1 Failed Ignition

A number of unsuccessful ignition tests are investigated using a air mass rate WR of 0.142. The spark location is chosen from considerations based on the vapour kerosene concentration and the results of the experiments [77]. In the experiments the spark is located close to the wall. From the analysis of the kerosene mixture fraction and droplet distribution this location does not seem to be favorable for a successful ignition; figure (6.5) shows the kerosene mixture fraction in the combustion chamber.

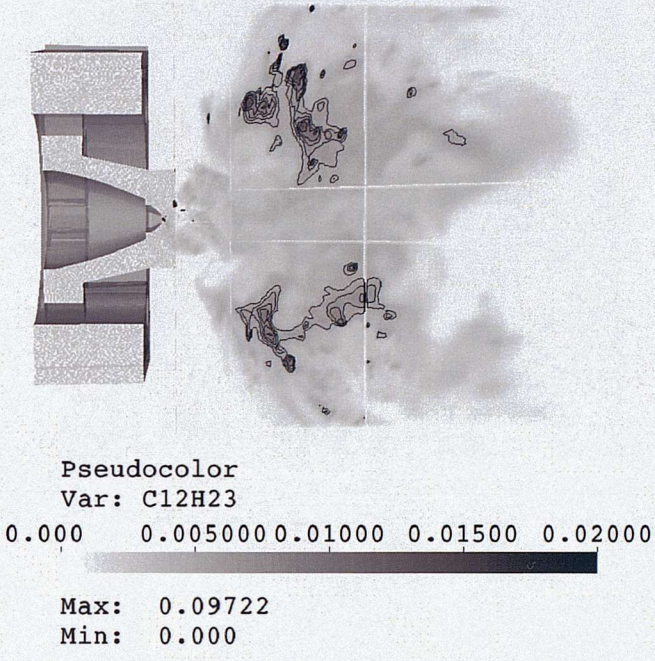


Figure 6.5: Kerosene mass fraction isosurface and contour

The fuel vapour is distributed over the chamber with a maximum of 0.09 close to the injector. Apart from this very rich area close to the injection point, a zone with a lean, but still significant, FAR is evident in the recirculation zone at a distance between 26 and 56mm from the entrance. This area extends from about 10mm from the chamber center up to 45mm. A first set of trials is conducted varying the spark axial position between 26 and 56 mm and at a radial distance from the center of the chamber of 35 mm. Because no stable combustion resulted, the injected air temperature is adjusted to the value of 463K, similar to the two-phase characterisation experiments in order to enhance fuel evaporation. In the two phase characterisation tests of chapter (5) the liquid kerosene is injected at a temperature of 290K for two configuration, high and low-flow rates, with flow rates of respectively 0.45 and 0.9 g/s. However, the value of the FAR corresponding to the high flow case is 0.068, which is far from the stoichiometric value. In order to achieve conditions suitable for combustion the fuel rate is increased to 1.7 g/s.

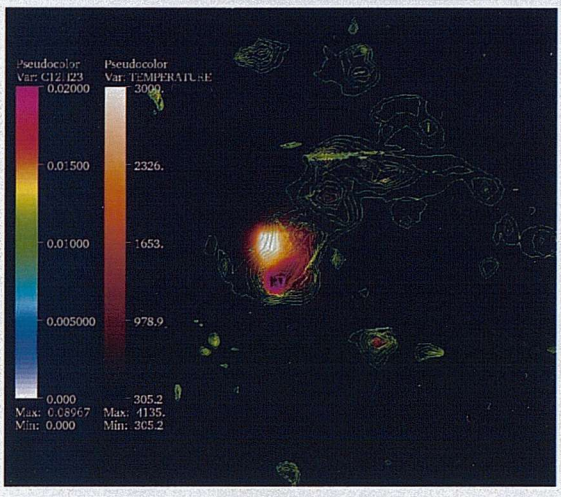


Figure 6.6: Kerosene mass fraction isosurface and Temperature contour

The application of the spark (6.6) produces a local generation of kerosene vapour due to the rapid evaporation of the liquid droplets. The fuel concentration increases significant close to the spark position and rises to the stoichiometric value, generating combustion. Because of the rapid expansion of gas in the spark core, incoming droplets are deflected and are unable to enter the spark core. Burning is observed downstream of the spark location where the hot gaseous products vaporize the kerosene droplets creating suitable conditions for combustion.

Because of this further tests are performed positioning the spark at 10mm, where the flow appears to be particularly rich in liquid fuel. In this way the spark is used to increase the vapour kerosene concentration and generate high temperatures to start the combustion process.

In the simulation of the richest test case, the presence of a flame is briefly observed. The analysis of the instantaneous quantities and the scatter plot (figure 6.7) suggests that the combustion is too lean to be stable, and the flame extinguish shortly after the end of the spark.

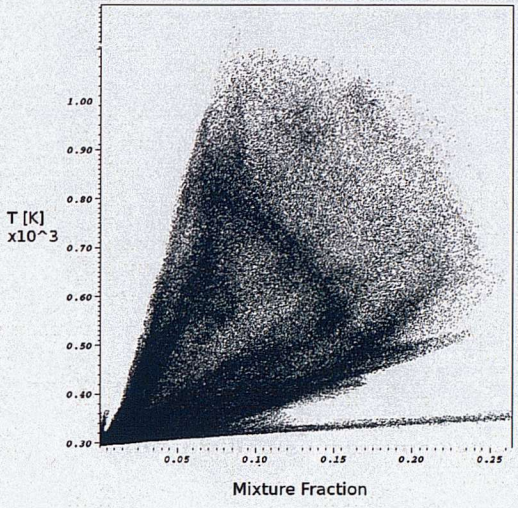


Figure 6.7: Scatter plot of kerosene mixture fraction versus temperature

The maximum temperature briefly overshoots to about 3000 K and immediately falls to a lower more physical value. However, when the spark ends the temperature decreases further showing that no stable combustion is reached. Further investigations are conducted by moving the position of the spark downstream, figure (6.9a), and close to the wall, figure (6.9b), which also resulted in failed ignition.

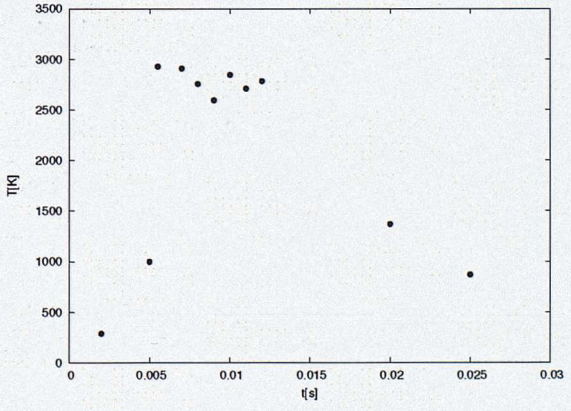
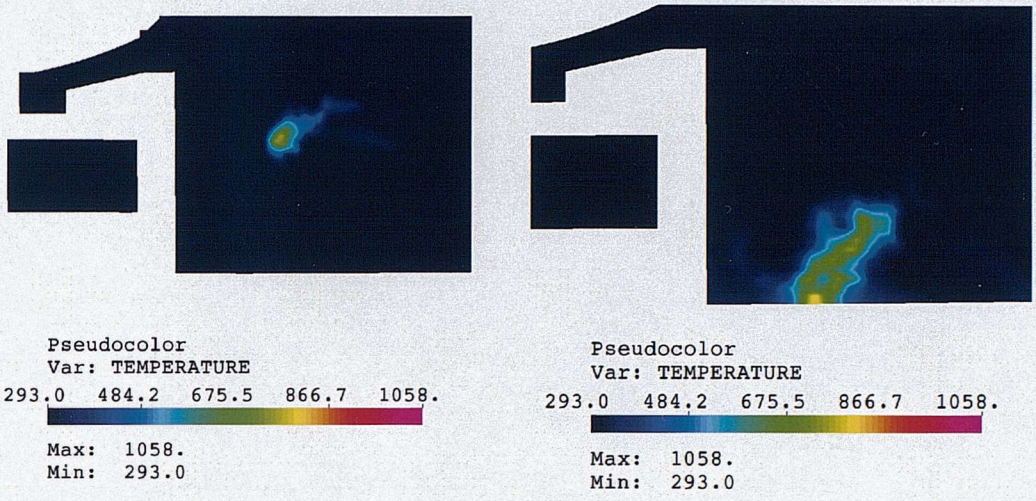


Figure 6.8: Kerosene mass fraction isosurface and Temperature contour



(a) 26mm (b) wall

Figure 6.9: Extinguishing flame after spark removal - 26 mm (a) wall (b)

6.3.2 Successful Ignition

At this point the conditions were changed in an attempt to achieve ignition and a stable flame. The mass rate was set to WR=0.201 with a kerosene flow rate of 1.8 g/s. The air temperature was 293K, consistent with experimental conditions, where a stable flame was observed with high ignition probability. According to the discussion above the spark plug position was chosen to be in a region rich in liquid kerosene. The temperature of the gas phase is lower than the previous case and the relative concentration of kerosene vapour before the spark deposition is minimal compared to that arising from the rapid evaporation of droplets in the spark core. The analysis of the liquid kerosene mass flux profiles for similar cases presented in (5.6) of chapter (5) suggests that the sections around 8mm axial distance are particularly rich in liquid fuel, as supported by observation of the simulated instantaneous liquid field and the experimental findings. The selected section is located at 10mm downstream of the chamber inlet and at a radius of 10 mm from the centre. From the images of the experimental rig a fitting hole for a spark igniter is visible at that location, suggesting that this position constitutes a realistic choice. Figure (6.10) illustrates the effects of the spark on the liquid phase.

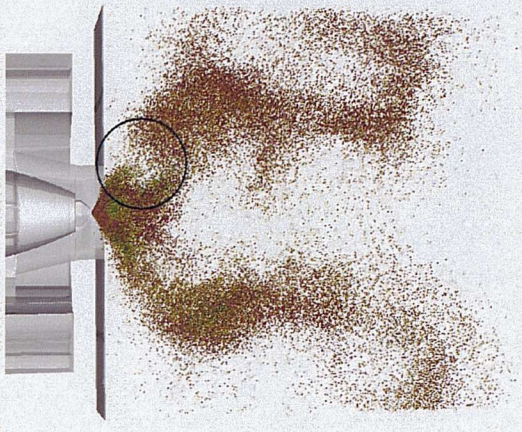


Figure 6.10: Instantaneous droplets snapshot after t=10 ms from spark deposition. The circle shows the spark location

The snapshot is taken in the plane of the spark. Droplets vaporize in the region of the spark, while the rapid expansion of gas in the spark core inhibits other droplets from entering this region, forming a sort of droplet-free space. Figure (6.11) shows the temperature contours at $t = 10ms$, when the spark intensity is at its maximum. The maximum temperature observed is close to 3000 K, hot gases are convected by the swirling motion of the flow forming a helical shape which stretches in the combustion chamber.

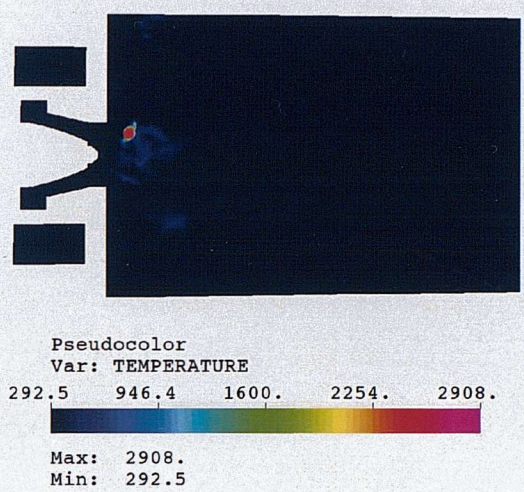


Figure 6.11: Temperature contour at t=10 ms after the spark application

After t=20 ms the spark is terminated and a small flame is observed propagating in the observation volume. The hot gaseous combustion products move downstream, enhancing the local liquid evaporation until the kerosene vapour concentrations reaches values close to stoichiometric. The flame propagates rapidly, reaching over half of the combustion chamber in 80 ms; the flame temperature appears to be relatively low compared to typical combustion cases. At t=20 ms the maximum temperature does not exceed 1500 K. This can be due to the rapid mixing effect of the swirler combined with the fact that the flame is initially located in a particularly rich region where both kerosene and air are injected at a temperature of 293K. The heat is used to evaporate the liquid fuel until the combustion is fully developed and the maximum temperature reached is around 1800 K. The high temperature region is however confined to a small region and the average temperature is around 1600 K showing that the flame temperature is on average low and the flame is close to the extinction limit. Hot pockets are visible in the center and on the sides in correspondence to the recirculation zones. There, hot gases accumulates along with droplets which evaporate forming regions where the kerosene vapour concentration is higher.

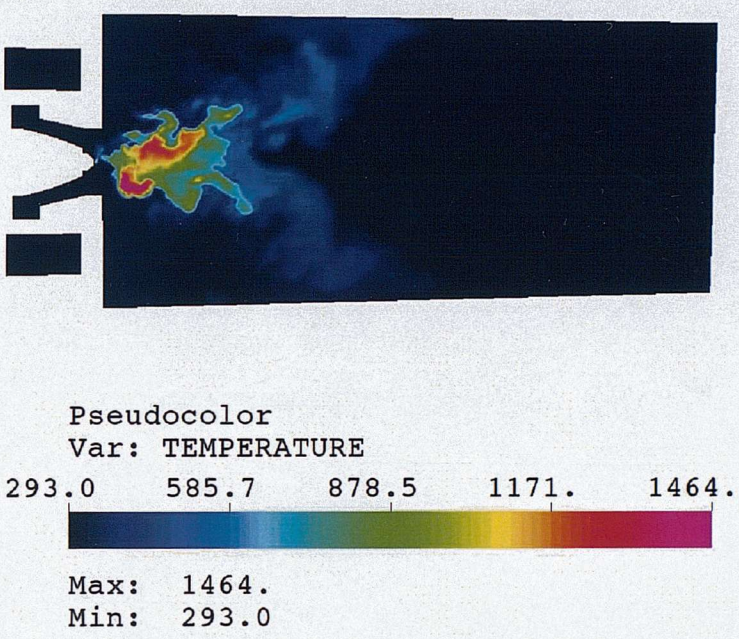


Figure 6.12: Temperature contour at t=20 ms after the spark application

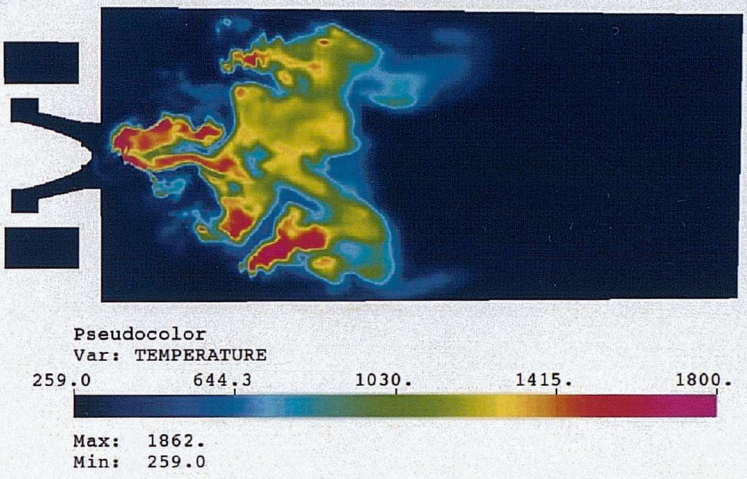


Figure 6.13: Temperature contour at t=60 ms after the spark application

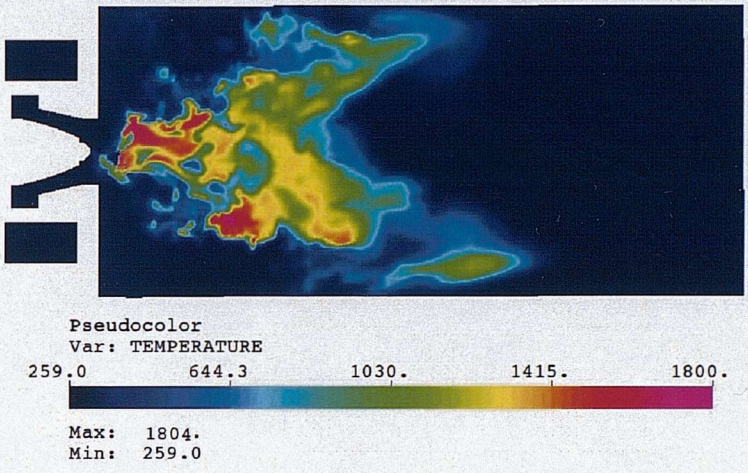


Figure 6.14: Temperature contour at t=80 ms after the spark application

The scatter plots of kerosene mixture fraction versus temperature are presented in figures (6.15)-(6.18). Again, the flame exhibits a relatively low temperature, compared to the typical value commonly found in combustion applications; the maximum mean temperature is below 1600 K. An examination of the scatter plots shows that the combustion is lean, the flame does not appear to be completely stable and is near to the extinction limit. The mean value of the temperature, mass fraction of H_2, CO_2 and H_2O along the axis of the combustor are shown in figures (6.19) to (6.20). The profiles of mean quantities are plotted in figures (6.21)-(6.25) at the same locations as was the case for the two-phase flow of the previous chapter. The mean values of the temperature, kerosene and various product mass fractions are also reported, however no comparisons are possible as no measurement of those quantities were made during the experiments.

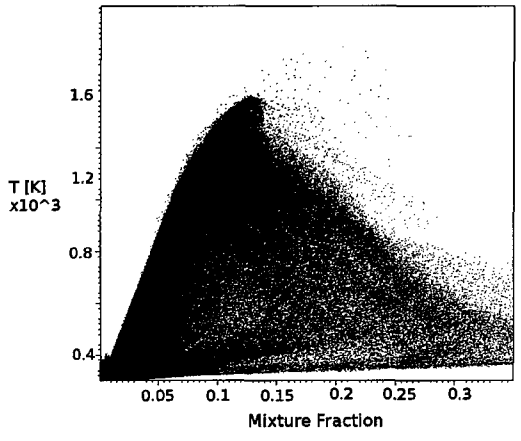
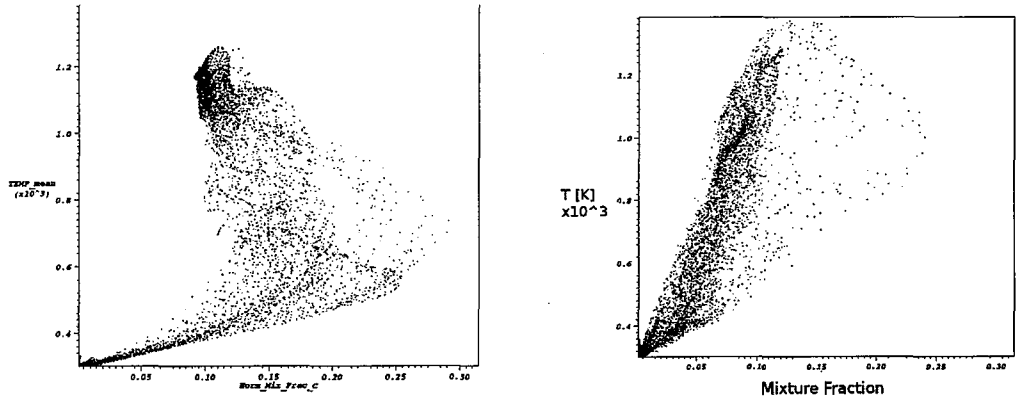
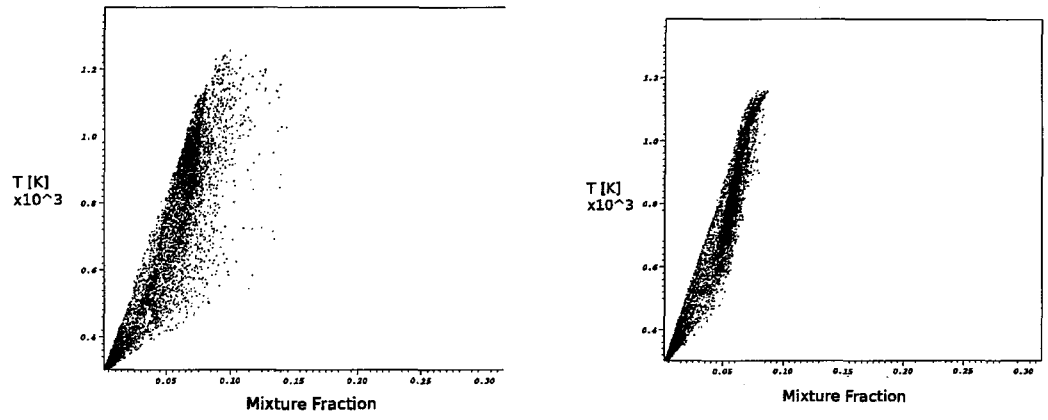


Figure 6.15: Global scatter plot of kerosene vapour mixture fraction versus temperature



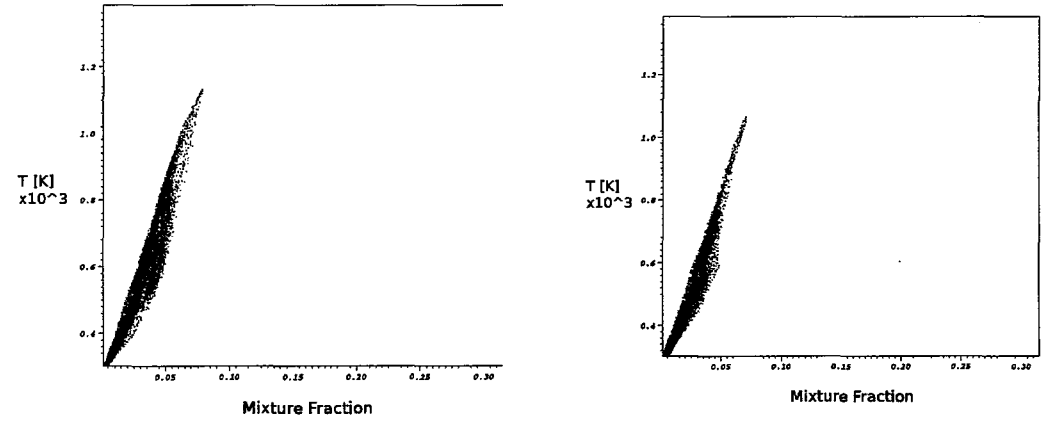
(a) 8mm (b) 26 mm

Figure 6.16: Scatter plot of kerosene vapour mixture fraction versus temperature-8mm section (a) 26mm section (b)



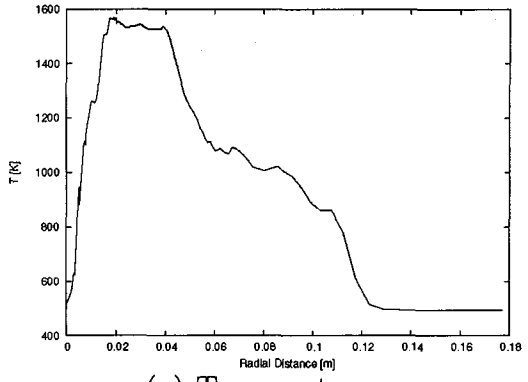
(a) 56 mm (b) 86 mm

Figure 6.17: Scatter plot of kerosene mixture fraction versus temperature- 56 mm (a) 86mm section (b)

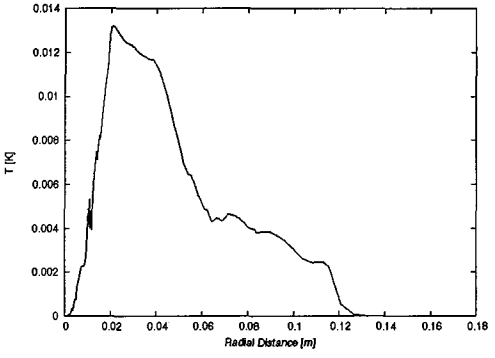


(a) 116 mm (b) 130 mm

Figure 6.18: Scatter plot of kerosene mixture fraction versus temperature- 116 mm (a) 130mm section (b)

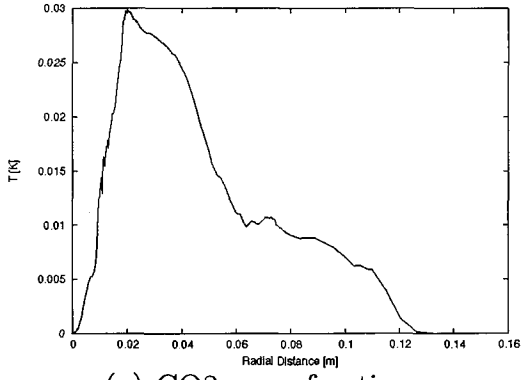


(a) Temperature

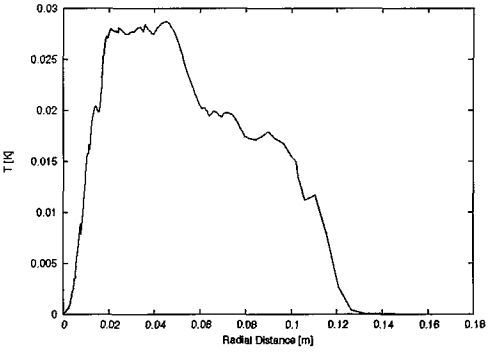


(b) H2 mass fraction

Figure 6.19: Mean temperature (a) and H2 mass fraction (b) along the axis of the combustor



(a) CO2 mass fraction



(b) H2O mass fraction

Figure 6.20: Mean CO2 mass fraction (a) and H2O mass fraction (b) along the axis of the combustor

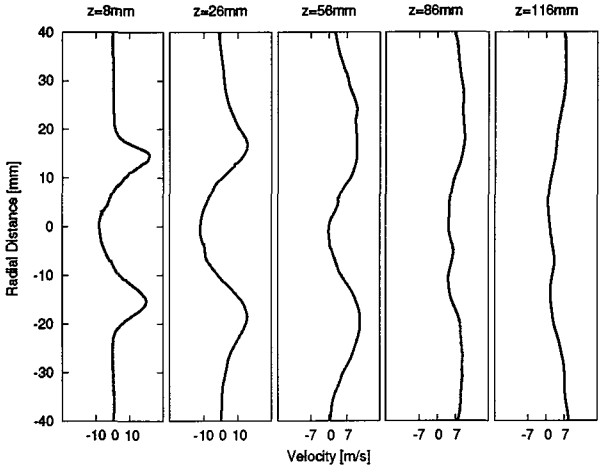


Figure 6.21: Mean axial velocity profiles

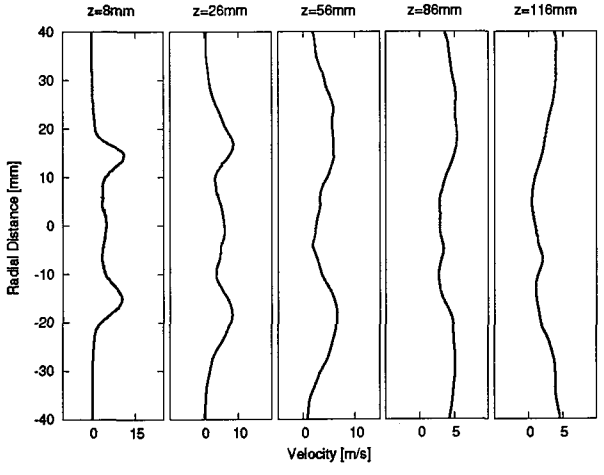


Figure 6.22: Axial velocity rms profiles

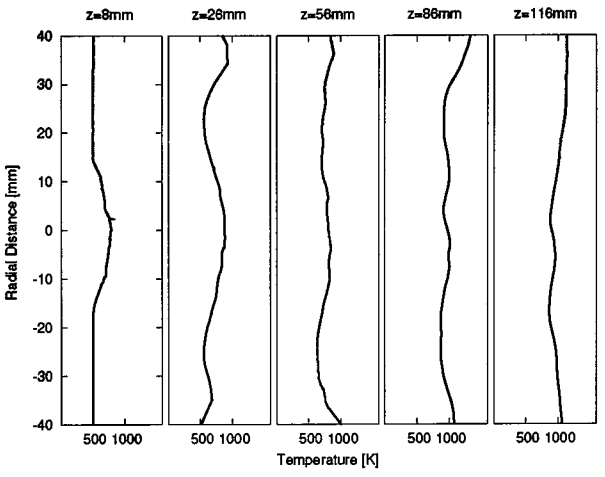


Figure 6.23: Mean temperature profiles

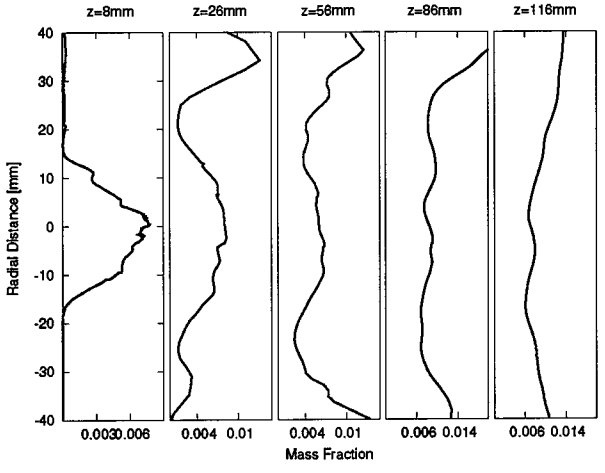


Figure 6.24: Mean CO2 mass fraction profiles

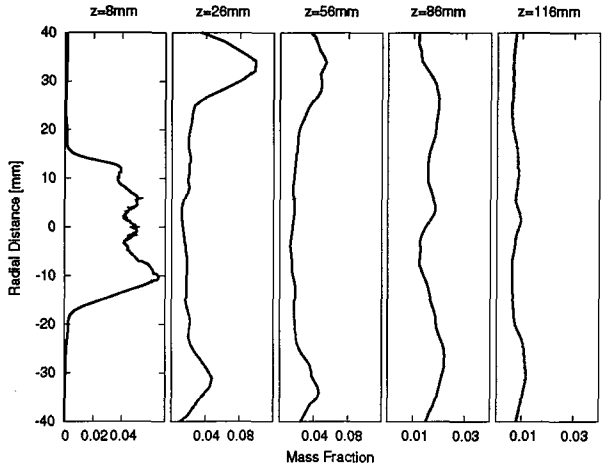


Figure 6.25: Mean kerosene mass fraction profiles

6.4 Conclusions

An investigation of the ignition of the MERCATO test bench is presented. The simulations fail to reproduce a stable flame similar to those observed during the experimental campaign. The analysis of the results of the computed temperature and the scatter plots for the unsuccessful and the successful test case clearly show that the captured combustion is lean with a flame close to extinction and whose temperature is below the values expected in typical combustion applications. This can be due to two main factors, which are explained below.

The kerosene vapour concentration in the combustion chamber plays an important role. In most of the simulations the local values of the kerosene vapour concentration are lower than the values to be found in typical combustion applications. In this regard it must be noticed that all the experiments are performed for a relatively long 'ignition time' with successful ignition occurring after 2-3 seconds in the best case scenario. During that time kerosene is continuously injected into the combustion chamber and, due to the wide injection angle, part of the fuel impinges on the side walls, creating a thin layer which covers the combustor. Indeed, in the two-phase flow studies experimentalists reported difficulties in taking measurement at high kerosene flow rates because of the window pollution.

An even higher amount of kerosene is injected in the ignition test case, where almost certainly a larger portion accumulates on the walls thus enhancing the local fuel concentration. In the experiments the igniter is sparked contineously. Though each successive spark is separated by a relatively long time interval, it is likely that this procedure has a non negligible effect on the fuel concentration in the area close to the wall. Probably the most important parameter is the spark position: in the experiments the spark is located on the wall or very close to it (protubing by around 2mm). In these circumstances the quality of the solution will strongly depend on the wall boundary conditions adopted for the gas and liquid phases.

Spray impingement becomes a predominant problem. The models used in the simulations involved droplets either sticking or bouncing on the wall. This is clearly a simplification, as spray impingement constitutes a complex phenomena which depends on many factors, such as incidence angle, droplet Weber number, droplet dimensions, incident velocity, temperature, fluid properties (i.e. viscosity and surface tension), wall temperature, surface roughness, wall film thickness and gas boundary layer characteristics in the near wall region. Depending on these factors a wide spectrum of possible droplet outcomes can arise: droplets could rebound, spread, stick, break, rebound and break, break, shatter, break because of boiling, splash or any combination of those. A study of this phenomena is beyond the scope of the present work and represents a possible idea for future investigations.

The combustor walls are presumed to be adiabatic in the simulations but this is also a source of error as the spark is likely to have an effect on the temperature of the combustor walls during the long sparking procedure.

Finally, the four step mechanism used in the simulation is probably not accurate enough to capturing all aspects of the ignition process. This problem is, however, likely to be less significant than the lack of a proper impingement model.

Because of the reasons described above, the spark was positioned inside the combustor in the simulations and this clearly influenced the final results. Possible solutions could be the implementation of spray impingement models, the development of more accurate wall functions for the gas phase as well the utilisation of a model for the thermal exchange on the wall. Considering a different test case

could be another solution. Further experiments with a smaller spray angle could reduce the effects of spray impingement and the importance of the near-wall dynamics. Several test cases are available in the literature [12, 17, 20] where the position of the spark is far from the solid boundaries and these could provide a fruitfull subject for future investigations.

Chapter 7

Conclusions and Further Works

The present work presented an investigation of the performances of the LES Eulerian-Lagrangian particle methodology for the simulation of practical aeronautical applications.
A probabilistic approach for secondary breakup of droplets is formulated and validated. The simulated droplet size distributions are compared with experiments in two typical spray configurations. At first, a single cycle of a diesel fuel injection into stagnant pressurised nitrogen is considered. This first case represents a good test of the calibration of the breakup frequencies and pdf because of its relative simplicity. The comparison of the simulated size of the droplets and spray penetration with experimental data show a reasonably good agreement. The second test case consists of mono-dispersed droplets injected into a cross flow. A range of breakup regimes, characterised by different Weber numbers, are investigated: it is found that the model is able to adapt to the different breakup mechanism, generating droplet fragments with different sizes as well as reproducing the global features of the experiment. The simulations indicate that large droplets with high momentum cross the jet whilst small droplets do not, reproducing the experimental observations. The predicted SMDs are in good local and overall agreement with measurements. The ability of the model of dynamically relating the breakup frequency, the pdf of daughter droplets, the critical diameter and the expected life of the particles to the local Weber number demonstrated that the formulation is suitable to the simulation of more complex geometries and cases, such as the

swirling stabilised burners of typical aeronautical turbine configuration.
The LES-Lagrangian particle methodology is proposed for the study of the two-phase flow in an experimental burner. The predicted profiles of the mean and *rms* velocities of the gas phase are compared with experimental data, demonstrating the efficacy of the LES. Droplets are injected into the combustor with a fixed diameter and at room temperature. The breakup constants β and C_b are adjusted in order to reproduce the injector characteristics. The liquid droplets on interaction with the turbulent structures of the shear layer of the swirled air jet, undergo fragmentation and vaporization. The good agreement of the predicted profiles of droplets size and velocities with the measured data demonstrates the effectiveness of the models implemented. Globally the physics of the two phase flow appear to be well represented: a central gas recirculation starting from the injector tip captures the droplets, which are distributed in a hollow cone pattern in the combustion chamber. The presence of a PVC is observed and the analysis of the FFT of the velocity and pressure at several probing locations demonstrate that the vortex rotation is reproduced to a good accuracy. This turbulent structure greatly influences the liquid phase by generating droplet segregation, enhancing evaporation and promoting breakup. Evidence of the latter assertion is provided by an analysis of simulations in which the PVC is not reproduced. Moreover, the relative importance of the breakup in the prediction of droplets size distribution is demonstrated by consideration of a case in which fragmentation is not simulated.
Finally, an investigation of the ignition of the MERCATO test bench is presented. The simulations do not succeed into reproducing a stable flame similar to those observed in the experiments. The analysis of the results of the predicted temperature and scatter plots for the unsuccessful and the successful test case clearly show that the captured combustion is lean with a flame close to extinction, where the temperature is below the values expected in typical combustion applications. The probable main reason for this is the relatively low simulated values of kerosene concentration in the combustion chamber. In this regard, the lack of a proper model for the impingement of kerosene on the combustor walls represents a major limitation. In the experiments the igniter was sparked for a relatively long time with a successful ignition occurring after 2-3 seconds in the

best case scenario. During that time kerosene was continuously injected into the combustion chamber and, because of the wide injection angle, part of the fuel impinged and was accumulated on the lateral walls. The global spark procedure lasted over 5 seconds with the spark located on the wall and fired over 20-30 times. The temperature of the combustor walls as well as the gas near the wall is thus not accurately represented in the simulation. A study of this wall impingement phenomena is beyond the scope of the present work, so that the spark was moved inside the combustor to achieve suitable conditions. The simulation show the potential of the code for the simulation of turbulent two-phase reacting flows. Future investigations should focus on the formulation of a reliable model of liquid impingement. Spray impingement constitutes a complex phenomena which depends on many factors, such as incidence angle, droplet Weber number, droplet dimensions, incident velocity, temperature, fluid properties (i.e. viscosity and surface tension), wall temperature, surface roughness, wall film thickness and gas boundary layer characteristics in the near wall region. Depending on these factors a wide spectrum of possible droplet outcomes can happen, which must be modelled. The relative importance of this phenomena in the prediction of combustion for modern aeronautical engines is evident [67]. Apart from that, the development of more accurate wall functions for the gas phase as well the utilisation of a model for the thermal exchange on the wall could be an interesting task. The analysis of a different test case in which impingement is not relevant could represent another solution. For what concerns droplets breakup, future work could investigate the possibility of connecting the breakup constants used for the breakup frequency and pdf of the generated particles size to flowfield parameters, such as the turbulent kinetic energy, the rate of dissipation of kinetic energy and the Weber number. In this way the problem of defining values of the model constants would be avoided. Regarding the gas phase results, even though the simulated gas profiles shown good agreement with the experimental data, slightly more accurate predictions might arise if a dynamic Smagorinsky model were to be used. Improvement to the simulations of the liquid phase could be achieved if the injector specifications were known. In this regard the choice of a test case with more detailed information on the injector could represent a good propose for further investigations.

Appendix A

Stochastic Review

Appendix A presents a brief review of the stochastic theory necessary to understand the model adopted. A more complete and formal explanation can be found in references [25].

A stochastic differential equation can be defined as a differential equation in which some randomness is present in its coefficients. Let N be for instance the number of particles of a certain diameter. The following simple population growth model can be considered:

$$\frac{dN}{dt} = c(t)N(t) \quad N(0) = N_0(constant) \tag{A.1}$$

where N(t) is the size of the population at time t, and c(t) is the relative rate of growth. It might happen that c(t) is not completely deterministic but subject to some sort of uncertain noise: $c(t) = r(t)$"$noise$". The exact behaviour of the noise term can be unknown, and just the probability distribution defined. The solution of this type of equation can be obtained by rewriting it into the form:

$$\frac{dX}{dt} = a(t, X_t) + b(t, X_t) \cdot \text{"}noise\text{"} \tag{A.2}$$

with a and b given functions. Considering for example a 1-dimensional case, it is reasonable to look for some stochastic process W_t which represents the noise term, and rewrite the equation as

$$\frac{dX}{dt} = a(t, X_t) + b(t, X_t) \cdot W_t \tag{A.3}$$

where W_t satisfies the following properties: if $t_1 \neq t_2 \Rightarrow W_{t_1}$ and W_{t_2} are independent, $\{W_t\}$ is stationary (the joint distribution $\{W_{t_1+t}, ..., W_{t_k+t}\}$ does not depend on t) and $E[W_t] = 0$ for all t. In the equation A.3, the noise term does not exhibit continuity of path and, therefore, is usually written in the integral form:

$$dX_t = a(t, X_t)dt + b(t, X_t)dW_t \tag{A.4}$$

where the only process satisfying the properties of W_t and also continuity of the path over finite intervals is a Brownian motion (also known as a Wiener Process). An example of Brownian motion is the motion experienced by a suspended particle in water. The motion is due to the frequent and, from a macroscopic point of view, random impacts of water molecules with the particle. The mathematical expression of a Brownian motion is the Markovian process W_t. A Markovian process is defined as a process which has $W_{t=0} = 0$, independent increments and $W_{t+s} - W_t$ normally distributed with mean 0 and variance s:

$$p[(W_{t+s} - W_t) = x] = \frac{1}{\sqrt{2\pi s}} e^{-\frac{x^2}{2s}} \tag{A.5}$$

which resembles the Markov assumption for what the value of the function in the future time does not depend on the past values, but just on the present. Brownian motion is an ideal approach to adopt for the problem of particle dynamics when LES is adopted for continuous phase. Similarly to the particle suspended in water whose dynamics are affected by a certain macroscopic motion of water and a random-like component due to the molecular impacts, the motion of a droplet in a flow solved with LES will experience a deterministic component arising from the filtered term, and a "unknown" filtered component due to the small unresolved continuous phase small scale motions. A widely accepted form for the particle dispersion equation is the following:

$$\frac{d\overrightarrow{V_t}}{dt} = \frac{\overrightarrow{U(t)} - \overrightarrow{V_t}}{\tau_I} \tag{A.6}$$

where V_t is the particle velocity, $U(t)$ is the flow velocity at the particle position and τ_I is a time dimensioned term representing the inertial effects and taking into account the mutual force between the particle and the fluid. In LES the velocity

of the flow can be divided into the filtered $\bar{U}(t)$ and the velocity fluctuations $u(t)$ as $U(t) = \bar{U}(t) + u(t)$. By using this expression in A.6 it is possible to write:

$$dV_t = \tau_I^{-1} \left(\bar{U}(t) + u(t) - V_t \right) dt \tag{A.7}$$

where the term τ_I is called particle relaxation time and is defined as the rate of response of particle acceleration to the relative velocity between the particle and the fluid. It can be expressed as a function of the flow density ρ_f, the particle densityρ_p , radius R and drag coefficient C_D. For general flows:

$$\tau_I^{-1} = \frac{3}{8} \frac{\rho_f C_D}{\rho_p R} \| U(t) - V_t \| \tag{A.8}$$

As already noticed in A.7 the local velocity fluctuations are unknown and the modelling assumption consists of introducing a stochastic Markovian model. It is possible to write the equation in term of Wiener process as showed in [7]:

$$dV_i^t = {\tau_p}^{-1} \left(\widetilde{U}^{(i)}(t) - V_t^{(i)} \right) dt + \mathbf{B} d\mathbf{B}_t \tag{A.9}$$

where B_t is a Brownian motion and B is the diffusion coefficient matrix. The following expression for the diffusion coefficient is adopted in the present work:

$$dV_i^t = {\tau_p}^{-1} \left(\widetilde{U}^{(i)}(t) - V_t^{(i)} \right) dt + C_o \sqrt{k_{sgs} \left(\tau_p^{-1} \right)} d\mathbf{W}_t \tag{A.10}$$

For the numerical simulation of equation A.10 the Euler approximation is one of the simplest time discrete approximations of an Ito process. It is a strong approximation scheme and can be written as:

$$x_{n+1} = x_n + a(x_n)\Delta_n + b(x_n)\Delta W_n \tag{A.11}$$

where $\Delta_n = t_{n+1} - t_n$ and $\Delta W_n = W_{t_{n+1}} - W_{t_n}$. The time discretization of SDE is similar to ODE discretisation. Another more accurate scheme is that of Milstein:

$$x_{n+1} = x_n + a(x_n)\Delta_n + b(x_n)\Delta W_n + b(x_n)b'(x_n)(\Delta W_n^2 - \Delta_n) \tag{A.12}$$

and higher order schemes can be also formulated, however this is only applicable to simple Ito diffusion, while the considered problem includes a jump-diffusion process. The jump part of the SDE, in a scalar case $dx = a(x)dt + b(x)dW_t +$

$A(x)\delta N_t$, is discretised in an heuristic manner [7]: $A(x_n)\Delta N_n$ where ΔN_n is the variation in the number of occurrences of the underlying counting process between t_n and t_{n+1}. The problem is solved with a fractional steps method, where the time step is divided in sub-steps and only one variable is allowed to vary per time.

Appendix B

Random Variate Generation

This appendix introduces the fundamental principles in non-uniform random variate generation as reported in [18]. The two methods presented, the inverse trasformate sampling and the acceptance-rejection method, are often used in practical applications for random number generation.

The Inverse transformate Sampling or "inversion method" is a non-uniform random variate generation method which allows the generation of random numbers with a well defined probability distribution function (PDF), given its cumulative distribution function F (CDF). The inversion method is the only truly universal method: it allows to generate a random variate with distribution F without any additional information but the distribution itself. The method is based upon the following property:
Let F be a continuous distribution on R with inverse F^{-1} defined by

$$F^{-1}(u) = inf\{x : F(x) = u, 0 < u < 1\} \tag{B.1}$$

If U is a uniform $[0,1]$ random variable, then $F^{-1}(U)$ has a distribution function F. Also, if X has distribution function F , then $F(X)$ is uniformly distributed on [0,1]. The proof of the first statement follows after pointing out that for all $x \in R$:

$$P(F^{-1}(x) \leq x) \stackrel{\text{def}}{=} P(inf\{y : F(y) = U\} \leq x) = P(U \leq F(x)) = F(x) \tag{B.2}$$

being the cumulative distribution function F monotonic on both sides and U uniform on the unit interval. Also:

$$P(F(x) \leq u) = P(X \leq F^{-1}(u)) = F(F^{-1}u) = u \tag{B.3}$$

Equation B.2 states that if X is a continuous random variable, with cumulative distribution function F, and if $Y = F(X)$, then Y has a uniform distribution on [0, 1]. The inverse of this function is the inverse probability integral transform. Indeed, if Y has a uniform distribution on [0, 1] and if X is defined as $X = F^{-1}(Y)$, then X has cumulative distribution function F. Following the previous statements a random number can be generated with a well defined PDF f and only knowing this, the F can be computed integrating f. Therefore, from the inverse of the cumulative distribution function, F^{-1}, a number can be generated. Fortran can provide various simple methods of generating pseudo-random numbers u_{random} which are effectively distributed according to a standard uniform distribution. The corresponding value $x^* = F^{-1}(u_{random})$ is the desired value.
The Rejection method is often applied to generate random numbers with a well defined distribution and within certain constraints. An example could be the injection of droplets with a defined number distribution (e.g. Rosin Rammler) but within the limits and constraints (size and velocity) dictated by the specific test case considered, and according to the experimental data available.

Appendix C

Basics of spray characterization

Some means of describing quantitative information of droplet distribution is necessary in order to evaluate and compare spray characteristics. A possible solution is defining a PDF of the drop size: the set of droplets of different sizes produced by spray atomisation can be divided into classes, where each class consists of the ensemble of droplets of a given diameter D in the range $[D - \Delta D, D + \Delta D]$. A histogram of the frequency of occurrence of a given class can be defined by counting the number of elements in each of the defined classes. The continuous version of such a histogram ($\lim_{\Delta D \to 0}$) represents the PDF of the droplet or "number distribution". In the same way, it is possible to construct area or volume distributions, where the area or the volume of the droplets are the variables of interest. The velocity distribution can be defined in a similar manner, with droplets size and velocity distribution completely characterizing a given spray. Even though in reality droplets size distribution are limited functions, bounded by a minimum and maximum diamter, it is convenient to assume droplets distributions as ranging from zero to infinity with:

$$\lim_{D \to 0} \int_0^D f(D) dD = 0 \tag{C.1}$$

$$\lim_{D \to 0} \int_D^\infty f(D) dD = 1 \tag{C.2}$$

The PDF must satisfy the following properties:

$$f(D) \geq 0 \tag{C.3}$$

$$\int_0^\infty f(D)dD = 1 \tag{C.4}$$

Moments of a drop size distribution can be calculated as follows:

$$M_n = \int_0^\infty D^n f(D)dD \tag{C.5}$$

In many calculations for mass and flow processes it is more convenient to work with average diameters, instead of using a complete drop size distribution. In this way the caracterization of a particular droplet size distribution is achieved by means of a single number or 'representative droplet diameter'. This concept of diameter has been standardized by [51], and can be expressed in a general formulation as:

$$(D_{pq})^{p-q} = \left[\frac{\int_0^\infty D^p f(D)dD}{\int_0^\infty D^q f(D)dD}\right]^{1/(p-q)} \tag{C.6}$$

where p and q are typicall positive integrs, but fractional and negative mean diameters are not excluded [5]. The expression of the mean diameter can be also written as:

$$D_{pq} = \left[\frac{\Sigma N_i D_i^p}{\Sigma N_i D_i^q}\right]^{1/(p-q)} \tag{C.7}$$

Some of the most common mean diameters are reported below.

The arithmetic mean diameter D_{10}, or mean number distribution represents the linear average value of all droplets in a given spray. It can be defined as:

$$D_{10} = \frac{\int_0^\infty Df(D)dD}{\int_0^\infty f(D)dD} \tag{C.8}$$

The Sauter Mean Diameter D_{32} or mean of the area distribution is used to define mass transfer and is very valuable in applications related to combustion

and reactions as it provide a measure of the mass of liquid transfered. It can be defined as:

$$D_{32} = \frac{\int_0^\infty D^3 f(D) dD}{\int_0^\infty D^2 f(D) dD} \tag{C.9}$$

Other significative diameters are the volume mean diameter D_{30}, used in hydrology for volume controlling, the mean volume distribution D_{43}, important for combustion equilibrium and the surface mean diameter D_{20}.

Appendix D

Large Eddy Simulation of complex geometries

Large-scale applications in computational fluid mechanics are generally very demanding in terms of computational resources. The need of achieving solution in reasonable time is addressed by mean of parallel processing. This process consists into splitting the computational domain in several sub-domains or blocks and solving them independently with different processors. Inter-domain exchanges are implemented via Message Passing Interface (MPI) routines and guarantees the continuity of the solution, so that information is communicated between the neighbor domains.

Although this procedure permits to significantly speed up the simulation, its implementation requires special attention when dealing with complex geometries. The conventional method used for parallel computing of Eulerian based CFD applications adopts halo cells which overlap between neighbor domains as shown in Figure (D.1). The picture shows the exchanges for a simple bi-dimensional case with the overlapping or *"halo"* cells clearly displayed. The halo cells keep the information necessary for the domain to compute derivatives: the solution of each domain is calculated separately and information is written into these exchanging cells so that the neighbor domains have the quantities they need to compute the solution. All the scalars (temperature, energy and species), velocities and

pressure are exchanged between domains; numerical structures such as the TVD schemes which require more information might use 2 or more rows of halo cells.

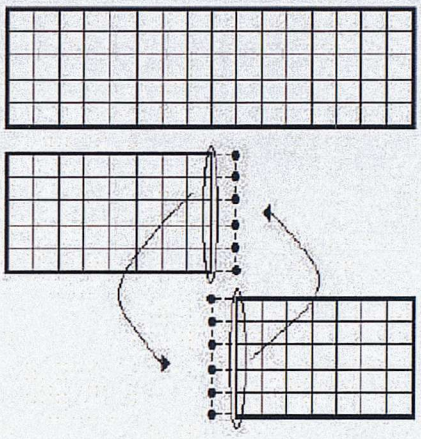


Figure D.1: Basic scheme of halo cells for the left-side sub-domain

The exchanging of information between domains can become difficult in complex multi-domain geometries such as the one used for the simulation of the MERCATO test case. Figure D.2 shows a typical situation when several domains share one of the corners. In this case the information required by one domain for the solution of the flowfield might demand the knowledge of the information in the corner of the opposite domain. Geometrical parameters, scalars quantities and velocities must be somehow exchanged between these domains. Additional complexity is encountered in 3D when the flipping of the computational directions of the domains makes the identifications of the neighbor corners very difficult. In the present work a hybrid node and vertex structure is adopted. The information of the vertex based structure is used whenever the interpolation scheme requires the values in one of the external corners. Detailed information on numerical aspects can be found in [40, 57].

The parallelisation of the Lagrangian tracked dispersed phase is solved simultaneously with the Eulerian and particles are exchanged between domains in the same way as the continuous variables.

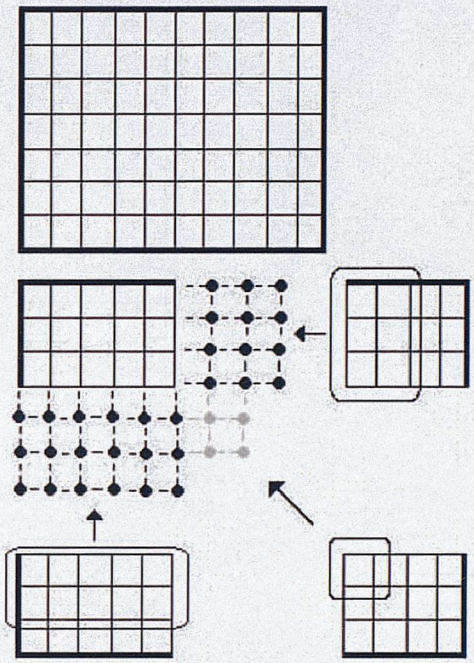


Figure D.2: Basic scheme of halo cells in a multi-domain configuration

References

[1] B. Abramzon and W.A. Sirignano. Droplet vaporization models for spray combustion calculations. *Int. J. Heat Mass Transfer*, 32:1605–1618, 1989. 50

[2] J.D. Anderson. *Computational Fluid Dynamics - The Basics with Applications.* Mc-Grawn-Hill, 1995. 28

[3] S.V. Apte, M. A. Gorokhovski, and P. Moin. Les of atomizing spray with stochastic modeling of secondary breakup. *Int. J. Multiphase Flow*, 29:1503–1522, 2003. 53, 67, 81, 82

[4] S.V. Apte, K. Mahesh, P. Moin, and J.C. Oefelein. Large-eddy simulation of swirling particle-laden flows in a coaxial-jet combustor. *International Journal of Multiphase Flow*, 29:1311–1331, 2003. 25

[5] E. Babinsky and P.E. Sojka. Modeling drop size distributions. *Prog. Energy Combust. Sci.*, 28:303–329, 2002. 64, 77, 192

[6] L. Bayvel and Z. Orzechowski. Liquid atomization. *Taylor and Francis, London*, 1993. 54, 144

[7] M. Bini. *Large eddy simulation of particle and droplet laden flows with stochastic modelling of subfilter scales.* PhD thesis, Imperial College London, 2007. 40, 43, 44, 48, 52, 76, 187, 188

[8] M. Bini and W. P. Jones. Particle acceleration in turbulent flows: A class of nonlinear stochastic models for intermittency. *Phys. Fluids*, 19:035104, 2007. 47

[9] M. Bini and W. P. Jones. Large eddy simulation of particle laden turbulent flows. *J Fluid Mech.*, 614:207–252, 2008. 43, 46, 47

[10] M. Bini and W.P. Jones. Large eddy simulation of an evaporating acetone spray. *International Journal of Heat and Fluid Flow*, 30:471–480, 2009. 43, 46

[11] N. Branley and W. P. Jones. Large Eddy Simulation of a Turbulent Non-premixed Swirling Flame. In W. Rodi, editor, *4th International Symposium on Engineering Turbulence Modelling and Measurements*, pages 861–870, Corsica, France, May 1999.

[12] N. Branley and W. P. Jones. Large Eddy Simulation of a Turbulent Non-premixed Flame. *Combustion and Flame*, 127:1914–1934, 2001. 181

[13] P. Burattini, R.A. Antonia, S.Rajagopalan, and M. Stephens. Effect of initial conditions on the near-field development of a round jet. *Experiments in Fluids, 37*, page 5664, 2004. 86

[14] B. Chehroudi, Y. Onuma, S. Chen, and F.V. Bracco. On the intact core of full cone sprays. *SAE Paper*, page 850126, 1985. 56

[15] C.A. Coulaloglou and L.L. Tavlarides. Description of interaction processes in agitated liquid liquid dispersions. *Chem. Eng. Sci.*, pages 32,12891297, 1977. 68, 69

[16] E.L. Crow and K. Shimizu. Lognormal distributions: theory and applications. *New York:Marcel Dekker*, 1998. 64

[17] P. Dagaut and M. Cathonnet. The ignition, oxidation, and combustionnext term of kerosene: A review of previous termexperimentalnext term and kinetic modeling. *Progress in Energy and Combustion Science*, pages 32,48–92, 2006. 181

[18] L. Devroye. *Non-Uniform Random Variate Generation.* New York: Springer-Verlag, 1986. 189

[19] John K. Dukowicz. A particle-fluid numerical model for liquid sprays. *J. Comp. Phys.*, 35:229–253, 1978. 63

[20] I. Dwel, H.-W. Ge, H. Kronemayer, R. Dibble, E. Gutheil, C. Schulz, and J. Wolfrum. Experimental and numerical characterization of a turbulent spray flame. *Proceedings of the Combustion Institute*, pages 31,2247–2255, 2006. 181

[21] G. M. Faeth, L. P. Hsiang, and P. K. Wu. Structure and breakup properties of sprays. *Int. J. Multiphase Flow*, 21, suppl.:99–127, 1995. 16, 62

[22] G. M. Faeth, L. P. Hsiang, and P. K. Wu. Structure and breakup properties of sprays. *Int. J. Multiphase Flow*, 21:99–127, 1995. 56, 59, 60, 69

[23] G.M. Faeth. Current status of droplet and liquid combustion. *Prog. Energy Combust. Sci.*, 1977. 50

[24] T. Galloway and B. Sage. Thermal and material transfer in turbulent gas steams - a method of prediction for spheres. *Int. J. Heat Mass Trans.*, pages 7:283–291, 1964. 50

[25] C. W. Gardiner. *Handbook of Stochastic Methods. For Physics, Chemistry and the Natural Science.* Springer, 1983. 44, 45, 46, 76, 185

[26] S. Ghosal, T. S. Lund, P. Moin, and K. Akselvoll. A dynamic localization model for large eddy simulation of turbulent flows. *J. of Fluid. Mech*, page 286:229255, 1995. 39

[27] Batchelor G.K. *An Introduction to Fluid Dynamics.* Cambridge University Press, 1967. 28, 70

[28] M. A. Gorokhovski and V. L. Saveliev. Analyses of kolmogorov's model of breakup and its application into Lagrangian computation of liquid sprays under air-blast atomization. *Phys. Fluids*, pages 184,192, 2002. 45, 64, 67

[29] A. D. Gosman and D. Clerides. Diesel spray modelling: A review. In *Proceedings of the International Conference on Liquid Atomization and Spray Systems-ILASS Europe*, July 1998. Florence, Italy. 64

[30] M.G Hall. Vortex breakdown. *Ann. Rev.Fluid Mech 4 (1)*, pages 195–218, 1972. 137

[31] G. Haller. An objective definition of a vortex. *J. Fluid Mech. (2005), vol. 525, pp. .*, pages 525,126, 2005. 136

[32] M. Herrmann. Detailed numerical simulations of the primary atomization of a turbulent liquid jet in crossflow. *In American Physical Society*, pages 23–25, 2008. 80

[33] M. Herrmann. Detailed simulations of the breakup processes of turbulent liquid jets in subsonic crossflows. *In 11th Triennial International Conference on Liquid Atomization and Spray Systems*, page 188, 2009. 80

[34] H. Hiroyasu and T. Kadota. Fuel droplet size distribution in diesel combustion chamber. Technical report, University of Hiroshima, 1976. 53, 80

[35] C.W. Hirt, A.A. Amsden, and J.L. Cook. Arbitrary Lagrangian Eulerian computing method for all flow speeds. *Journal of Computational Physics*, pages 14, 227253, 1974. 63

[36] L.P. Hsiang and G. M. Faeth. Near-limit drop deformation and secondary breakup. *Int. J. Multiphase Flow*, 18:635–652, 1992. 61, 63

[37] L.P. Hsiang and G. M. Faeth. Drop properties after secondary breakup. *Int. J. Multiphase Flow*, 19:721–735, 1993. 60

[38] G. L. Hubbard, V. E. Denny, and A. F. Mills. Droplet evaporation: effects of transients and variable properties. *Int. J. Heat and Mass Transfer 18(9)*, page 1003 1008, 1975. 51

[39] Felix Jaegle. *Large eddy simulation of evaporating sprays in complex geometries using Eulerian and Lagrangian methods.* PhD thesis, Institut National Polytechnique de Toulouse, 2009. 16, 24, 35, 36, 48, 63

[40] W. P. Jones, F. di Mare, and A. J. Marquis. Les-Boffin: Users guide. Technical memorandum, Imperial College, London, 2002. 40, 195

[41] W. P. Jones, S. Lyra, and A. J. Marquis. Large eddy simulation of evaporating kerosene and acetone sprays. *Int. J. Heat Mass Trans.*, 53:2491–2505, 2010. 46, 51

[42] W.P. Jones and D. Sheen. A probability density function method for modelling liquid fuel sprays. *Flow, Turbulence and Combustion*, 63:379–394, 1999. 43

[43] J. Keays. *Large eddy simulation of premixed combustion.* PhD thesis, Imperial College London, 2006. 34

[44] A.N. Kolmogorov. A refinement of previous hypotheses concerning the local structure of turbulence in a viscous incompressible fluid at high Reynolds number. *J. Fluid Mech.*, pages 13–82, 1962. 34

[45] Seok Jae Kwon and Il Won Seo. Reynolds number effects on the behavior of a non-buoyant round jet. *Experiments in Fluids, 38*, page 801812, 2005. 86

[46] G. Lacaze, E. Richardson, and T. Poinsot. Large eddy simulation of spark ignition in a turbulent methane jet. *Combust. Flame 156 (10)*, page 19932009, 2009. 160, 161

[47] J.C. Lasheras, C. Eastwood, C. C. Mart'inez-Baz'an, and J.L. Montanes. A review of statistical models for the break-up of an immiscible fluid immersed into a fully developed turbulent flow. *Int. J. Multiphase Flow*, 28:247–278, 2002. 66, 69, 71, 77, 78

[48] R. Lecourt, G. Heid, and M. Zedda. Ignition and extinction results at ambient conditions. Report, ONERA, 2008. 110, 162

[49] R. Lecourt and M. Zedda. Injection system two-phase flow characterisation (LDA-PDA). Report, ONERA, 2008. 106, 110, 112, 137, 138, 139

[50] C. H. Lee and Rolf D. Reitz. An experimental study of the effect of gas density on the distortion and breakup mechanism of drops in high speed gas stream. *Int. J. Multiphase Flow*, 26:229–244, 2000. 62, 63

[51] A. H. Lefebvre. *Atomization and Sprays.* Hemisphere Publishing Corporation, 1989. 54, 58, 61, 88, 192

[52] S. Leibovich. Vortex stability and breakdown: Survey and extension. *AIAA Journal*, page 22(9):11921206, 1984. 137

[53] P.A. Libby and F.A. Williams. *Computational Fluid Dynamics.* Springer-Verlag, 1994. 28

[54] D. K. Lilly. A proposed modification of the germano subgrid-scale closure method. *Physics of Fluids*, pages 4:633–635, 1992. 39

[55] Hai-Feng Liu, Xin Gong, Wei-Feng Li, Fu-Chen Wang, and Zun-Hong Yu. Prediction of droplet size distribution in sprays of prefilming air-blast atomizers. *Chem. Eng. Sci.*, 61:1741–1747, 2006. 67

[56] Z. Liu and R. D. Reitz. An analysis of the distortion and breakup mechanisms of high speed liquid drops. *Int. J. Multiphase Flow*, 23(4):631–650, 1997. 63

[57] F. Di Mare. *Large Eddy Simulation of reacting and non-reacting flows in complex geometries.* PhD thesis, Imperial College, University of London, UK, 2002. 195

[58] C. Mart'inez-Baz'an, J.L. Montanes, and J.C. Lasheras. On the break-up of an air bubble injected into fully developed turbulent flow. Part I:Breakup frequency. *J.Fluid Mech.*, 401:157–182, 1999. 66, 69, 70

[59] C. Mart'inez-Baz'an, J.L. Montanes, and J.C. Lasheras. On the break-up of an air bubble injected into fully developed turbulent flow. Part II:Size pdf of the resulting daughter bubbles. *J.Fluid Mech.*, 401:183–207, 1999. 66, 69, 70

[60] M.Germano, U.Piomelli, Moin P., and W.H. Cabot. A dynamic sub-grid-scale eddy viscosity model. *Physics of Fluids*, pages 23:1760–1765, 1986. 39

[61] R.S. Miller, K. Harsted, and J. Bellan. Evaluation of equilibrium and non-equilibrium evaporation models for many-droplets gas-liquid flow simulations. *International Journal of Multiphase Flows*, 24:1025–1055, 1998. 49, 51

[62] A. Mostafa and M. Mongia. On the modeling of turbulent evaporating sprays: Eulerian versus Lagrangian approach. *International Journal of Heat and Mass Transfer*, 30(12):2583–2593, 1987. 43

[63] Manuel Garcia Villalba Navaridas. *Large eddy simulation of turbulent swirling jet.* PhD thesis, Karlshucle University, 2006. 136

[64] P. J. O'Rourke and A. A. Amsden. The TAB method for numerical calculations of spray droplet breakup. SAE Technical Paper 87-2089, 1987. 64, 69

[65] Sung Wook Park, Sayop Kim, and Chang Sik Lee. Breakup and atomization characteristics of mono-dispersed diesel droplets in a cross-ow air stream. *Int. J. Multiphase Flow*, 32:807–822, 2006. 53, 61, 62, 84, 86, 94, 100, 101

[66] M. Pilch and C. Erdman. Use of breakup time data and velocity history data to predict the maximum size of stable fragments for acceleration-induced breakup of a liquid drop. *Int. J. Multiphase Flow*, 13:741–757, 1987. 62, 63

[67] T. Poinsot, G.Staffelbach, M.Boileau, and P. Wolf. Using LES to study reacting flows and instabilities in annular combustion chabers. *ETMM8 Proceeding*, pages 301–316, 2010. 184

[68] S.B. Pope. *Turbulent Flows.* Cambridge University Press, 2000. 28, 33, 34

[69] M. Rachner, J. Becker, C. Hassa, and T. Doerr. Modelling of the atomization of a plain liquid fuel jet in crossflow at gas turbine conditions. *Aerospace Science and Technology*, pages 495–506, 2002. 81

[70] J. Réveillon and L. Vervisch. Eulerian analysis of the dispersion of evaporating polydispersed sprays in a statistically stationary turbulent flow. *Journal of Turbulence*, pages 1–27, 2000. 43

[71] J. Réveillon and L. Vervisch. Spray vaporization in non-premixed turbulent combustion modelling: A single drop model. *Combustion and Flame*, 121:75–90, 2000. 43

[72] A.A. Abdel Rahman, W.Chakroun, and S.F. Al-Fahed. LDA measurements in the turbulent round jet. *Experiments in Fluids*, page 801812, 1997. 86

[73] Doraiswami Ramkrishna. *Population Balances.* Academic Press, 2000. 68, 69

[74] R. D. Reitz. Modeling atomization processes in high-pressure vaporizing sprays. *Atomization and Spray Tech*, 3:309–337, 1987. 64

[75] R.D. Reitz and F.V.Bracco. Mechanism of atomization of a liquid jet. *Phys. Fluids*, 25:1730–1742, 1982. 60, 64

[76] S. Rigopoulos. Population balance modelling of polydispersed particles in reactive flows. *Prog. Energy Combust. Sci.*, 2010. doi:10.1016/j.pecs.2009.12.001. 69

[77] R.Lecourt. Ignition and extinction results at ambient conditions. Technical report d2.2.1c timecop-ae, ONERA, 2008. 164

[78] S. Roux, G. Lartigue, T. Poinsot, U. Meier, and C. B rat. Studies of mean and unsteady flow in a swirled combustor using experiments, acoustic analysis and large eddy simulations. *Combust. Flame 141 (10)*, pages 40–54, 2005. 137

[79] Mirko Salewski and Laszlo Fuchs. Consistency issues of lagrangian particle tracking applied to a spray jet in crossflow. *Int. J. of Multiphase Flow*, pages 33–4, 394–410, 2007. 25, 35, 43

[80] M. Sanjose. *Evaluation de la methode Euler-Euler pour la simulation numrique aux grandes chelles des chambres carburant liquide.* PhD thesis, Institut National Polytechnique de Toulouse, 2009. 155

[81] M. Sanjose, T. Lederlin, L. Gicquelt, B. Cuenott, H. Pitscht, N. Garcia-Rosa, R. Lecourt, and T. Poinsot. LES of two-phase reacting flows. *Center for Turbulence Research Proceedings of the Summer Program*, 2008. 155

[82] Viriato Semio, Pedro Andrade, and Maria DE Graca Carvalho. Spray characterization: numerical prediction of sauter mean diameter and droplet size distribution. *Fuel*, 75(15):1707–1714, 1996. 65, 77

[83] J-.M. Senoner. Large eddy simulation of two-phase-flows using a euler-lagrange approach with secondary breakup. *PhD thesis, University of Toulouse*, 2010. 81

[84] W.A. Sirignano. *Fluid Dynamics and Transport of Droplets and Sprays.* Cambridge University Press, 1999. 43, 48, 50, 52

[85] J. Smagorinsky. General circulation experiments with the primitive equations, i. the basic experiment. *Monthly Weather Review*, pages 152,9199, 1963. 38

[86] D. B. Spalding. The combustion of liquid fuels. *Fourth Symposium on Combustion*, page 818830, 1953. 51

[87] E. V. Stekol'shchikov, M. P. Anisimova, I. A. Yatcheni, and O. L. Kondrat'ev. Experimental study concerning the motion and fragmentation of liquid droplets in a gas stream. *J. Engineering Physics and Thermophysics*, 23(2):957–962, 1972. 47

[88] F.X. Tanner. Liquid jet atomization and droplet breakup modeling of non-evaporating diesel fuel sprays. *SAE Transactions: J. Engines*, pages 106, 127140, 1998. 64

[89] H. Tennekes and J.M. Lumley. *A First Course in Turbulence.* New York: Springer-Verlag, 1972.

[90] S.T. Turns. *An Introduction to combustion.* McGraw-Hill, Inc, 1983. 25

[91] B. P. Volgin and F. S. Yugai. Experimental determination of the drag coefficient of a liquid droplet in the process of deformation and breakup in a turbulent gas flow. *J. Applied Mechanics and Technical Physics*, 9(1):118–120, 1968. 47

[92] A. Wierzba. Deformation and breakup of liquid drops i a gas stream at nearly critical weber numbers. *Experiments in Fluids*, 9:59–64, 1990. 63

[93] W. Wille. Large eddy simulation of jets in cross flow. *Imperial College London, PhD thesis*, 1997. 34

[94] M. William. *Large eddy simulation of spray impingement.* PhD thesis, Imperial College London, 2006. 57

[95] F. A. Williams. Spray combustion and atomization. *Phys. Fluids*, 1(6):541–545, 1958. 66, 69

[96] Suresh Menon Won-Wook Kim and Hukam C. Mongia. Large-eddy simulation of a gas turbine combustor flow. *Combustion Science and Technology*, 143:25–62, 1999. 25

[97] Jones W.P. Large eddy simulation if the filtered probability density function method: Auto ignition and lifed flames, les and dns of ignition process and complex structure flames with local extintion. *AIP Conference Proceedings*, 2008. 162

[98] Jones W.P and Lindstedt P. Global reaction schemes for hydrocarbon combustion. *Combustion and Flame*, pages 73:23–249, 1995. 162

[99] G. Xu and R.A. Antonia. Effect of different initial conditions on the turbulent round free jet. *Experiments in Fluids 33*, page 677683, 2002. 86

[100] F. Yeh and U.Lei. On the motion of small particles in a homogeneous isotropic turbulent flow. *Phys. Fluids*, pages 3, 25712586, 1991. 25, 35

[101] M. C. Yuen and L. W. Chen. On drag of evaporating liquid droplets. *Comb. Sci. & Tech.*, 14:147–154, 1976. 47

[102] M. C. Yuen and L. W. Chen. Heat transfer measurements of evaporating liquid droplets. *Int. Jour. of Heat and Mass Transfer*, pages 21:537–542, 1977. 50, 51

[103] S. Yuu, T. Ueno, and T. Umekage. Numerical simulation of the high re number slit nozzle gas-particle jet using subgrid scale coupling les. *Chemical Eng. Science*, page 42934307, 2001. 52